DIPARTIMENTO DI INGEGNERIA INDUSTRIALE

Dottorato di Ricerca in Ingegneria Meccanica

XIV Ciclo N.S. (2013-2015)

**"*Modeling and control of advanced powertrain systems
and Waste Heat Recovery technologies for
the reduction of CO$_2$ emissions in light-duty vehicles*"**

Ing. Andrea Cricchio

Il Tutor

Ch.mo Prof. Cesare Pianese

Il Coordinatore

Ch.mo Prof. Vincenzo Sergi

Table of contents

Index of figures

Index of tables

CHAPTER 1

Introduction

This Chapter shows the motivations and the objectives of the analysis performed towards the identification of technical solutions aiming at effective carbon dioxide (CO_2) reduction from automobiles. The Regulation of the European Commission for new passenger cars is described, analysing the severe CO_2 emissions limits and the envisaged sanctions. Several techniques to improve the engine efficiency, and, consequently, to reduce the greenhouse gas emissions are presented. Notably, conventional technologies (i.e. already exploited), hybridization and new Waste Heat Recovery systems (WHRs) are described and analysed. The last section of this first introduction stresses the importance of the vehicle simulations and lists the main simulators available in literature to quantify the fuel economy, the performance and the emissions.

1.1 Motivations

1.1.1. European Commission Regulation on CO_2 emission for passenger cars

Transportation is the major sector in the European Union (EU) where greenhouse gas emissions are still rising. Therefore, in the recent years, the main goal of OEMs research and development has been focused on the reduction of CO_2 and pollutants emissions. The European Commission (EC) proposed targets for the further reduction of CO_2 emissions from new cars by 2020. The enforcement of these rules could cut average emissions from new cars down to 95 grams of CO_2 per km (g CO_2/km) by 2020 with respect to 135.7 grams in 2011 and a mandatory target of 130 grams in 2015 [1]. To make effective the new regulation, economic penalties are imposed. Any manufacturer exceeding its limit value on fleet basis has to pay: €5 for the 1st g/km; €15 for the 2nd g/km, €25 for the 3rd g/km, and €95

for any further g/km. From 2019, the cost will be €95 from the first gram. In the normative framework, the European Commission envisaged a specific category of technologies, addressed as 'eco-innovations', that provide a confirmed contribution in terms of CO_2 reduction. According to the issued regulations, all carmakers, upon request, can benefit from a credit of up to a maximum of 7 g/CO_2 if they adopt approved and certified Eco-Innovations on each vehicle [1].

Emission targets are set as function of the average mass in running order of the vehicle fleet, according to a limit value curve. This curve is built in such a way to assume the average mass of manufacturer fleet equals to the reference mass value M_0. The reference mass vehicle is changed every three years from the EC (starting from the 31st October 2014), referred to the average mass of new passenger cars in the previous three calendar years [2] Then for each manufacturer, the target for the reference mass value is fixed to 95 g CO_2/km.Therefore, for each vehicle mass the new emission limit is obtained from the following relationship

$$\text{specific emissions of } CO_2 = 95 + a \times (M - M_0) \tag{1.1}$$

where a is 0.0333, M is the average mass of the manufacturer's fleet in kilograms (kg) and M_0 is the reference mass.

The Figure 1.1 reports the limit value curves defined for the passenger cars targets in 2015 and 2020.

CO$_2$ specific emissions (g CO$_2$/km)
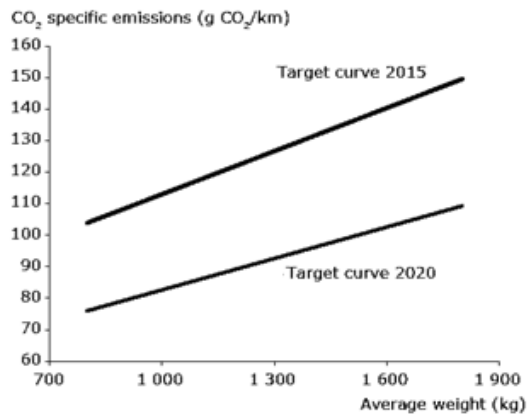
Figure 1.1 - The two limit value curves for the calculation of the passenger cars target in 2015 and 2020 [2].

These regulations can be considered the driving force behind most of

the advancements in the technology of the automobiles, ranging from the improvement of the engine efficiency to the hybridization of the vehicles. In this scenario, a specific attention is paid to different powertrain solutions as the electrical vehicles (EVs), the hybrid electric vehicles (HEVs) and, more recently, the fuel cell hybrid vehicles (FCHVs). Nevertheless, the IC engine will keep its role in the automotive field by matching it with technological innovation that could allow meeting the legislation requirements in the next decade. Indeed, in the last years, engines downsizing, stop and start systems and others technologies for engine efficiency improvement have been the dominant trend in engine design for light duty vehicles. However, more recently, waste heat recovery (WHR) systems are some of the major topics of research, as their application may lead to a significant improvement of the fuel economy [3].

1.1.2. Reducing CO_2 emissions from internal combustion engines

The automotive industry is increasing its focus on developing fuel-efficient vehicles. In the world, the automotive internal combustion engines are mostly fueled with gasoline and diesel; with little case fuelled by compressed natural gas, liquefied petroleum gas, liquefied natural gas or biomass-based fuels. The liquid hydrocarbons are well established, thanks to their features and for the convenient emission process exploited to generate mechanical energy from its combustion. Furthermore, the easiness to handle it and the large availability affected the considerable development and the expansion of the internal combustion engines for the propulsion systems [4]. In spite of these benefits, the diffusion on a global scale brought the ICE to show some critical points. Among these, the most important disadvantage is the rather poor efficiency, approximately between 35% and 45%. Moreover, the operating conditions where the engines work in the optimum efficiency states are seldom, and consequently this effect negatively affects the fuel consumption and the emissions. Figure 1.2 shows the operating points for a 1.3 l Diesel engine 95 hp, during ECE, EUDC and WLTC.
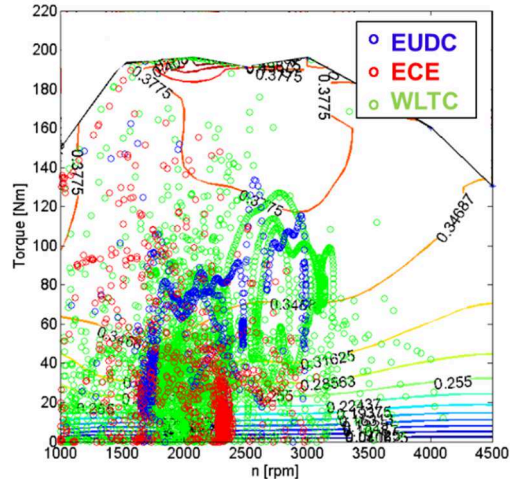
Figure 1.2 - 1.3 l Diesel MultiJet engine 95 hp and the ECE, EUDC and WLTC working conditions.

On the energy side, it is worth noting that in today vehicles, approximately 60% of the chemical energy of fuel is lost in the form of waste heat, dissipated by the cooling and exhaust systems. The most sources of losses could be significantly decreased by means of several advanced powertrain design, while waste heat, in particular at exhaust of the engine, is the major source of inefficiency, as well as the combustion process. The temperature in the coolant is generally around 90 °C with minor variation with engine speed or load. While, the exhaust temperatures can be as high as 900 °C for SI engines and around 500 °C for CI engines. Therefore, there is clearly an opportunity to recover waste heat. Such an opportunity could be exploited by using advanced technologies without substantially modifying the powertrain. Thus, research efforts are oriented towards technologies that can convert thermal energy in electricity from the energy lost of engine exhaust and/or from the coolant loop. Furthermore, the growing demand for electric energy in vehicles is currently being met with inefficient mechanical generators that are driven by the engine. Although improvements in generator efficiency are on going, still an amount of mechanical energy must be generated by the engine to produce the requested electric energy, thereby decreasing overall system efficiency. On the other hand, generating electricity from the energy lost to engine exhaust or from the coolant loop would be, essentially, "free energy" leading to an improvement of overall system efficiency.

In the last decades, new innovative technologies that improve light-duty engine fuel economy and reduce the CO_2 emissions by shifting the ICE operating points closer to the minimum specific fuel consumption area have been developed. These technologies include downsizing, turbocharging of the ICE, cylinder de-activation, low pressure exhaust gas recirculation, etc. These technological improvements are able to make the internal combustion engine more efficient [5]. The downsizing of the ICE allows shifting the working point toward higher thermal efficiency area of the engine. The loss in power can be replaced by the turbocharger or by the coupling with a system made of an electric motor generator (EMG) and a battery. The EMG and batteries provide the requested power needed to maintain vehicle performance. Therefore, a reduction of fuel consumption and the CO_2 emissions for passenger cars occurs with the introduction of electrification or hybridization of the vehicles. An accurate description of the several hybrid configuration and their control strategies are reported in Chapter 4, by illustrating the results of simulations along the standard driving cycles.

Furthermore, research efforts are moving towards Waste Heat Recovery (WHR) systems, considering several technologies for electrical or mechanical energy generation [6][3][7][8]. These innovative technologies include Electric Turbo Compound (ETC), Thermo-Electric Generator (TEG) and Organic Rankine Cycle (ORC) that have been practically implemented on few heavy-duty applications but have not been proved yet as effective and affordable solutions for passenger cars. The WHRs recover energy from the heat and the velocity of the exhaust gases and will be better described in the Chapter 4.

However, quite often when considering fuel economy only engine efficiency is taken into account. The achievement of the highest feasible engine efficiency does not imply that the other components or proprieties of the vehicle are optimized and their influence on fuel economy is frequently disregarded. The optimal design of the engine to reach a high efficiency and consequently benefits in terms of fuel economy could be useless if there is no proper matching between the engine and the vehicle and a lack of integration among the components. Furthermore, relevant impact on the efficiency is also due to the vehicle weight, aerodynamic drag and rolling resistance. Therefore, in addition to the waste heat recovery systems, other energy recovery systems (ERSs) for vehicles have been researched and can be classified according to the source of energy to be

recovered [7]:
- energy from vertical oscillations of the body;
- energy from vehicle inertia.

The vertical oscillations of the vehicle body during driving, such as bumping, result in a kinetic energy, that can be recovered in part with regenerative shock absorbers (RSAs). These devices allow transforming the kinetic energy into electric energy. The efficiency of this ERS technique depends on the type of vehicles and road. For these reasons, major advantages can be reached with heavy-duty vehicles and rough surfaces. Also the conversion of kinetic energy into electric energy can be done by exploiting the vehicle inertia; this technology is called kinetic energy recovery system (KERS). This energy recovery process is most common in electric and hybrid-electric vehicles. In conventional vehicles, during deceleration phases, the braking system has to overcome the inertia of the vehicle, by decreasing the speed and converting part of the kinetic energy into waste heat in the brakes. Here, a fraction of energy can be recovered and used for either improving the vehicle performance during the acceleration phases, or it can be used for cruising. Therefore, the high engine load is reduced with fuel saving. The regenerative braking is the term that is used to identify this process [7].

Summarizing, the growing awareness of environmental issues together with concerns about competitiveness and the possible sanctions imposable by the European Commission have generated considerable interest in research of advanced technologies for highly efficient internal combustion engines (ICE). Although competing hybrid, electric and even fuel cell vehicles are being developed and already commercialized by many car companies, the vehicles equipped with ICE and, particularly, diesel engine again represent an important share in the research activities, with more than 50% of firms' patent portfolios [9]. Indeed, a broad potential for energy savings by means of the exploiting of waste heat recovery (WHR) technologies is recognized by several studies. Thus, such technologies can potentially ensure maintaining the dominance of internal combustion engines and give a concrete answer to increasingly strict emission standards.

1.2 Objectives

In order to increase the efficiency of the internal combustion engines, the automotive industry has shown considerable interest on the waste heat recovery technologies, which have seen rapid development in recent years. Such technologies present a great potential for energy savings and can play a role in responding to increasingly strict emission standards and in maintaining the ICEs very competitive. On the other hand, hybrid electric vehicles are currently considered the most viable alternative propulsion system and, due to their significant potential in reducing fuel consumption and emissions, are now actively developed by many car companies [10]. In this scenario, this work has focused on the investigation of several hybrid configurations and WHRs from a broader perspective to better understand advantages and limits of these systems for passenger cars. This study includes mainly theoretical and modeling activities and aims at identifying the general principles and assessing the methodologies for modeling and control of alternative and innovative powertrain systems.

According to the theory of propulsion systems, vehicle-powertrain system is considered as a complex plant consisting of several interconnected components. The techniques and the methods presented for the modeling of engines and vehicles have general validity. They allow developing numerical tools to perform both scenarios analyses and control strategy design for several applications. Indeed, the approach followed supports the study of each component for the optimization and their matching management to improve system performance.

Particular attention is given in this work to the development and the control of the WHRs models and their integration in the vehicle-powertrain model. Moreover, also the modeling of the hybrid and fuel-cells powered vehicles has been approached to cover long term scenario.

Apart from the analysis just mentioned this thesis provides a comprehensive framework towards further studies that can broaden the vision and promote the development of efficient innovative technologies.

A model based computational platform capable to simulate different vehicles with several powertrain configurations has been developed; to achieve a modularity approach that confers to the model composability and scalability properties. The vehicle-powertrain model simulates the full longitudinal simulation of the powertrain, as well as engine, driveline,

transmissions and electrical components. It allows evaluating the benefits achievable in terms of fuel economy and CO_2 reduction depending on powertrain configuration (vehicle, engine, transmission, etc.), selected scenario (standard NEDC, WLTC or arbitrary driving cycles), Hybrid or WHR technology, components sizing and management.

Thus, different hybrid electric configurations are examined in order to give an overview about the energy conversion and management strategies and a helpful for decisions for design of propulsion systems. On the other hand, the performed investigation explores from a broader perspective the WHRs to better understand the opportunities and limits of these technologies for the conventional vehicles. In general, WHRs could be considered as a secondary component to the vehicle powertrain that could bring to a success in light-duty vehicles in terms the innovation and saving.

1.3 Vehicle simulation tool

To avoid incurring economic sanctions due to non-compliance with CO_2 limits and to meet the more stringent requirements on engine pollutants, powertrain design together with optimal management strategies is the main objective of car manufacturers. The recourse to mathematical models in the automotive sector has gained increased attractiveness from the industry and now has become an essential tool to evaluate vehicle system performance early in the design phase. This increased interest comes from high complexity of the systems to be designed [11].

It is evident that the detailed study of the individual components appears crucial to correctly estimate the impact they have on emissions and fuel consumption, which may be analysed both individually or integrated in a global context. Therefore, modularity features are required to easily compose arbitrary systems by selecting and connecting all components. A sufficiently composable model structure makes it possible to automatically create systems by defining appropriate rules of connectivity. This feature is necessary to guarantee a comprehensive vehicle design, avoiding the missing of features that would be overlooked in a heuristic approach [12]. The most important property of some model to be used for scenario analysis is its scalability. For emphasis, the objective is the use of a generic model reproducing basic features. Thus one may estimate and formulate the model

simply by defining scalar parameters, such as displacement or power coefficients. Such an approach can be easily extended to other application field to simulate, e.g. electric motors/generators, pumps, compressors, or any other components [13]. The property is fundamental for correctly assessing the effect played by engine downsizing or other technologies within comprehensive modeling structures. These strategies are adapt to optimization framework and online energy management strategies and to emerging technologies in the automotive field, such as cylinder on demand applications. Willans line formulation widely uses this modeling concept to build scalable models for IC engines and electric machines. The first defines internal combustion engine behavior taking into account two 'size parameters': engine displacement and piston stroke. For electric machines, the scalability is achieved through the use of two other 'size parameters', the rotor volume and the rotor radius. This approach allows expressing the torque, for IC engines, in terms of mean effective pressure and mean piston speed, which are conventionally used to normalize IC engine data. For the EMG, the torque is represented as an air gap shear stress (equivalent to mean effective pressure in IC engines) and a rotor tangential speed (equivalent to mean piston speed in IC engines) [14][12].

In order to develop an accurate vehicle model and evaluate the benefits of several technologies on the fuel economy, a greater understanding of the physical processes within the vehicle system is essential. Most of existing vehicle system models are based on performance maps and guarantee a good prediction of the overall fuel economy. but, for example, sometimes lack the capability to take into account when and where fuel energy is being demanded within the vehicle system along different drive cycles [15]. Therefore, a trade-off among accuracy, generalization, calculus speed, computational burden and physical-theoretical feedback has to be accounted during the model framework development. Although accuracy and computational speed are very high, they are not flexible enough. Moreover, they lack phenomenological description and may not help in supporting physical analysis.

Several vehicle simulators have been introduced by research centers and universities or produced for commercial purposes by companies such as Bosch, AVL, MathWorks, and Ricardo. Many commercial packages are available for simulation of powertrains systems. An empirical tool that combines component efficiency maps with a vehicle dynamic model to predict system performance has been develop by the National Renewable

Energy Laboratory (NREL) to assist the Department of Energy (DOE) in developing technology for hybrids. The model, called Advanced Vehicle Simulator (ADVISOR) [16], owned now by AVL, quantifies the fuel economy, the performance, and the emissions of vehicles including the impact of advanced technologies applied to vehicles, such as fuel cells, batteries, electric motors, internal combustion engines, and hybrids. However, ADVISOR requires the knowledge of the characteristics of each component from experimental data. Therefore, despite tits flexibility in combining some components, it is not flexible due to the large amount of data requires to make useful analysis. Vehicle Systems Analysis Toolkit (P-SAT) is a vehicle simulator developed by Argonne National Laboratory with the support of the U.S. Department of Energy and several American carmakers. It calculates the power generated by the powertrain on a predefined cycle. An additional tool (PSAT-PRO) was developed and integrated to make the PSAT capable of real-time simulation, hardware in the loop (HIL) and rapid-prototyping [17]. At the same time, Southwest Research Institute (SwRI) has developed a commercial, whose name RAPTOR (Rapid Automotive Performance Simulator). RAPTOR is an application program written in Matlab®/Simulink®, which allows powertrain components to be simulated in a virtual environment. Mathematical descriptions of vehicle powertrain components are assembled in software and simulated under various user-selectable driving schedules in a process of linking these powertrain components and sub-components from the engine to the wheels. RAPTOR may help automotive engineers to analyse and optimize vehicle powertrain systems performance, efficiency and emissions [18][15]. Also, the Automotive Research Center at the University of Michigan has developed and later refined a Vehicle Engine Simulator (VESIM) composed of engine, driveline and vehicle dynamics modules to simulate the dynamic response of a Class VI heavy duty diesel truck [19]. The unified approach of power flow, where mechanical, electrical and chemical power are universally represented by effort and flow, was applied to the modeling and analysis of hybrid vehicles in a computer simulation called, Vehicle Performance Simulator (VP-SIM) [13]. The aforementioned vehicle simulations are adequate at providing solutions for future vehicle system configurations where prototypes are not yet available.

The model described here is based on the work proposed at University of Salerno in two last decades. A computer code for the simulation and

optimization of control strategies in spark ignition automotive engines was presented in 1996 [20]. It was used from industry and can compute engine performance over arbitrary driving cycles starting from steady-state experimental data, by using steady-state approach and considering the most significant dynamical effects of interest for control applications. The model has been updated and expanded later in 2000's, and it is suitable for simulation analysis and to achieve optimal engine control strategies for minimum consumption [21].

1.4 Summary

The present manuscript is divided in three main areas dealing with vehicle modeling approach, hybridization analysis, and waste heat recovery systems.

In the second Chapter, the modeling of the vehicle-powertrain is approached. This section reports on the fundamental approach used to model vehicle systems together with a description of model capabilities and limitations. Model identification and validation are performed vs. experimental data collected both in steady-state conditions at the engine test bench and in transient operations on the vehicle test rig for a C-segment vehicle equipped with SI turbocharged engine.

The Willans line application is described in the Chapter 3, which reports on its use towards the evolution of each technological solution for engine efficiency improvement. The electric, hybrid-electric and fuel cells hybrid-electric propulsion systems are also analysed in this Chapter. Various types of hybrid-electric vehicles are introduced and a description of the quasi-stationary and the dynamic models of typical electric components of such vehicles, including electric motors/generators, batteries is carried out. An analysis of the energy consumption and CO_2 reduction of various powertrain configurations is also reported.

The fourth Chapter analyses the impact of the waste heat recovery systems on the fuel economy. Initially a thorough state of art on the existing models and applications of each analysed system is reported. The modeling and the integration in the vehicle model of such technologies are described for a particular application and the results of the simulations are shown.

In the last Chapter conclusions and perspectives are discussed.

Moreover, the scaling up/down features of the engine are explained in the appendix.

CHAPTER 2

Vehicle-powertrain model

In the last decades, the carmakers have increased their interest for vehicle and powertrain simulators, which have become an important resource for several purposes. An important property is the modular approach [22]. It provides valuable opportunity when different components configurations must be analysed, thus avoiding the recourse to difficult procedure of reconfiguring. In this Chapter, the developed simulator is presented. A thorough description is reported, allowing understanding the impact of each components on the energy management powertrain and vehicle system and which decisions can be taken to improve the efficiency.

2.1 Modeling approach

The theoretical concepts and methodologies presented in this Chapter are the basis for the definition of numerical models that describe the entire vehicle system and the dynamics of specific components and subsystems. By combining together different computational blocks, more complex models can be built and the behaviour of the entire vehicle can be simulated. Thus, in this study, a novel simulation tool for the scenario analysis, control and optimization of conventional powertrains with WHRs and hybrid vehicles based on the forward simulation approach is presented. The simulator, developed in Matlab-Simulink environment, consists of a set of elementary replaceable blocks connected each other to form a tool that simulates complex powertrains. The model serves to the design of engine control strategies to minimize fuel consumption and emissions with constraints on vehicle drivability and comfort.

The global vehicle-powertrain model layout is shown in Figure 2.1: and can see, it is made up of the following main subsystems:
- driver model;
- driveline model, with one state model of the vehicle dynamics;

- black-box parametric approach of the in-cylinder processes;
- MVEM for intake/exhaust dynamics;
- turbocharger grey-box model, with one-state model of the turbocharger shaft speed;
- battery model, as a first order circuit in the SOC state;
- efficiency map of the alternator;
- electrical loads model.
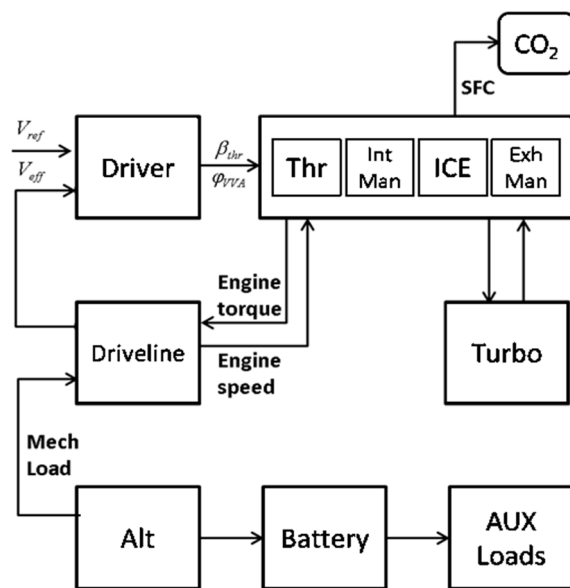
Figure 2.1 - Vehicle-powertrain model framework.

2.2 Driver

Two different approaches are implemented for simulating longitudinal vehicle motions: the backward quasi-static and forward dynamic approaches. The former uses speed and accelerations provided by the drive cycle, in order to guarantee that the powertrain, with the all subsystems, is able to provide the requested load within the operational and physical limits. This allows verifying the correct sizing of the powertrain for the prescribed driving mission. The backward approach assumes that the

torque and speed required at wheels are computed from the speed profile defined in the drive cycle; therefore it does not require a driver model. The subsystems of the powertrain are modeled through a quasi-static approach and the prediction ability of these simulations is generally suitable for the desired purposes, also during the transient maneuvers. Low computational burden and simulation times are guaranteed by a low numerical complexity making such an approach a suitable method for preliminary design studies and often preferred for fuel economy predictions, component sizing, and road load analysis. On the other hand, the forward dynamic approach includes a driver model. The driver model uses the difference between current and required vehicle speed to evaluate the appropriate throttle and brake commands often using a proportional-integral (PI) controller. The actuators signals, e.g. throttle, brakes and steering wheel, are used as inputs to calculate the vehicle dynamics. In fact, the throttle command is translated into a fuel flow rate and engine torque, which represents subsequently the input into the transmission model, where the transmission output torque is computed from the transmission efficiencies and gear ratios. The transmission output torque is transferred forward through the drivetrain towards the wheels, to compute the traction force at the road. Forward-looking models have high accuracy but their major weakness is their long run times. Because this approach requires a control system for tracking a drive cycle it is more suitable to control design and validation purposes, once that the overall powertrain architecture has been correctly sized.

Many commercial packages, mentioned in the Chapter 1, are driven by backward and forward simulation of powertrain systems: example of backward dynamic simulation tool is ADVISOR. On the forward simulation side is worth mentioning the PSAT and the VESIM tools. RAPTOR has the capability of performing both forward- and backward-looking simulations [15].

In the present work only the forward approach has been considered. The engine actuators are driven in closed loop by PID controllers that operate based on the vehicle speed error, in order to make the vehicle able to follow the reference driving transient. Particularly for spark ignition engines with the variable valve actuation system, the VVA map is exploited and the throttle opening is driven by a PID controller based on the vehicle speed error.

2.3 Driveline

In most of the studies dealing with vehicle powertrains, detailed models of the vehicle dynamics is not required and its mathematical description can be limited to longitudinal motion, neglecting the equations describing the lateral behaviour. Therefore, the driveline sub-model describes the longitudinal vehicle dynamics reduced to the engine crankshaft [23]

$$\frac{d\omega}{dt} = \frac{T_{ICE} - T_{aero} - T_{roll} - T_{slope} - T_{acc/aux}}{I_{tot}} \tag{2.1}$$

where the engine torque T_{ICE} is the output of the ICE sub-model (see Figure 2.1) and I_{tot} is the total vehicle inertia reduced to the engine crankshaft. The vehicle dynamics is influenced by aerodynamic drag force (T_{aero}), rolling resistance (T_{roll}), slope (T_{slope}) and alternator load ($T_{acc/aux}$). The alternator resistance torque takes into account the auxiliaries and accessories electrical loads [24].

2.4 In-cylinder model - Willans Line Method

The in-cylinder processes and friction losses of the ICE are modelled by a parametric approach known in literature as Willans line method [25]. Willans line approach consists of an affine representation relating the available energy (i.e. the energy theoretically available for conversion) to the useful energy that is actually present at the output of the energy converter [26]. There are many advantages of adopting such a formulation to describe both conventional and hybrid vehicles. Among others the most important are: the ability to make the model independent of the power rating or 'displacement' of the device, thus permitting easy scaling; the compactness of the model, requiring only two parameters; its straightforward definition and implementation; and the ability to easily compose models, thanks to the unified method of representation [26]. Nevertheless, some drawbacks should be considered when applying such an affine relationship to modern powertrain configurations, such as those featuring turbocharging, downsizing or both advanced design solutions.

The Willans line modeling technique was initially applied to describe the relationship, approximately linear, linking mean effective pressure to brake and engine fuel consumption. Rizzoni et al. [26] extended this model to describe the energy converters, such as engines and electric machines. In fact, in stationary conditions, it is possible to estimate the efficiency of a new machine belonging to the same category, using a scaling approach [20]. Furthermore, this approach is well-suited for immediate and approximate assessment of new design configurations and new engineering solutions for those classes of prototype machines or, in general, for those machines for which there are not enough data on efficiencies.

The key factor of this unique representation is that for a fixed speed, there is a linear relationship between output and input variables. That method suggests a close correlation between the total available energy (the fuel chemical energy) and the real used energy (the energy available at the crankshaft) [27]. The resulting representation is described by two factors: the slope, or intrinsic energy conversion efficiency e, and the vertical axis intercept P_{loss}, which represents the losses due to mechanical friction, alternator, auxiliaries etc., as shown in Figure 2.2.
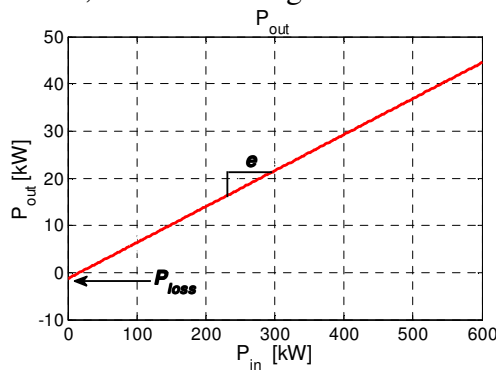
Figure 2.2 - Linear relation between P_{out} and P_{in}. Adapted from Rizzoni et al. [26].

The energy conversion efficiency and the relationship between input and output powers are thus expressed by the following equation

$$P_{out} = e \cdot P_{in} - P_{loss} \tag{2.2}$$

where e has been considered obtained as the product of thermodynamic (η_t) and combustion (η_b) efficiencies. This means that e already accounts for losses due to pumping work. Equation (2.2) can also be expressed in terms of torque, thus though simple substitutions [27]

$$T_e = e \cdot H_{LHV} \frac{\dot{m}}{\omega} - T_{loss} = e \cdot T_a - T_{loss} \qquad (2.3)$$

with T_a available torque, H_{LHV} as the fuel lower heating value, and T_{loss} loss torque due to friction phenomena. To achieve scalable relations, one introduces the concept of mean effective pressure *bmep* (i.e. break mean effective pressure, which can also be seen as the engine's ability to fulfill mechanical work), available mean effective pressure *amep* (represents the available chemical energy by fuel supply) and the average piston speed v_{pist}, corresponding respectively to the output torque, the available torque and engine speed. For a four stroke engine, one obtains

$$\begin{cases} bmep = T_e \cdot \left(\dfrac{4\pi}{V_d} \right) \\[2ex] amep = H_{LHV} \cdot \left(\dfrac{4\pi}{V_d} \right) \dfrac{\dot{m}}{\omega} \\[2ex] v_{pist} = \left(\dfrac{S}{\pi} \right) \omega \end{cases} \qquad (2.4)$$

where V_d is the displacement, $\dot{m}$ is the fuel mass flow rate, ω is the engine angular velocity and S is the piston stroke.
The engine efficiency can then be defined as follows

$$\eta_{ICE} = \frac{P_{out}}{P_{in}} = \frac{\omega T_e}{\dot{m}_f H_{LHV}} \qquad (2.5)$$

Using the relationships given by equation (2.4) and substituting it into equations (2.3) and (2.5), the definition of engine dimensionless efficiency is

$$bmep = e \cdot amep - fmep \rightarrow \eta_{ICE} = \frac{bmep}{amep} \qquad (2.6)$$

where *fmep* is the mean effective pressure lost and is defined in a similar way to *bmep* and *amep*. Parameters *e* and *fmep* are functions of load and piston average speed. The following parameters, selected by referring to Willans line parameter correlations proposed in Rizzoni et al. [26], were experimentally validated on different engines

$$bmep = \left[e_0\left(v_{pist}\right) - e_1\left(v_{pist}\right) \cdot amep \right] \cdot amep - fmep\left(v_{pist}\right)$$

$$e_0\left(v_{pist}\right) = e_{00} + e_{01} \cdot v_{pist} + e_{02} \cdot v_{pist}^{\;2}$$

$$e_1\left(v_{pist}\right) = e_{10} + e_{11} \cdot v_{pist} \tag{2.7}$$

$$fmep\left(v_{pist}\right) = fmep_0 + fmep_2 \cdot v_{pist}^{\;2}$$

It is worth mentioning here that the efficiency-related parameters listed in equations (2.7) were curve-fitted as a multi-linear regression model, here obtained by substituting such equations in equation (2.6).

As aforementioned, the pumping work produces losses that are considered into the efficiency term *e*. For several applications, it needs to decouple the pumping losses from the other members of the equation (2.6), and the result is expressed by the following equation

$$bmep = e \cdot amep - fmep - pmep \tag{2.8}$$

where the pumping losses are defined from the difference between the exhaust manifold and intake manifold pressures

$$pmep = p_{exh} - p_{man} \tag{2.9}$$

This splitting of the several contributions of losses allows accounting for the effect of additional turbocharging or of other devices and technologies that could affect the backpressure and the boosting of the engine. The efficiency related parameters should be adapted in such a way as to decouple purely thermodynamic from turbocharging effects.

Summarizing, Willans line main concepts and applications are:
- scaled engine and reference one should belong to the same engine's class, such as SI engines or CI engines, either aspirated or turbocharged.
- since they aim at generating scale coefficients, the curves should adapt to a wide range of v_{pist} values, to avoid extrapolation when Willans-based engine model is scaled up/down or used for other engine configurations.
- to evaluate the impact of additional technologies on the engine efficiency, as better described in the Chapter 3.

2.4.1. Mathematical modeling of engine losses

Two different approaches for engine losses estimation can be considered: the first adopts a comprehensive evaluation of the total losses, while the second evaluates the contribution of each engine component causing friction losses. It is worth noticing that the experimental results allow stating that, in the second approach, it is possible to obtain a higher degree of accuracy. Therefore, the latter approach was adopted, where all losses are expressed as friction mean effective pressure (*fmep*). It is based on the Bishop's model [29][30]. Different results were obtained from tests with both spark ignition and compression ignition engines, which may consist of one, four, six up to eight cylinders, with several configurations (e.g. in line or V-engine, turbocharged or naturally aspirated) and compression ratios ranging in a wide range [29].

The friction losses rates usually considered are five, as listed below:

- losses due to the piston motion;
- losses related to the intake and exhaust valves;
- losses related to the crankcase;
- losses due to pumping work and phenomena occurring in combustion chamber;
- losses caused by blow-by.

With the aim of adapting a detailed phenomenological model (such as that proposed by Bishop in the 50s [30], but developed and tested on more actual engines by Lee et al. [29]) a simplified model based on Willans line approach was used. It neglects the friction losses relating to the intake-exhaust system (e.g. pumping losses induced by valve movement), as well as those losses related to the phenomena that take part in the combustion phase. Furthermore, as mentioned above, the losses due to pumping work are already accounted for by Willans line model (equation (2.6)), thus avoiding calculating a further loss quote. It is worth commenting that the blow-by causes a loss of chemical energy and is not a mechanical loss; however it is involved by Bishop within the list of mechanical losses.

Therefore, two friction losses are considered and one caused by blow-by as follows:

- Crankcase mechanical friction, including:
    - friction losses related to bearings,
    - friction losses linked to the gears responsible for valves movement,

- mechanical friction losses related to the auxiliaries;
- Piston mechanical friction (mechanical losses associated with the piston motion) are due to the sum of two contributions:
  - friction losses related to the stress on piston rings,
  - losses related to the viscosity and the presence of rings on the piston skirt.
- Blow-by: this term is considered only for gasoline engines; for compression ignition engines, characterized by direct injection systems, blow-by is not considered because the fuel is generally injected just before the ignition takes place, thus ensuring the combustion occurs with the appropriate concentration of fuel nearby the ignition point.

The main losses contributions are modeled [29] as shown below.

Journal bearings contribution is expressed by

$$fmep_1 = 41.37 \left(\frac{B}{S}\right)\left(\frac{N}{1000}\right)K \tag{2.10}$$

where K is a dimensional coefficient of journal bearings depending on bore B and various geometric parameters (values for SI and CI engines are 0.14 and 0.29, respectively).

As for valve gears,

$$fmep_2 = 245.73 \left(30 - \frac{4N}{1000}\right)\left(\frac{GH^{1.75}}{SB^2}\right) \tag{2.11}$$

where G is the intake valves number per cylinder and H is the intake valve head diameter. The above equation is experimentally obtained to estimate the friction losses due to single overhead camshaft (SOHC) configuration. For double overhead camshaft (DOHC) configuration, such as compression ignition engine considered in this work, the loss rate was simply doubled.

Auxiliaries are modeled through equation (2.12), which was specifically used to model losses of alternator, water pump, oil pump and power steering pump, where present

$$fmep_3 = 6.23 + \left(5.22 \cdot 10^{-3}\right)N - \left(1.79 \cdot 10^{-7}\right)N^2 \tag{2.12}$$

Blow-by effect was included for SI engine through the following equation

$$fmep_4 = 6.895 \left(\frac{p_a - p_1}{97.909} \right)^{0.5} \cdot$$
$$\cdot \left[1.72 R_C^{0.4} - \left(0.49 + 0.015 R_C \right) \left(\frac{N}{1000} \right)^{1.185} \right] \tag{2.13}$$

where p_a denotes the atmospheric pressure, p_1 is the difference between atmospheric and intake manifold pressure and R_c is the compression ratio.

Finally the effects due to the viscosity and the presence of rings on the piston outer surface are accounted for through the following equation

$$fmep_5 = 369.53063 \left(\frac{Sn}{B^2} \right) + 756.037 \left(\frac{MV_p}{BS} \right) \tag{2.14}$$

with n number of piston rings per cylinder, M equivalent piston skirt length and V_p average piston speed. Geometry of engine components were estimated via specific tables provided by the manufacturer.

2.5 Mean Value Engine Model (MVEM)

To solve the trade-off between accuracy and computational time in the simulation of fluid systems, Mean Value Models have been proposed for predicted and effective uses. Such an approach allows describing physical phenomena with a time scales small enough to account for transients, but neglecting smallest ones [22]. These kind of models have also been amply used to reproduce the behaviour of internal combustion engine systems and the acronym has been changed in MVEM (Mean Value Engine Model) [22]. Currently, such models have a simplicity and accuracy which sometimes allows them to be coded into engine control microprocessors [31].

For the purpose of the engine manifolds modelling, a mean value approach with lumped parameters, ensuring satisfactory accuracy and low computational demand has been implemented. The engine components of interest (i.e. intake/exhaust manifolds, EGR system) are modeled as control volumes in which the dynamics of the state variables have a time scale slightly larger than the engine cycle; thus the cycle-to-cycle variations can

be disregarded. Following the Filling and Emptying formulation, mass and energy conservation is applied in some control volume, along with information on incoming and outcoming mass flow rates. Furthermore homogeneous pressure, temperature and chemical compositions inside the manifold are assumed together with instantaneous and perfect mixing of incoming flows [32].

A first schematization, analysed below, allows modeling a purely naturally aspirated Spark Ignition (SI) engine. The model of the intake manifold is reported and is obtained by differentiating the ideal gas law applied to the mass of air in the intake manifold [31]

$$p_{man} = \frac{R T_{man}}{V_{man}} m_{man} \qquad (2.15)$$

Assuming that

$$\dot{m}_{man} = -\dot{m}_{cyl,in}\left(n, p_{man}\right) + \dot{m}_{thr}\left(\alpha_{man}, p_{man}\right) \qquad (2.16)$$

Taking the time derivative of the equation (2.15) yields the simple manifold pressure state equation

$$\frac{dp_{man}}{dt} = \frac{R}{V_{man}}\left(\dot{m}_{man}T_{man} + m_{man}\dot{T}_{man}\right) =$$
$$= \frac{R T_{man}}{V_{man}}\left(-\dot{m}_{cyl,in} + m_{thr}\right) \qquad (2.17)$$

where the last equation holds for isothermal conditions in the intake manifold. This is thus an isothermal MVEM. The port and throttle air mass flows are given by two algebraic equations: the speed density equation and law of mass flux through an orifice [31].

Equation. (2.17) can be upgraded by considering the EGR system (see equation. The model can be enhanced by adding other equations describing temperature and oxygen concentration states [24]. The knowledge of intake gas composition, in particular the O2 concentration, in several sections of the air/exhaust paths (e.g., intake manifold, engine outlet, upstream and downstream the catalysts) is fundamental to model combustion process, emissions formation and after-treatment devices management. In particular, for the SCR system in CI engines, NOx evaluation upstream and downstream the catalyst is essential for control and diagnosis purposes.

Some variables may be measured by several sensors located in different sections of the engine, resulting in a reduction of the states of the model, as well as a lower computational burden.

The layout of an engine equipped with EGR path and Turbocharger is sketched in Figure 2.3.
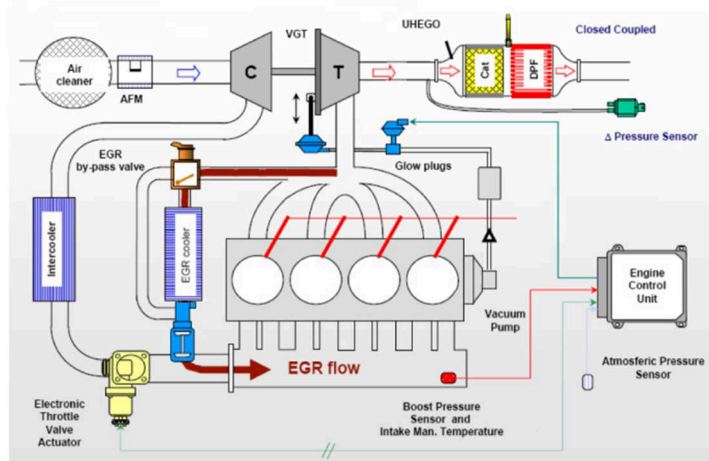
Figure 2.3 - Engine layout [32].

2.5.1. Intake manifold

For those engines not equipped with EGR it has been shown that the simple state equation (see the right hand side of equation (2.17)) is accurate enough to describe the dynamics of the intake manifold. It is worth noting that Exhaust Gas Recirculation (EGR) is an important technology of the modern CI and SI engines control systems. It reduces the mean in-cylinder temperature lowering also the NOx emissions to fulfil the limits imposed by the legislation. For the SI engines, it even provides a method to reduce exhaust temperature and thus to prevent Three Way Catalyst damage. When the EGR has to be accounted, the intake manifold model must include the energy balance [31][33] and the following equations apply

$$\frac{d\left(m_{man}\right)}{dt} = \dot{m}_{man} + \dot{m}_{egr} - \dot{m}_{cyl,in} \tag{2.18}$$

$$\dot{m}_{thr}h_{air} + \dot{m}_{egr}h_{egr} - \dot{m}_{cyl,in}h_{cyl,in} = \frac{d(mu)_{man}}{dt} =$$

$$\dot{m}_{man}c_pT_{man} + m_{man}c_v\dot{T}_{man} \tag{2.19}$$

whose states are: temperature, pressure and oxygen mass fraction. Therefore, the system (2.18) - (2.19) can be recast as follows

$$\frac{dT_{man}}{dt} = \frac{\dot{m}_{thr}c_{p,air}T_{thr} + \dot{m}_{egr}c_{p,exh}T_{egr}}{m_{man}c_{v,man}} +$$

$$- \frac{\dot{m}_{cyl,in}c_{p,cyl,in}T_{cyl,in} + \dot{m}_{man}c_{v,cyl}T_{man}}{m_{man}c_{v,man}} \tag{2.20}$$

$$\frac{dp_{man}}{dt} = \frac{R_{air}T_{man}}{V_{man}}\left(\dot{m}_{thr} + \dot{m}_{egr} - \dot{m}_{cyl,in}\right) \tag{2.21}$$

$$\frac{dO_{2,man}}{dt} = \frac{R_{air}T_{man}}{p_{man}V_{man}}\left[\begin{array}{c}\dot{m}_{egr}\left(O_{2,exh} - O_{2,man}\right) \\ + \dot{m}_{thr}\left(O_{2,amb} - O_{2,man}\right)\end{array}\right] \tag{2.22}$$

In the equation (2.22) $O_{2,amb}$ and $O_{2,exh}$ are the oxygen concentrations in the ambient air (i.e. 20.9 %) and in the exhaust manifold, respectively.

According to the scheme of Figure 2.3, the intake manifold temperature evaluation is based on the thermodynamic modeling of the intercooler and the EGR system [32]. The air temperature downstream the intercooler is computed by modeling the efficiency of the heat exchanger as [34]

$$\varepsilon = \frac{C_h\left(T_{hi} - T_{ho}\right)}{C_{min}\left(T_{hi} - T_{ci}\right)} \tag{2.23}$$

where C_{min} is the minimum heat capacity between hot and cold fluids evolving in the exchanger and C_h is the heat capacity of the hot fluid. In equation (2.23) it is assumed that the outlet cooling air temperature (i.e. T_{co}) reaches the same value of the inlet hot gases (i.e. T_{hi}). For the intercooler under study, the minimum heat capacity corresponds to that of air thus leading to the following equation for the efficiency

$$\varepsilon_{ic} = \frac{\left(T_{ic,in} - T_{ic,out}\right)}{\left(T_{ic,in} - T_{cool}\right)} \Rightarrow$$

$$\Rightarrow T_{ic,out} = T_{cool}\varepsilon_{ic} + T_{ic,in}\left(1 - \varepsilon_{ic}\right) \tag{2.24}$$

where the efficiency is evaluated by a polynomial regression as function of the engine operating conditions

$$\varepsilon_{ic} = f\left(n, \dot{m}_{air}, P_{man}, u_{EGR}\right) \tag{2.25}$$

A similar approach is adopted to estimate the temperature downstream of the EGR cooler

$$\varepsilon_{egr,c} = \frac{\left(T_{egr,in} - T_{egr,out}\right)}{\left(T_{egr,in} - T_{cool}\right)} \Rightarrow$$

$$\Rightarrow T_{egr,out} = T_{H2O}\varepsilon_{egr,c} + T_{egr,in}\left(1 - \varepsilon_{egr,c}\right) \tag{2.26}$$

where the heat exchanger efficiency is expressed as function of the EGR mass flow rate

$$\varepsilon_{egr,c} = f\left(\dot{m}_{egr}\right) \tag{2.27}$$

The black-box models expressing the heat exchangers efficiency (i.e. equations (2.25) and (2.27)) need for experimental measurements of temperature upstream and downstream the intercooler and the EGR cooler In a simplified approach the manifold temperature could be assumed constant and equation (2.20) could be neglected; this is the case when both intake and exhausted gases have constant temperatures due to effectiveness of the air intercooler and Egr cooler, respectively. In such a case the model will be an adiabatic one [31]. For the purpose of the current work the full set of equations (2.20) - (2.22) has been considered. The mixing of the gases into the plenum is considered perfect and instantaneous, leading thus to uniform conditions within the volume.

The air flow through the throttle is modelled assuming an orifice [35] where the upstream pressure equals the compressor outlet pressure. The air flow to the engine is evaluated by the speed density equation

$$\dot{m}_{air,eng} = \lambda_v \frac{\rho_{amb}V_d n}{120} \tag{2.28}$$

where volumetric efficiency is estimated by a polynomial regression as function of intake manifold pressure, manifold temperature and engine speed

$$\lambda_v = f\left(n, P_{man}, T_{man}\right) \tag{2.29}$$

The tuning parameters of the polynomial regressions are determined by solving a linear least-squares problem, making use of the 'stepwise' algorithm [32]. It has been identified and validated through a set of experimental data measured in steady state and transient operations on a Fiat 1.3 litres, 4 cylinders, EURO 5 Diesel engine, equipped with Common-rail injection system, high pressure EGR and variable geometry turbocharger (VGT). Figure 2.4 shows the comparison between measured and predicted volumetric efficiency by equation (2.29), showing a very good fitting ($R^2 = 0.991$).
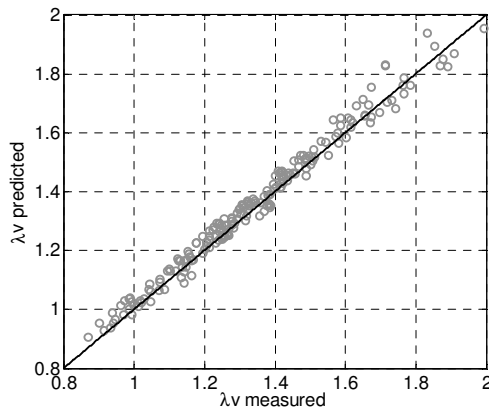
Figure 2.4 - Comparison between measured and simulated volumetric efficiency.

The influence of the EGR rate on the volumetric efficiency is indirectly accounted through the intake manifold temperature, which depends on the mixing between fresh air and recirculated gases [32].

In case of presence of Variable Valve Actuation system the volumetric efficiency is affected by the VVA actuator. When VVA systems are installed, the volumetric efficiency is influenced also by the operation of such a technology. To account for VVA, again a regression model is implemented but the variables are engine speed, intake manifold pressure and VVA actuator position

$$\lambda_v = f(n, p_{intake}, \phi_{VVA}) \tag{2.30}$$

Figure 2.5 shows the comparison between measured and estimated volumetric efficiency, with respect to the set of steady-state experimental data available for 1.4 liters turbocharged spark ignition (SI) engine with variable valve actuation (VVA).
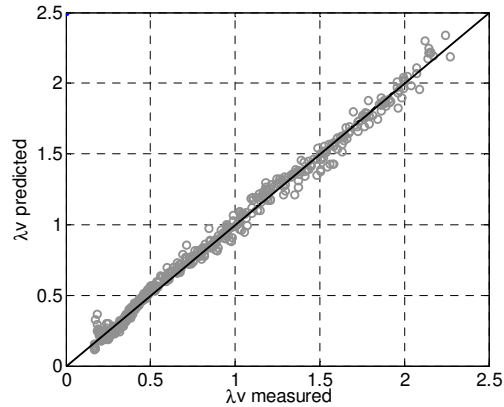
Figure 2.5 - Comparison between measured and simulated volumetric efficiency.

The figure exhibits good model accuracy with correlation index equal to 0.997.

To compute the EGR flow rate, the hypothesis of perfect mixing is applied

$$\dot{m}_{egr} = \dot{m}_{cyl,in} - \dot{m}_{thr} \tag{2.31}$$

2.5.2. Exhaust manifold

Similarly to the intake manifold, the exhaust manifold model is based on mass and energy equations

$$\frac{d(m_{exh})}{dt} = \dot{m}_{cyl,out} - \dot{m}_{egr} - \dot{m}_{turb} \tag{2.32}$$

$$\dot{m}_{cyl,out}h_{cyl,out} - \dot{m}_{egr}h_{egr} - \dot{m}_{turb}h_{turb} = \frac{d(mu)_{exh}}{dt} =$$

$$\dot{m}_{exh}c_vT_{exh} + m_{exh}c_v\dot{T}_{exh}$$

(2.33)

The gas dynamics in the exhaust manifold is modeled as a three states system, namely temperature, pressure and oxygen concentration [32]

$$\frac{dT_{exh}}{dt} = \frac{R_{exh}T_{exh}}{V_{exh}}\left(\begin{array}{c}\dot{m}_{cyl,out}\left(k_{exh}T_{cyl,out} - T_{exh}\right) + \\ -\dot{m}_{egr}\left(k_{exh}T_{exh} - T_{exh}\right) + \\ -\dot{m}_{turb}\left(k_{exh}T_{exh} - T_{exh}\right)\end{array}\right)$$

(2.34)

$$\frac{dp_{exh}}{dt} = \frac{R_{exh}T_{exh}}{V_{exh}}\left(\dot{m}_{exh}T_{cyl,out} - \dot{m}_{egr}T_{exh} - \dot{m}_{turb}T_{exh}\right)$$

(2.35)

$$\frac{dO_{2,exh}}{dt} = \frac{R_{exh}T_{exh}}{p_{exh}V_{exh}}\left[\dot{m}_{cyl,out}\left(O_{2,cyl,out} - O_{2,exh}\right)\right]$$

(2.36)

where the cylinder out temperature can be computed by a polynomial regression derived from experimental data, as function of the engine operating conditions

$$T_{cyl,out} = f\left(\dot{m}_{air}, \alpha, n, p_{man}, u_{EGR}\right)$$

(2.37)

The oxygen concentration in the exhaust manifold could either be measured by a UEGO sensor located downstream of the turbine or simulated in case the sensor is available or faulty.

The oxygen concentration at the engine outlet is computed by the O_2 mass balance between intake and exhaust manifolds

$$O_{2,cyl,out} = \frac{\dot{m}_{cyl,in}O_{2,man} - \alpha_{st}\dot{m}_fO_{2,man}}{\dot{m}_{cyl,in} + \dot{m}_f}$$

(2.38)

2.6 Turbocharger

This paragraph describes the turbocharger model and its equations. The compressor and turbine are components that present features that are difficult to model due to the complex thermos-fluid dynamic interaction between both thermomachines and the volumetric engine. Moreover, the characteristic curves provided by the manufacturers do not cover all operating regions of the engines coupled with the turbocharger. Indeed, the maps for low speed and low torque engine operations are not available [36]. It is worth that most of Turbochargers use Wastegate (WG) and/or Variable Geometry Turbine (VGT) systems, which are difficult to simulate. The manufacturers provide the characteristics of turbine and compressor by means of some maps, which are specific particularly for higher turbo speeds [11].

The Wastegate valve allow exhausted gases to bypass the turbine to reducing the load. When the bypass valve is open the reduced flow rate and the lower pressure acting on the turbine limit its power generated, thus the shaft speed is also limited. Therefore, the power to the compressor is reduced and the boosting action is also kept low. The Wastegate flow is modeled as a flow restriction for a compressible fluid, by assuming an isoenthalpic process, which does not cause a change into the fluid temperature over the WG.

The VGT system controls the inlet flow to the turbine rotor by changing the geometry of the stator blades and thus the inlet absolute velocity. In such a case the variation of the power delivered by the turbine is more accurate and the efficiency of the turbine is also optimized by choosing the right opening of the VGT vanes. Moreover a reduced lag is experienced by those systems on which the VGT is implemented and well controlled. The VGT is modeled by fitting the turbine model parameters to different VGT positions [37].

In order to guarantee short computational time and satisfactory accuracy, the modeling approach could be based on the experimental maps of the two machines provided by the manufacturers. Therefore, four linear interpolation algorithms can be derived from the manufacturers data to simulate the steady-state operation of compressor and turbine. This approach is consistent with the hypothesis that the fluid dynamics of the two machines is faster than the rotational dynamics of the turbocharger.

The data driven models were developed to estimate the turbine mass flow rate, the compression ratio and the efficiencies of both machines, depending on exhaust gas thermodynamic properties, turbocharger speed and VGT or WG control (χ) [38]

$$\dot{m}_t = f_1\left(P_{exh}, T_{exh}, n_{tc}, \chi\right)$$
$$\beta_c = f_2\left(\dot{m}_c, n_{tc}\right)$$
$$\eta_t = f_3\left(P_{exh}, T_{exh}, n_{tc}, \chi\right)$$
$$\eta_c = f_4\left(\dot{m}_c, n_{tc}\right)$$

(2.39)

where f_i are the interpolating functions.

Standard interpolating methods like polynomial regressions or look-up tables generally fail to produce accurate results outside the region where experimental data are available. They do not describe with the right accuracy the complex thermo/fluid-mechanic phenomena occurring inside the compressor and the turbine. In order to fit the maps and extend them to the region of low turbocharger speed an appropriate methodology of curve fitting should be used.

To reproduce the behaviour of the turbocharger, two models were developed, for compressor and turbine, respectively. These models are coupled to account for the dynamics of the turbocharger by means of the power balance at the turboshaft.

2.6.1. Compressor model

Two approaches have been followed for the compressor model:

1. An interpolation black-box based on the "moving least squares method";
2. A grey-box model, able to extrapolate the map at low compressor speeds.

These two models are matched together to simulate the compressor into the entire operating domain. The former is applied to the high turboshaft speed region and described in [11], while the second one is based on semi-empirical relationships among the flow parameter (Φ), the head parameter (Ψ) and the inlet Mach number (Ma) [39][40][24]. These parameters are related to the pressure ratio (β_c), the corrected mass flow ($\dot{m}_{corr}$) and the corrected speed (n_{corr}) through the following set of equations

$$\begin{cases} \Phi = \dfrac{\dot{m}_{corr} R T_0}{\dfrac{2\pi^2}{60} r_{tip}^3 p_0 n_{corr}} \\[4ex] \Psi = \dfrac{2 c_p T_0 \left[\beta_c^{\frac{k-1}{k}} - 1 \right]}{\left[\dfrac{2\pi}{60} r_{tip} n_{corr} \right]^2} \\[4ex] Ma = \dfrac{\dfrac{2\pi}{60} r_{tip} n_{corr}}{\sqrt{k R T_0}} \end{cases} \tag{2.40}$$

where r_{tip} is the compressor propeller radius, p_0 and T_0 are the inlet reference conditions. This model requires only geometrical and operational data. A relationship between Ψ and Φ can be implemented in the following black-box model

$$\Psi = \frac{k_1 + k_2 \Phi}{k_3 \Phi}, \qquad k_1, k_2, k_3 = f(N) \tag{2.41}$$

The parameters k_1, k_2, k_3, modeled with a polynomial function identified by using the experimental data. These data refer to the region where experimental information are available, i.e. the high speed area. Once the parameters k_i are known, the compressor map can be built also into the low compressor speeds region.

In order to guarantee a smooth matching of the models, weighted interpolation function is implemented by ensuring the continuity of the data (compression ratio and compressor efficiency) across the two regions. The matching between black-box and grey-box model is obtained, by introducing a function around the minimum experimental rotational speed (around 80 krpm, inside a region between 75 and 85 krpm). Figure 2.6 reports the simulated compressor map generated by the two models. The Figure shows with black colour the curves obtained with the black box model, whereas the extrapolated curves below 80000 rpm are represented with blue colour.
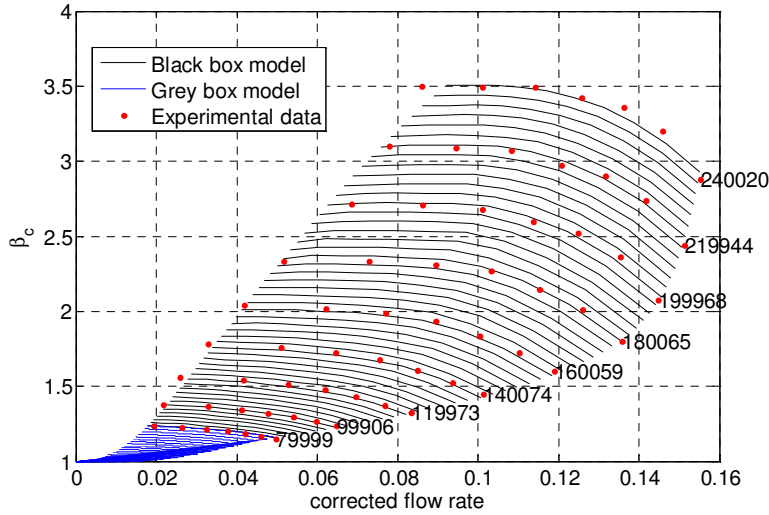
Figure 2.6 - Simulated compressor map

The efficiency calculation is based on the power output of the compressor [11]. The power is linked to the turbo compressor speed and the mass flow rate and can be written as third order polynomial function: as follows:

$$P_{corr} = b_1\dot{m}^3_{corr} + b_2\dot{m}^2_{corr} + b_3\dot{m}_{corr} + b_4$$
$$b_i = f(n_{corr})$$

(2.42)

Once the corrected power is known, the compressor efficiency η_c can be determined from the equality of the equation (2.42) and the definition of the compressor work (later described through the equation (2.50)). Figure 2.7 shows results of efficiency curves at low speeds in blue and the results of fitted efficiency curves at high speed are accurate and present a good fitting respect the experimental data.
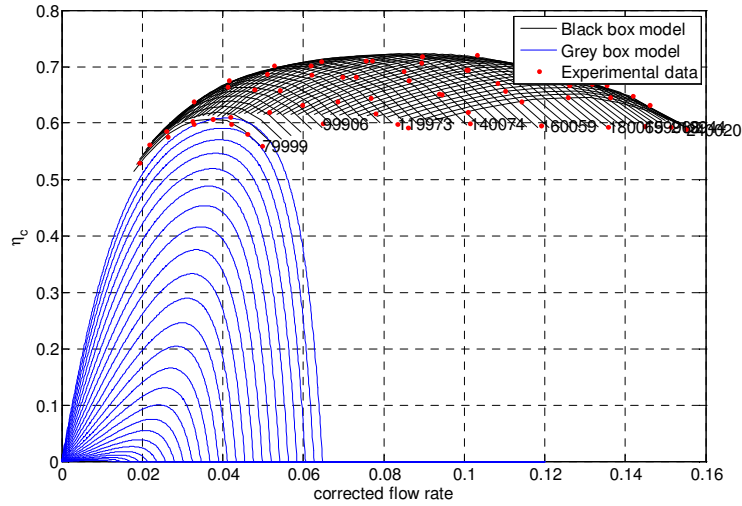
Figure 2.7 - Simulated efficiency compressor map

2.6.2. Turbine model

A turbine grey-box model is applied to simulate the behaviour of such a component. The turbine is modelled assuming the flow through an orifice [36][40].

$$\dot{m}_{corr} = \frac{C_d \Omega p_0}{\sqrt{RT_0}} f(\beta_e) \tag{2.43}$$

where C_d is the discharge coefficient, Ω represents the inlet area and the flow function $f(\beta_e)$ describes the orifice flow in chocked or unchocked conditions

$$f(\beta_e) = \begin{cases} \sqrt{\dfrac{2k}{k-1}\left[\beta_e^{-\frac{2}{m}} - \beta_e^{-\frac{m+1}{m}}\right]} & if \quad \beta_e \leq \left(\dfrac{m+1}{2}\right)^{\frac{m}{m-1}} \\ & \qquad\qquad unchoked\ flow \\ \left(\dfrac{2}{m+1}\right)^{\frac{1}{m-1}}\sqrt{\dfrac{2k}{k-1}\dfrac{m-1}{m+1}} & \qquad chocked\ flow \end{cases} \tag{2.44}$$

The polytropic coefficient m can be found from the definition of the isentropic efficiency

$$\eta_t = \frac{1 - \dfrac{1}{\beta_t^{\frac{m-1}{m}}}}{1 - \dfrac{1}{\beta_t^{\frac{k_e-1}{k_e}}}} \tag{2.45}$$

The isentropic efficiency η_t and the expansion ratio β_t are known from map data. For convenience the value for m is averaged and taken constant for each VGT rack position.

Moreover, the following equation was applied to evaluate the Tip Speed Ratio (TPS), defined as the ratio between the impeller tangential speed and the exhaust gases one

$$TPS = \frac{U_t}{C} = \frac{\pi n_{corr} r_{in}}{30\sqrt{2c_p T_0 \left[1 - \beta_e^{\frac{1-k}{k}}\right]}} f(\beta_e) \tag{2.46}$$

where r_{in} represents the turbine impeller radius, whereas p_0 and T_0 are the inlet reference conditions provided by the manufacturer. The *TPS* and the corrected turboshaft speed are the parameters that allow evaluating the turbine efficiency by means of a polynomial functions

$$\eta_t = a_1 + a_2 n_{corr} + (a_3 + a_4 n_{corr})TPS + (a_5 + a_6 n_{corr})TPS^2 \tag{2.47}$$

The coefficients a_i have to be identified by using the available experimental data for each rack position of the VGT. It is worth noting that the above computational sequence must be applied for each geometry of the inlet stator vanes. For the implementation, a linear interpolation of the variables is applied to compute the values at intermediate VGT position.

The Figure 2.8 represents the curves of reduced mass flow against expansion ratio, for several turbocharger speeds, evidencing a good fitting against the experimental data represented by blue markers. It is worth noting that the turbine model extends the turbine map to the low speed zone.
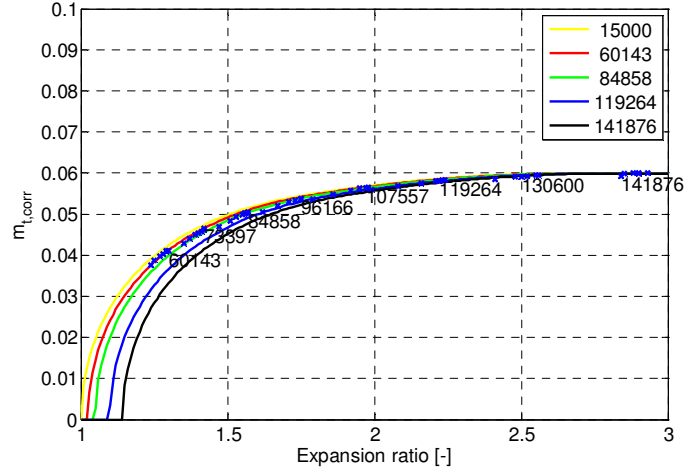
Figure 2.8 - Simulated turbine map.

This turbine model is useful for the proportional scaling of the map, by operating on the surface Ω. So in this way, a similar turbine, but of different sizes can be reproduced.

2.6.3. Turbocharger dynamic model

The coupling interaction of compressor and turbine models is done through the following balance of the powers at the turbocharger shaft

$$\frac{d\omega_{tc}}{dt} = \frac{P_t - P_c}{I_{tc}\omega_{tc}} \tag{2.48}$$

where the powers of turbine and compressor are evaluated with the following equations [38]

$$P_t = \dot{m}_{turb}T_{exh}c_{p,exh}\left[1 - \left(\frac{1}{\beta_e}\right)^{\frac{k_{exh}-1}{k_{exh}}}\right]\eta_t \tag{2.49}$$

$$P_c = \dot{m}_{air}T_{amb}c_{p,air}\left[\left(\beta_c\right)^{\frac{k_{air}-1}{k_{air}}} - 1\right]\frac{1}{\eta_c} \tag{2.50}$$

2.7 Alternator, Battery and AUX Load

For the purpose of the work, the Lundell alternator is assumed. It is described through an efficiency map as function of the engine speed, with values ranging from 30 % to 60 % [41], whereas the battery is modelled as a first order circuit in the SOC state [42]. The model considered for the battery pack consists of N_B cells. Thus the instantaneous battery power is related to the power of each cell as follows

$$P_B = N_B P_C \tag{2.51}$$

Each cell is assumed to be modelled by means of an equivalent static electric circuit characterized by an internal resistance R_{in} and the open circuit voltage V_0 (see Figure 2.9). Then the cell model is

$$V_C = V_0 - R_{in} I_C \tag{2.52}$$

and the power provided by each cell is given by

$$P_C = V_0 I_C - R_{in} I_C^2 \tag{2.53}$$

By substituting (2.53) in (2.52), the instantaneous battery current can be written as

$$I_C = \frac{V_0 - \sqrt{V_0^2 - 4R_{in}P_C}}{2R_{in}} \tag{2.54}$$

where only the solution corresponding to low current is considered. The other solution is not considered because the power dissipated on the battery internal resistance is much lower than the load power.

By assuming that all battery cells are equalized and that the battery is able to provide the requested power P_B, the evolution of the battery state of charge SOC can be obtained by considering a single cell and is represented by the following differential equation

$$\frac{dSOC}{dt} = -\frac{1}{Q_{max}} I_C = \frac{V_0(SOC) - \sqrt{V_0(SOC)^2 - 4R_{in}P_B / N_B}}{2R_{in}Q_{max}} \tag{2.55}$$

where t is the continuous time variable Q_{max} is the maximum battery cell

charge.
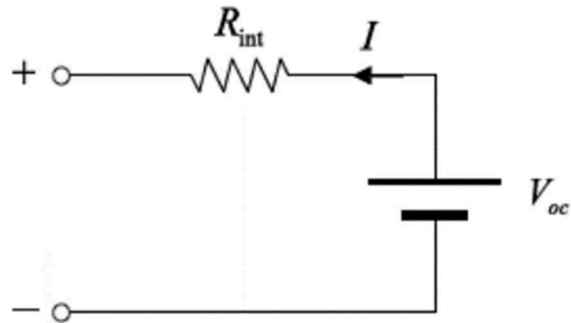
Figure 2.9 – Kirchoff law-based approach to battery modeling.

The simulations were carried out by setting a constant electrical load, equal to 250 W, which is a typical value for the contribution of auxiliaries in automotive engines. It is worth pointing out that electrical absorption for a specific driving cycle is not constant value, but strongly fluctuating, with peaks exceeding 1 kW. An exhaustive list would include all the electric devices that have an influence on the alternator behaviour, such as lightning, the air conditioning, etc., neglected for this study [24].

2.8 Model validation

This section presents the validation of the vehicle-powertrain model, which is performed with respect to experimental data collected on the reference car at the vehicle test rig. The presented study refers to a segment C vehicle equipped with a 1.4 litres turbocharged spark ignition (SI) engine with variable valve actuation (VVA). The analyses were carried out against both NEDC and global WLTC standard driving cycles, which are typically used for passenger cars.

The Figure 2.10a and Figure 2.10b illustrate the speed and gear time histories measured at the test rig and assumed as input for model simulations. The Figure 2.10c shows the comparison between simulated and measured time histories of the engine torque, along the NEDC. The model exhibits good accuracy in simulating the engine torque profile, particularly at high load, while an overestimation occurs when the engine is idling. This result is due to the Start and Stop (S&S) strategy that was

enabled in the real vehicle but not simulated in the model (see plot on the left side of Figure 2.11). Therefore, in idling conditions, the model simulates the torque delivered by the engine to drive the alternator while the real data refer to the engine switched off.

Nevertheless, this discordance at engine idling does not affect the validation results. The good model accuracy in simulating the engine torque is shown in detail in the plot on the right side of the Figure 2.11 that focuses on the time window corresponding to the extra-urban cycle, when the engine operates at high load. Model accuracy is also evaluated via comparison between predicted and measured pressure in the intake and exhaust manifold during engine transient operation.
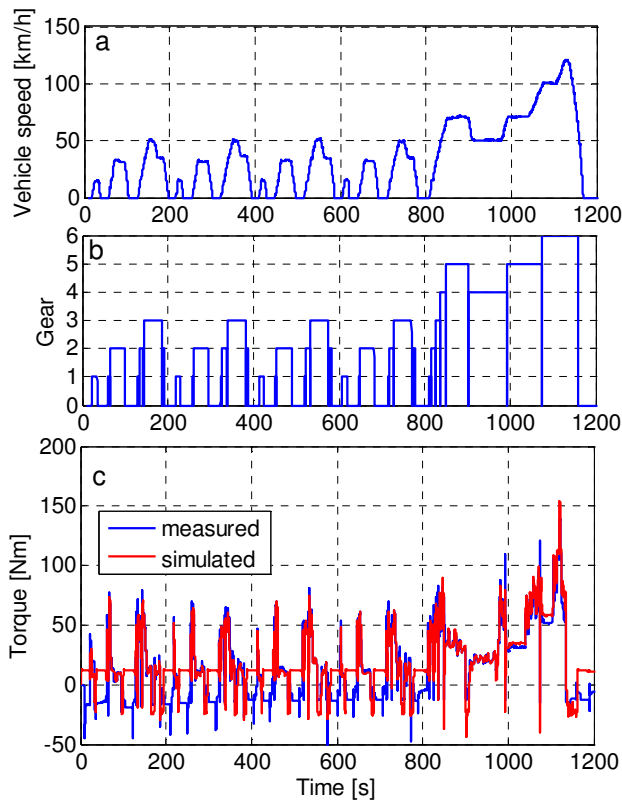
Figure 2.10 - Validation results on the NEDC: a) Experimental vehicle speed; b) Experimental gear; c) Comparison between measured and simulated torque.
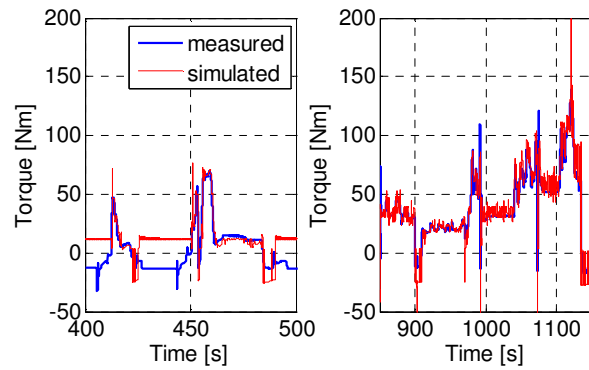
**Figure 2.11 - Comparison between measured and simulated torque
along the urban (left side) and extra-urban (right side) transient
(time windows 400 – 500s and 850 – 1150 s).**

Figure 2.12 and Figure 2.13 focus on the NEDC transient during the extra-urban module in the time window 850-1150 seconds. The former Figure shows a very good agreement of the intake manifold pressure with the measured signal, while an underestimation of about 7 % occurs for the exhaust manifold pressure during low load operating conditions (see Figure 2.13).
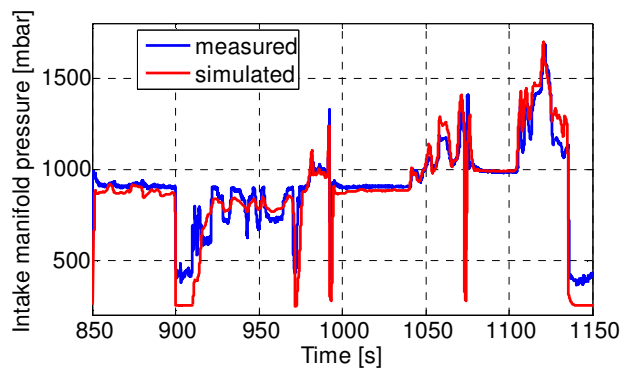
**Figure 2.12 - Comparison between measured and simulated intake manifold
pressure along the extra-urban transient (time window 850 – 1150 s).**
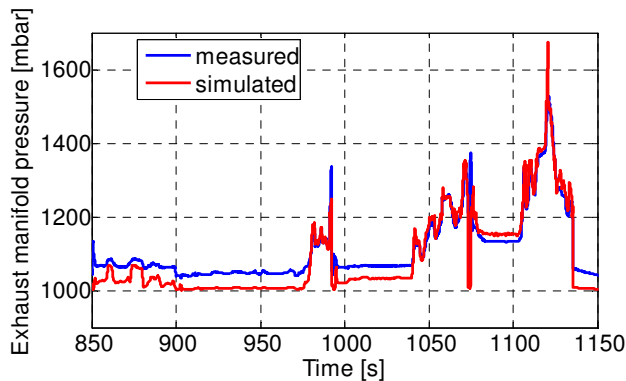
Figure 2.13 - Comparison between measured and simulated exhaust manifold pressure along the extra-urban transient (time window 850 – 1150 s).

The fuel economy and CO_2 emissions evaluated on the NEDC are equal to 16.20 km/l and 144 g/km, respectively, higher than the measured one of 134 g/km. These results differ by approximately 5 - 6 % from the experiments, and it is worth noting that this value can be mostly ascribed to the benefits expected by the S&S strategy [24].

2.9 Benchmarking

A wide database of several vehicles and different engines is available for this study and the simulations have been carried out for multiple combination vehicle-engine. For the sake of brevity only the most useful results have been represented.

The hybridization analysis has been performed for a Large/SUV-segment vehicle equipped with CI turbocharged engine and the WHRs have been analysed on a C-segment vehicle equipped with SI turbocharged engine. The reasons of these choices are explained in the graph of Figure 2.14 where the CO_2 emissions for both gasoline and Diesel powered engines are reported versus the vehicle mass. It is worth noting that the sub-compact and compact passenger cars segments are placed between 800 and 1500 kg and are mainly equipped with SI engines. With the increasing of the vehicle mass, the carmakers adopt always more the CI engines, until Large and SUV segment cars characterized by a mass included between

1500 and 2300 kg.

The WHRs are integrated on gasoline engines to exploit the high temperature of the exhausted gases to achieve the CO_2 target of 2020. This solution is consistent with the limited improvement required with respect to the current status and its easier implementation. This latter comment might appear not in agreement with the maturity of the technology, however WHRs can be considered as add-on components if compared with the hybridization of any powertrain. Such an analysis is in line with today trends for larger light duty vehicles. For more efficient but heavier diesel vehicles, the hybrid technology ensures a relevant saving of fuel and emissions. In the study, the Fiat Ducato Passenger Transport is used as a reference for the Large/SUV segment thanks to the large amount of data available. Such explanation allows illustrating better the potentialities and the benefits of the advanced and innovative technologies for light-duty vehicles.
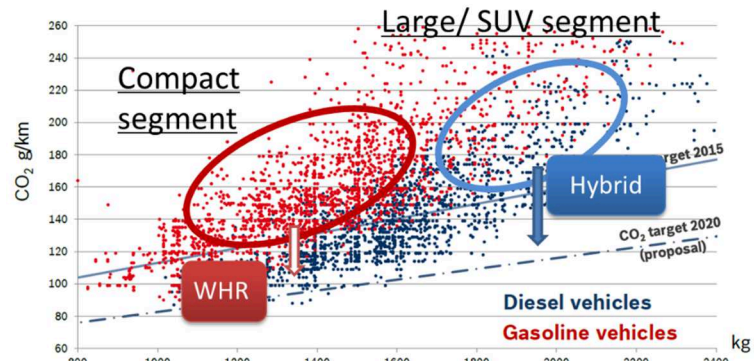
Figure 2.14 - The two limit value curves for the calculation of the passenger cars target in 2015 and 2020 [43] and the possible solutions to fulfil the limits.

The main technical data of the vehicles and engines are listed in Table 2.1.

Table 2.1 - Vehicles and Engines data.

Vehicle	Alfa Romeo Giulietta					Fiat Ducato Passenger Transport				
Vehicle mass	1290 kg + 70 kg (pilot)					2270 kg + 70 kg (pilot				
Vehicle front area	2.04 m^2					5.17 m^2				
Tire rolling radius	0.31 m					0.31 m				
Drag coefficient	0.31					0.31				
Rolling coeff.	0.015~0.025					0.015~0.025				
Diff. gear ratio	3.833					4.933				
Gear ratio	3.900	2.118	1.484	1.116	0.897	3.727	1.952	1.290	0.875	0.673
Engine	1.4 l MultiAir SI Turbocharged					2.3 l MultiJet CI Turbocharged F1A				
Cycle	Otto					Diesel				
Strokes	4					4				
Max Power (kW)	125 (5500 rpm)					107 (3600 rpm)				
Max Torque (Nm)	250 (2500 rpm)					350 (1500 rpm)				
Cylinders	4					4				
Disposition	In - Line					In - Line				
Bore (mm)	72					88				
Stroke (mm)	84					94				
Displacement (cm3)	1368					2287				
Compression ratio	10:1					16.2:1				
Emission standard	Euro 5					Euro 5				

CHAPTER 3

Advanced ICE–PowertrainTechnologies

For the next decades, one of the most promising and effective methodologies to reduce the CO_2 emissions of the vehicle fleet is the improvement of the efficiency of the internal combustion engines. According to the DOE [44], nowadays, outstanding features of drivability and reliability are already assured from the ICE for the transportation vehicles, while future technological improvements are expected to make them substantially more efficient. The increment of the fuel economy due to the engine efficiency improvements can potentially reach the 25 % for light duty passenger vehicles and the 30 % for heavy duty commercial vehicles with accompanying carbon dioxide reduction. Even greater vehicle fuel economy improvement is expected when more efficient engines are coupled with advanced hybrid electric powertrains. Valuable economic and environmental benefits could be achieved by operating on engine combustion, emission controls, fuel injection, turbo-machinery and other advanced engine technologies, that allow obtaining a higher thermal efficiency of the ICEs. For these reasons, the internal combustion engines, both gasoline and diesel ones, continue to play a key role for conventional vehicles. In addition, the integration of these engines with hybrid and plug-in hybrid electric vehicle powertrains together with the use of natural gas and biofuels such as ethanol and biodiesel, can considerably widen the opportunities for enhancement [44]. An important role in the automotive market is also covered by energy storage, electric drive systems and fuel cell technology. The hybridization and electrification of the vehicles are now actively developing by many car companies, thanks to their significant potential in reducing CO_2 emissions.

3.1 Technological improvements

In this section, attractive feasible solutions are researched and presented, through modeling and simulation of vehicles equipped with engines with increasing efficiency. The vehicle model, previously described, is used to evaluate the impact of the technological improvement on the engine efficiency. The results of the analysis are the reduction of CO_2 emissions achievable after the implementation of the technologies in the engine layout. For this purpose, several technologies are taken into account, initially as single contributions and later with combination effects defining a path of development of the engine [43][44]. For passenger cars, the technological improvements can be sufficient to guarantee low costs with quite high efficiency. The explored technological improvements (TIs) of the engines include:

- Friction Reduction (FR),
- Variable Valve Actuation improvement (VVA),
- Extended Recuperaction (Ext.Rec),
- Extreme downsizing (eDZ),
- Cylinder De-activation (CDA),
- Common rail pressure (CRP),
- Low Pressure – Exhausted Gas Recirculation (LP-EGR),
- De-Throttling (dTH),
- Turbocharger Friction (TC FR),
- Lean Gasoline Direct Injection (LGDI).

A brief description of these technologies is presented below.

Friction Reduction (FR)

As it is pointed out in the paragraph (2.4.1), mechanical losses have considerable impact on fuel consumption during urban operations. The engine friction losses represent 1/3 of the passenger car fuel consumption. It is estimated that such losses can be reduced by 20% in the next 5 - 10 years and up to 60% on long term [45][46].

VVA improvement (VVA)

Most of gasoline engines still use an intake throttle valve to regulate air flow rate for load control. The Variable Valve Actuation (VVA) may replace the intake throttle in order to achieve reduction of pumping loss and

specific fuel consumption. An optimized strategy of the VVA can bring to significant reduction of CO_2 emissions up to 3 or 4 % [47].

Extended recuperation (Ext. Rec.)

The impact of the auxiliaries and particularly Air Conditioning (AC) on both greenhouse gas and pollutant emissions are considerable. Typical value for the contribution of auxiliaries in automotive engines is about to 250 W (used for Alfa Romeo Giulietta equipped with 1.4 l MultiAir SI Turbocharged engine). For the Fiat Ducato Passenger Transport equipped with 2.3 l MultiJet CI Turbocharged F1A engine the value is set to 400 W. It is worth pointing out that electrical load for a specific driving cycle is not a constant value, but strongly fluctuating, with peaks exceeding 1 kW. The contribution on the carbon dioxide emissions of the AC is very important. However, in the case of standard cycles, the effect of the auxiliaries on fuel consumption is partially hidden by the improvement of the engine efficiency because the auxiliaries running increase the load and, therefore, the engine efficiency. In order to reduce the effect of the auxiliaries on the engine efficiency and consequently on the fuel consumption, the electrification of the some components could lead to useful fuel economy [48].

Extreme downsizing (eDZ)

The engine downsizing is the most popular solution in light duty engines. Downsizing refers to the practice of automotive engineers to reduce the displacement and/or the number of cylinders in an engine and affects the design of the entire powertrain. This technique is currently widely used in light-duty engines to effectively improve fuel efficiency and reduce both regulated and greenhouse gas emissions. Some OEMs claim that 50 % engine displacement downsizing could provide up to 30 % fuel economy benefit [47].

Cylinder De-Activation (CDA)

The variation of the engine displacement, also called cylinder de-activation, is a particular engine technology capable of improving considerably fuel economy without penalizing of the performance. The same engine with variable displacement by deactivating one or more cylinders when it operates at low load. The full displacement is activated when the power demand by the driver is higher. This strategy results in a

considerable reduction of fuel consumption and CO_2 emissions. An optimal integration of the variable displacement into the powertrain system and an opportune control strategy are necessary in order to achieve the maximum benefit from this technology. The variability of the displacement is constrained by the capability of the engine to meet the driver torque demand and the auxiliaries load with some of the cylinders disabled. Some drawbacks may be torque fluctuations that introduce noise, vibration and harshness (NVH) [48].

A number of companies have developed cylinder deactivation systems, with varying degrees of success. First experiments with multiple-cylinder engines during WWII, were re-attempted in 1981 on Cadillac's ill-fated L62 "V8-6-4" engine. In 1981 Alfa Romeo developed in collaboration with the University of Genoa a semi-experimental variable displacement engine version of the Alfa Romeo Alfetta, called Alfetta CEM (Controllo Elettronico del Motore, or Electronic Engine Management. In 1982 Mitsubishi developed its own variable displacement in the form of MD (Modulated Displacement) which proved that the technology.

Common Rail Pressure (CRP)

Modern electronically controlled common-rail fuel injection systems allow high injection pressures that can be controlled independently from engine speed and fuel injection quantity. Advances in electronics have allowed obtaining a complete control of injection timing, duration, and dosing processes, including multiple injections and high-accuracy fuel delivery. Optimization of injection rate shaping with new injectors can simultaneously improve the specific fuel consumption and pollutant emissions of the engines [49].

Low Pressure Exhausted Gas Recirculation (LP EGR)

For a Diesel engines, several layouts of the EGR system are suggested for improving engine efficiency and emissions [50]. In the low pressure (LP) EGR system, the exhaust gases are extracted from downstream of the after-treatment devices, and introduced upstream of the compressor. The simultaneous application of high pressure EGR (HP EGR) and LP EGR to Diesel engines has a potential to optimize fuel economy and emissions. The specific fuel consumption tends to decrease with the increasing of the LP EGR portion. This tendency is followed by the exhaust manifold pressure that drops as the LP EGR portion increased. Indeed, the nozzle of VGT

opens more widely with the increasing of LP EGR portion to maintain a constant boost pressure, which results in a lower back-pressure and a lower pumping loss. Thus, the specific fuel consumption (SFC) decreases with the increase of LP EGR portion [51].

De-Throttling (dTH)

Various de-throttling concepts are proposed in literature [52]. An important de-throttling of the intake system is obtained with the VVA systems. This technique allows changing the mass air flow rate without the regular use of the throttle. However, an extra component and complicated control strategies have to be adopted. The combining of the deThrottling and VVA system could bring a reduction in the specific fuel consumption, but also higher noise levels radiated by the intake mouth due to the pressure waves travelling through the intake ducts, which are not properly damped by the throttle valve. The effect of the throttle removal on Diesel engines is not relevant enough in terms of CO_2 reduction.

Turbocharger friction (TC FR)

Turbo-charging and super-charging are techniques to increase the volumetric efficiency of the engine, by increasing the intake air flow. Thus, performance and fuel efficiency can be improved. Generally, turbo-chargers are driven by the expansion of the exhaust gases in the turbine, while super-chargers are boosted by an accessory belt similar to a power steering pump. Both works as air compressors, by increasing intake air pressure and, consequently, the air mass for the combustion. This leads to more fuel to be burned and, therefore, more power generated. Downsized engines could be used without loss of performance or drivability if matched with turbo or super-chargers. Turbochargers have good efficiency but the mechanical connection between turbine and compressor can be enhanced. In order to improve the efficiency of the turbocharger, several ideas are suggested, among others the minimization of the turbo inertia and the reduction of the turbocharger friction by using floating ring bearings [53].

Lean Gasoline Direct Injection (LGDI)

Lean Gasoline Direct Injection (LGDI) combustion is a promising technical path for achieving significant improvements in fuel efficiency while meeting future emissions requirements. The technique consists in a gasoline (initially highly pressurized) direct injection into the combustion

chamber of each cylinder by means of a common rail system. The engine can work in three combustion modes: ultra lean burn, stoichiometric, and full power output. In some applications, gasoline direct injection enables a stratified fuel charge (ultra lean burn) combustion for improved fuel efficiency, and reduced emission levels at low load [54].

3.1.1. Modeling

To analyse the influence of the technological improvements (TIs) reviewed before the simplified modelling approach described into Chapter 2 has been modified to account for the contribution of each technology. The Willans line method (equation (2.8)) is used to evaluate the torque delivered, by splitting the terms related to both mechanical and pumping losses from the available torque generated by the fuel. Furthermore, three adimensional parameters (a, b and c) allows quantifying the impact of those technologies on the torque balance.

$$T_e = a \cdot e \eta_{id} H_{LHV} \frac{\dot{m}_f}{\omega} - b \cdot p_{loss} \frac{V_d}{4\pi} - c \cdot \frac{(p_{exh} - p_{intake})V_d}{4\pi}$$ (3.1)

Each advanced technology causes a different effect on the several terms of efficiency or loss. Therefore, the effective torque and engine efficiency will change. The implementation of this engine sub-model into the vehicle-powertrain model allows estimating the fuel economy and CO_2 reduction with respect to the conventional vehicle.

A brief explanation of each contribution is addressed and shown afterward. The VVA is a technology that affects both the parameters a and b, by operating on the torque available and pumping losses. Furthermore, the parameter a can modify the effect of the LGDI and CRP on the combustion. The mechanical losses are parameterized by the parameter b. Finally, the LP-EGR, the de-Throttling and Turbocharging influence the manifold pressures, modifying the parameter c can be used to describe the variation of the pumping losses. The Extended Recuperation allows reducing the auxiliaries load. For both gasoline and diesel engines, several simulations have been carried out, by varying the parameters a, b and c, as well as to set different values of the displacement V_d to take into account of the effect of the downsizing and the cylinder de-activation.

Before performing the analysis and the TIs influence on the CO_2 reduction, sensitivity analysis has been carried out. This allows evaluating

which technology is more effective on the CO_2 reduction. Figure 3.1 represents the results of 125 simulations that have been performed along the NEDC with a 1.4 l MultiAir SI engine 170 hp, modifying the parameters with steps of 0.02. The graphs show that the parameter *a* may cause a larger variation of CO_2 emissions, with respect to the other parameters. As expected, it would be more convenient to apply the technologies that affect the thermodynamic efficiency and the combustion. A variation of the 0.1 of the parameter *a* could bring to a reduction of about 16 % of carbon dioxide emissions.
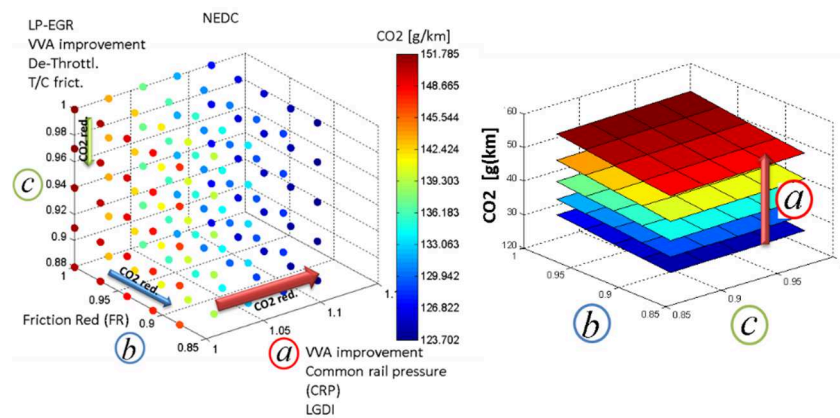
Figure 3.1 – CO_2 emissions results of the sensitivity analysis along the NEDC, ranging the *a*, *b* and *c* parameters (left side) and CO_2 emissions results of the simulations along the NEDC, ranging the *b* and *c*, parametrised against the *a* (right side).

3.1.2. Results

The reductions of CO_2 emissions for each technological improvements are reported in literature [43]. Starting from these savings, the values of the parameters for each one of TIs can be evaluated. To account for more than one technology and evaluate the potentialities of combining them all, a sequence of TIs has been followed for both SI and CI engines [43]. Again Table 2.1 reports the specification of both the engines. The CO_2 emissions evaluated on the NEDC for the vehicles Alfa Romeo Giulietta equipped with the 1.4 MultiAir SI engine and Fiat Ducato Passenger Transport equipped with 2.3 MultiJet CI engine are equal to 144 and 234 g/km (baseline cases), respectively. These results differ by approximately 5 - 6 % from the experimental data.

For SI engine, the results are shown in Table 3.1 and Figure 3.2.

Table 3.1 - Potential CO$_2$ reduction of the innovative technologies along the NEDC for SI 1.4 l TB MultiAir 170 hp.

Configuration	Parameters	CO$_2$ red. [%] Single reduction / Global reduction
CV	a = 0; b = 0; c = 0; AUX = 250W.	
CV + **FR**	a = 0; b =**-0.8**; c = 0; AUX = 250W.	2.2 / 2.2
CV + FR + **VVA**	a = **0.2**; b =-0.8; c =**-0.2**; AUX = 250W.	1.9 / 4.1
CV + FR + VVA + **Ext.Rec.**	a = 0.2; b =-0.8; c =-0.2; AUX = **150W**.	0.6 / 4.7
CV + FR + VVA + Ext.Rec.+ **CDA**	a = 0.2; b =-0.8; c =-0.2; AUX = 150W; **1 cyl. deact**.	9.2 / 13.8
CV + FR + VVA + Ext.Rec. + CDA + **LGDI**	a = **0.7**; b =-0.8; c =-0.2; AUX = 150W; 1 cyl. deact.	4.3 / 18.1
CV + FR + VVA + Ext.Rec. + **eDZ**	a = 0.2; b =-0.8; c =-0.2; AUX = 150W; **1 cyl.elimin**.	14.3 / 19.0
CV + FR + VVA + Ext.Rec. + eDz + **LGDI**	a = **0.7**; b =-0.8; c =-0.2; AUX = 150W; 1 cyl. elimin.	4.5 / 23.5
CV + FR + VVA + Ext.Rec. + **eDZ+CDA**	a = 0.2; b =-0.8; c =-0.2; AUX = 150W; **1 cyl. elimin. + 1cyl. deact**.	16.3 / 21.0
CV + FR + VVA + Ext.Rec. + eDZ + CDA + **LGDI**	a = **0.7**; b =-0.8; c =-0.2; AUX = 150W; 1 cyl. elimin. + 1cyl. deact.	5.4 / 26.4

The sum of contributes related to engine friction reduction, VVA

improvement and the extended recuperation gives a decreasing of CO_2 emissions of about 5 %. The next steps follow three alternative ways: the cylinder deactivation, the downsizing and the combination of these two. Each one of these three steps is furtherly coupled with the LGDI technology, as last step. The results show a reduction of CO_2 of about 18.1 %, 23.5 % and 26.4 %, respectively for the three followed ways. As expected, the major contribution is linked to the downsizing and the coupling with the cylinder deactivation function.
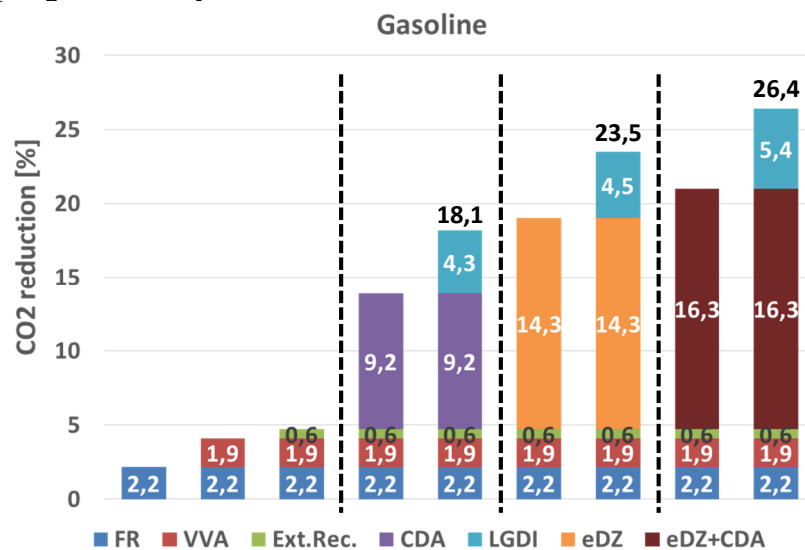
Figure 3.2 - Potential CO_2 reduction of the innovative technologies along the NEDC for SI 1.4 l TB MultiAir 170 hp.

Compression ignition engines account only for some of the improvements listed above, which are reported in the Table 3.2 and in the histogram of Figure 3.3. The contributions of both the deThrottling and the Turbocharger friction reduction are almost neglected with respect to the other technologies. However, the sum of the possible enhancements lead to 7.2% of reduction of CO_2 emissions, then the downsizing reach the 17.5 %. Generally, CI turbocharged engines are more efficient than the SI ones, therefore, the expected improvements are lower. The obtained results are the basis for the next analysis, which has been performed to understand the possible innovative solutions that may fulfil the stringent limits about the fuel consumption and emissions imposed by European Commission.

Table 3.2 - Potential CO_2 reduction of the innovative technologies along the NEDC for CI 2.3 l MultiJet F1A.

Configuration	Parameters	CO_2 red. [%] Single reduction / Global reduction
CV	a = 0; b = 0; c = 0; AUX = 250W.	
CV + **CRP**	a = **0.2**; b = 0; c = 0; AUX = 250W.	2.1 / 2.1
CV + CRP + **LP EGR**	a = 0.2; b = 0; c =**-0.2**; AUX = 250W.	1.7 / 3.8
CV + CFP + LP EGR + **FR**	a = 0.2; b =**-1.2**; c =-0.2; AUX = 250W.	3.2 / 7.0
CV + CFP + LP EGR + FR + **dTH**	a = 0.2; b =-1.2; c =**-0.6**; AUX = 250W.	0.1 / 7.1
CV + CFP + LP EGR + FR + dTH + **TC FR**	a = 0.2; b =-1.2; c =**-1.0**; AUX = 250W.	0.1 / 7.2
CV + CFP + LP EGR + FR + dTH + TC FR + **eDZ**	a = 0.2; b =-1.2; c =-1.0; AUX = 250W; **1 cyl.elimin**.	10.3 / 17.5
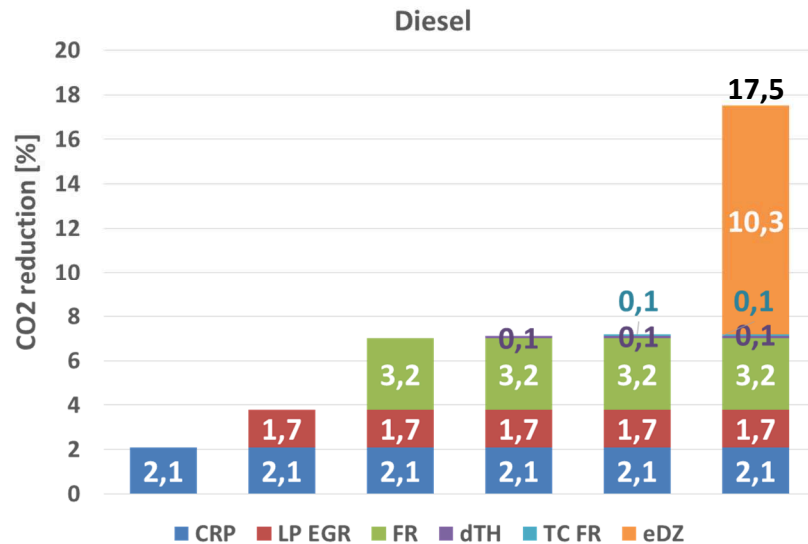
Figure 3.3 - Potential CO₂ reduction of the innovative technologies along the NEDC for CI 2.3 l MultiJet F1A.

3.2 Hybridization

The conventional vehicles are mostly fueled with gasoline and diesel, while the hybrid and electric propulsion systems present an energy storage system and the propulsion is obtained at least by an electric motor [23]. First applications of the hybridization on the vehicles allowed obtaining an important reduction of fuel consumption; several studies available in literature show a reduction of fuel consumption up to 40% [4]. However, such numbers must be carefully analysed because the fuel consumption and CO_2 emissions of the hybrid vehicles depend sensitively on the driving profile assumed. In addition, another relevant issue worth to be considered is the cost, which increases proportionally to the reduction of CO_2.

A classification of several kind of vehicles, based on the source of energy, is presented in literature [55]: hybrid electric vehicles (HEVs), purely electric vehicles (EVs) and fuel cell vehicles (FCHVs). The first one is built by the combination of the internal combustion engine and an electric motor, matched to the powertrain in several point of the driveline. Instead,

EVs and FCHVs do not use the fossil fuel and their development is influenced by both battery and fuel cell technology respectively, as well as charging infrastructures and hydrogen infrastructures. Although EVs and FCVs are considered the cleanest alternative propulsion systems for automobiles in the future by accounting for a Tank-to-Wheels analysis, will probably be not ready for mass production in the next few years. Therefore, several real limitations of their development occurs: high initial cost, unavailability of the infrastructures for EV technology, short driving range, high charging time and small passenger and cargo space [56].

A high variety of hybrid powertrains with different configurations are nowadays considered as valid candidates towards the achievement of sustainable mobility worldwide. The most typical classification of hybrid electric vehicle (HEVs) architectures consists of series HEVs (SHEVs) and parallel HEVs (PHEVs). The rapid development of electric components (primarily the battery pack) along with the diffusion of the plug-in concept motivates for the renewed interest into the series architecture [42]. On the other hand, the advantages of parallel architectures in terms of efficiency and light weight due to hybridization are widely recognized in the literature [56].

The series hybrid has an electric traction system, where the wheels are driven by the electric motor and can recover kinetic energy during braking phases. This recovered energy is stored into a battery and/or supercap bank and is made available to be re-used again during accelerations or for other functions. An ICE is located upstream the entire powertrain to convert the chemical energy available in the fuel to electric energy. The advantage of this structure is the complete decoupling of the electric motor generator from the ICE. However, the flexibility in coupling EMG and ICE+generator may be limited by the size of the battery, which acts as buffer. If the size of the battery/supercap store is high and the electric motor generator (EMG) is small, the system is called 'range extender': the EMG runs in high efficiency conditions to recharge the battery continuously [4]. The series connection can also represent the starting point for the introduction of the fuel cell hybrid vehicles, with fuel cells in place of the thermal engine [42]. If a FC system is used as a prime energy converter there is also the need for a battery to recover energy during braking as well as for system start-up. FC hybrid vehicles (FCHVs) exhibit a typical series hybrid structure, if works as range extender, otherwise as power supply for auxiliaries [4].

In the parallel hybrid, the combination of the mechanical power of both ICE and electric traction motor generates the traction torque. The main advantage of this kind of structure is that the losses derived by the connections of multiple converter chain of the series configuration are avoided. The mechanical power from the ICE is transferred almost directly to the wheels. Of course, there is a broad variability in the placement of the EM and the way it is coupled to the mechanical drive train. The electric motor generator (EMG) can be located either on the same axle of the thermal engine or on different axles. The simplest and cheaper layout is to have a conventional mechanical ICE traction drive on the front axle, and an additional purely electric motor on the rear axle. This configuration presents the disadvantage of a limited regenerative braking. There are several other ways to couple the EMG to the mechanical drive, namely P1, P2, P3 and P4, as depicted in Figure 3.4.
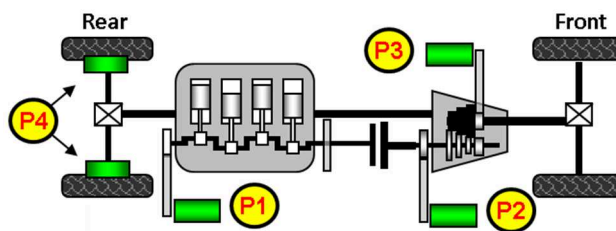
Figure 3.4 – Parallel hybrid electric vehicle configurations.

The P1 and P2 layouts consist of an electric motor generator that has the same rotational speed as the ICE. In the former case, the EMG is mounted on the crankshaft, and in the second case the EMG is integrated between the crankshaft and the gearbox. With the placement of the EMG on the output of the gearbox (P3) and, basically, in the configuration P4 also, the rotation speed is defined by the transmission shaft. With the motor on the axle that is not powered by the ICE, a four-wheel is obtained with configuration P4. More solutions have been already explored in literature, i.e. the connection of the EMG to the differential gear box with an additional (planetary) gear. The main hybridization configuration of the vehicle are shown in this Chapter, by modeling the hybrid vehicle-powertrain and analysing the results of the simulations. In the PHEV drive train, when the ICE operates at low efficiency or when a contribution to the traction is needed, the electrical drive components are activated. In such a case, the electric motor power is only a part of the vehicle total power [57]. With an increasing degree of electrification, the following main

applications can be obtained:
- starter–generator;
- vehicle launch or at least launch assist;
- load enhancement for the ICE for faster warm-up and better efficiency;
- boosting/acceleration assist;
- regeneration (recovering of kinetic energy during deceleration);
- electric drive during manoeuvring; and
- full electric driving during limited periods, for example, urban zero emission driving.

Among these functionalities, Stop & Start is a technology, which has demonstrated to save about 5 % of fuel by switching off the engine when the vehicle is stopped, such as in front of a traffic light, and restarting the engine instantly when the driver pushes back the pedal brake to proceed.

These functionalities were simulated by the conventional powertrain modular model, described in the Chapter 2, by adding the model of the EMG and the related electrical components. The scheme is sketched in Figure 3.5. The EMG model relies on of its efficiency maps where the values of both continuous and maximum applicable torque depend on the size of selected electric machine. The inputs of the EMG model are the demanded torque and rotational speed; the outputs are the delivered electric power and torque. It is worth noticing that this model can be used to manage the EMG either in motor mode or in generator mode. The inverter is modeled through an average value of electrical efficiency assumed equal to 0.8. In addiction, a battery with useful capacity of 0.8 kWh is modeled as a first order circuit with the SOC as state variable as described in paragraph 2.7. Furthermore, a supplementary weight (about 120 kg) related to the entire electrical plant (EMG, battery, inverter, transmission) is taken into account for the evaluation of the CO_2 emissions.
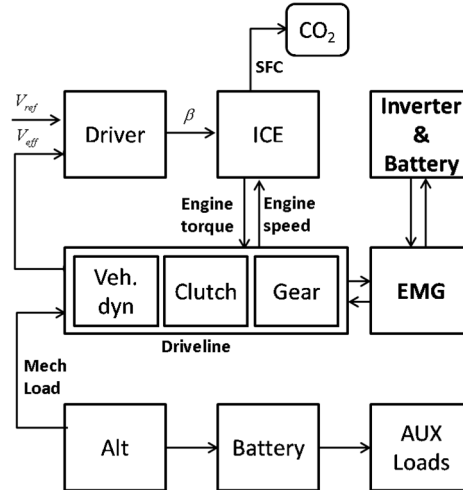
Figure 3.5 - Hybrid vehicle-powertrain model framework.

The NEDC cycle is chosen to evaluate the CO_2 saving potentials after the integration the hybridization components in the powertrain of a light-duty vehicle. In all studied cases, the constraint to recover the initial battery SOC at the end of the driving cycle is imposed. The simulations performed to evaluate the benefits of the hybridization refers to a Large/SUV segment (Fiat Ducato Passenger Transport) vehicle equipped with a 2.3 l turbocharged compression ignition engine; its main technical data are listed in Table 2.1. The CO_2 emissions evaluated on the NEDC for this vehicle is equal to 234 g/km. Intelligent energy management defines the strategies and the power splitting between the two propulsion systems, as well as the operating modes of the EMG. The energy recovered during braking manoeuvres and the charging energy derived from the alternator are stored in the battery and can be exploited as a contribution to boost the vehicle. If the SOC at beginning and at end of the testing manoeuvres are different, the results for CO_2 reduction analysis may not be meaningful. Indeed when the battery energy is depleted either regenerative braking or the engine should compensate for it with the latter option is not useful for CO_2 reduction. Indeed, if the electrical energy for this additional EMG torque assist cannot be compensated by the energy obtained by regenerative braking, there are no advantages in terms of CO_2 reduction. Such a case should request a recharge of the battery from the ICE, which would be overloaded, with consequently additional fuel consumption. Therefore, an

optimal EMG control has to manage the power splitting and balance the energy recovered by both the regenerative braking and recharging, fulfilling the SOC constraint, in order to maximize the fuel saving.

3.2.1. Belt Starter Generator (BSG) – P1

Among the parallel hybrid electric vehicle layouts, the P1 configuration uses an EMG connected to the shaft of the engine through of a belt. The power capacity of such a belt drive is limited to low values of power, around 13kW with a voltage level of 48 V. Furthermore, the power transmission is fulfilled in both directions. For real applications a bi-directional belt tensioner has to be installed to make the on-board implementation feasible. Usually, such a system is named 'belt starter generator' (BSG) or 'belt alternator starter' (BAS). Several investigations show the high interest of the automotive industry towards the potentials of 48 V Belt-Starter-Generators [4][58].
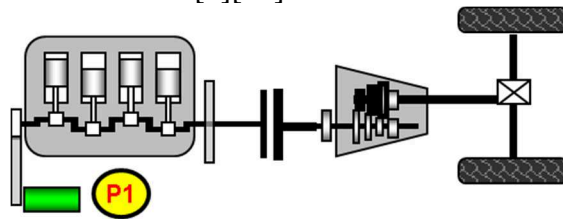
Figure 3.6 - Parallel P1 hybrid electric vehicle configurations.

The characteristics of the electric motor generator used as BSG and the strategies adopted are described in the Table 3.3.

Table 3.3 – P1 EMG technical data and strategies.

Hybrid Configuration	Voltage [V]	Peak Power [kW]	Max Torque [Nm]	Strategies		
				A	B	C
BSG (P1)	48	13	60	Alt.	Alt.+ Reg.brak.	Alt.+Reg.brak.+ Traction (40km/h)

Simulations of three P1 hybrid applications have been carried out. The applications gradually increase the number of possible functionalities, with always increasing electrical support:

A) Alternator function;
B) Alternator function + Regenerative braking;
C) Alternator function + Regenerative braking + Traction function.

The results of the performed simulations by implementing the several P1 applications (A, B and C), are shown in the Figure 3.7, Figure 3.8 and Figure 3.9. The middle graph of Figure 3.7 indicates the BSG operation along the NEDC (see upper graph of Figure 3.7) when the strategy A is applied (1 – motor mode, 0 – recharge mode, -1 – generation mode), showing that the EMG works as alternator with high efficiency along the whole cycle. The bottom graph of Figure 3.7 shows the power of recharge (see red line) quite low.
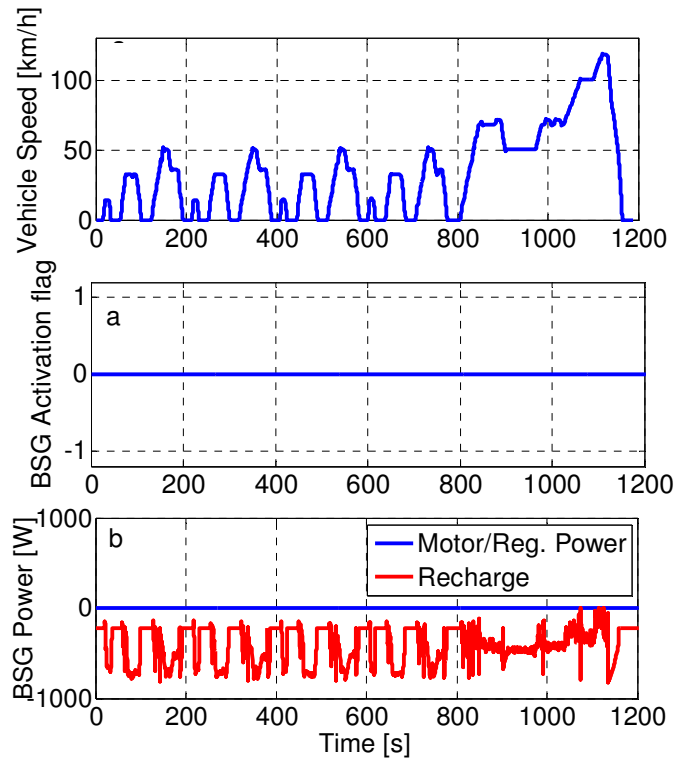
Figure 3.7 - Simulation results of the strategy A along the NEDC: a) Activation flag for BSG (modes: 1 – motor, 0 – recharge, -1 – generation), b) BSG power.

The B operation of the BSG considers also the regenerative braking, therefore in the Figure 3.8 are represented the EMG activation flag and the power recovered during the regenerative phases. It is worth noticing that the recovered power by the regenerative braking reaches almost 1 kW and could be useful to feed the auxiliaries or to be stored in the battery. The Figure 3.9 exhibits the results of the functions of the strategy C. The boost state is limited to the urban phases (ECE) with vehicle speed under 40 km/h and could occur in cases of high acceleration rates required by the driver (along the NEDC are not needed). It is worth noticing that for strategy B the recharging of the battery must be enhanced by using the mechanical energy from the engine to compensate for the extra power required during the boosting phases.
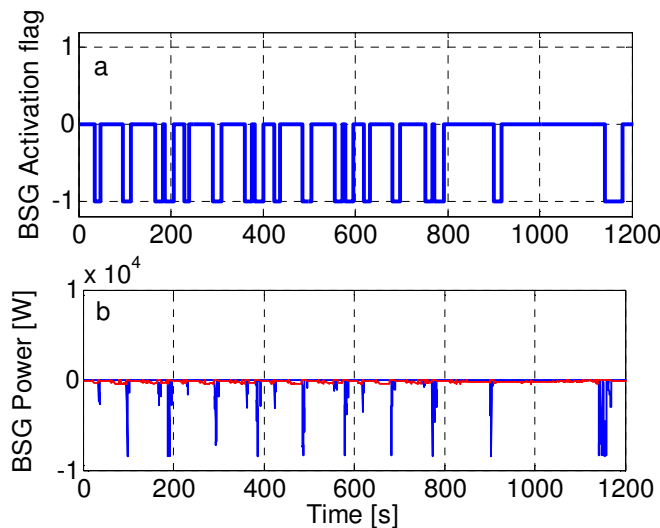
Figure 3.8 - Simulation results of the strategy B along the NEDC: a) Activation flag for BSG (modes: 1 – motor, 0 – recharge, -1 – generation), b) BSG power.
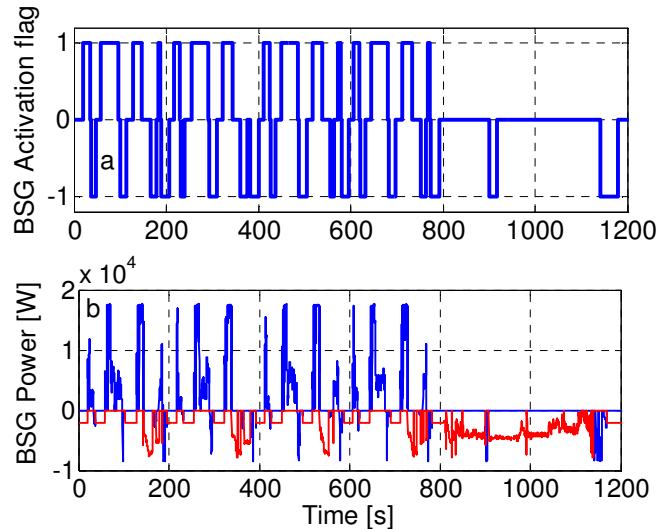
Figure 3.9 - Simulation results of the strategy C along the NEDC: a) Activation flag for BSG (modes: 1 – motor, 0 – recharge, -1 – generation), b) BSG power.

The overall results are summarized in Figure 3.10 that shows the reduction of CO_2 emissions achieved with the P1 implementation, for the different application functions investigated. As expected, by increasing the degree of electrification of the vehicle (i.e. moving from strategy A towards strategy B), the benefits are enhanced with a reduction of CO_2 up to 11 % (see red bar of the Figure 4.2). Although the BSG boost contribution is quite high, resulting in a significant discharge of the battery, the recharge phases and the regeneration braking guarantee the recovery of the SOC at the end of the cycle. This leads to evaluate the maximum achievable CO_2 reduction. The last three bars of Figure 3.10 reports on the integration of the TIs with hybridization. For a detailed description of TIs, the reader is addressed to paragraph 3.1. P1 hybridization added to the engine with TIs follows a different trend if compared to the first three results, offering the maximum benefit with the implementation of strategy B. Moreover, the CO_2 reduction due to the single hybridization for the TIs + P1 configurations (last three bars) are lower than the results of the single P1 implementation (first three bars): 6.2 %, 10.9 % and 6.6 % against 6.7 %, 8.7 % and 11 %, for the strategies A, B and C, respectively. These lower influence of the hybridization on the entire CO_2 reductions can be due to the used strategy, which is optimized for the conventional engine and also exploited for the engine with TIs. The rigid cycle-dependent strategy

constraints the engine to works in the same operation conditions (speed and torque) of the not optimized one (without the TIs implementation), but in different conditions of efficency. The P1 configuration, which applies the strategy C with TIs (last bar) reports on the smaller reduction of CO_2 with respect to the single hybridization contribution (third bar). This is due to an extra-load of the engine for the additional recharging of the battery, to recover the SOC at the end of the cycle. Such a condition leads to a lower saving because the engine works in a region away optimal efficiency area. However, values above the 23 % of CO_2 reduction are achieved for the last three configurations, thanks to the sum of the aliquots of hybridization with the TIs, which contribute with the 17.5 %. The total maximum reduction of CO_2 reaches about the 25 % with the strategy B. The development of an optimized strategy for each cycle, vehicle and engine, based on dynamic programming DP, equivalent consumption minimization strategy ECMS, etc. methodologies, could further reduce the CO_2 emissions and fuel consumption.
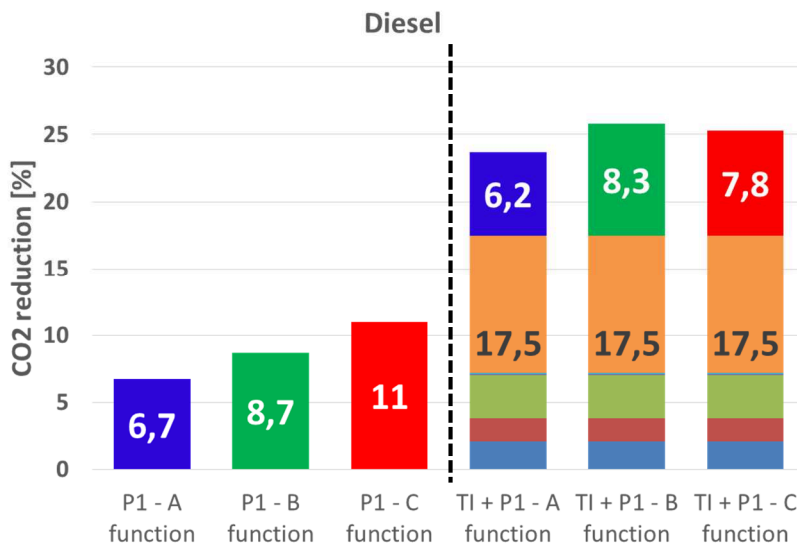
Figure 3.10 - Summary of the CO_2 saving potentials obtained along the NEDC by the implementation of the P1 BSG in the vehicle.

3.2.2. Integrated Starter Generator (ISG) - P2

The P2 hybrid design configuration consisted of an integrated electric motor/generator (ISG) placed between the internal combustion engine and the transmission (see Figure 3.11). It is coupled by a gear train.
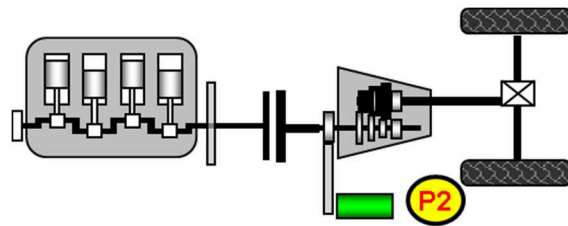
Figure 3.11 - Parallel P2 hybrid electric vehicle configurations.

This kind of mechanical transmission allows much higher power than a belt drive though is more costly, as specified in Table 3.4. EMG is connected to the crankshaft on the gearbox input and the clutch is mounted between ICE and EMG. This configuration allows decoupling the combustion engine, from the rest of the powertrain, thus minimizing both drag and pumping losses during pure electric mode and regeneration operations.

The simulations are performed by using the P2 for both functions motor and generator with the strategy C already described in section 3.2.1. Here, different limitations on the vehicle speed during electric mode operations are applied. The results are shown in the histogram of Figure 3.12. Three main results are reported and are specific for conditions with restriction on the utilization of the electric motor for 20, 40 and 60 km/h (see Table 3.4). The increases the use of the ISG with the speed limit. Therefore, the battery undergoes to more severe operations due to deep discharge phases during the cycle a larger request for charging. The maximum achievable benefit is around 20 % of CO_2 emissions, with a boost limitation of 60 km/h. Although the benefits tends to increase with a broaden employment of the P2 motor during the cycle, the savings follow a different trend if the engine is already optimized with the TIs. Less enhancement is seen for limitation at 40 km/h. It implies a recharging of the battery by the ICE during the extra-urban cycle. The operating points of the thermal engine move towards conditions with higher SFC to satisfy the request of electrical energy for the battery. The reducing of fuel consumption (and CO_2 emissions) is not significant enough (about 10.9 %) with respect to the

other cases.

Table 3.4 –P2 EMG technical data and strategies.

Hybrid Configuration	Voltage [V]	Peak Power [kW]	Max Torque [Nm]	Strategies		
ISG (P2)	48	22	60	Reg.brak.+ Traction		
				Speed Limitation: **20** km/h	Speed Limitation: **40** km/h	Speed Limitation: **60** km/h
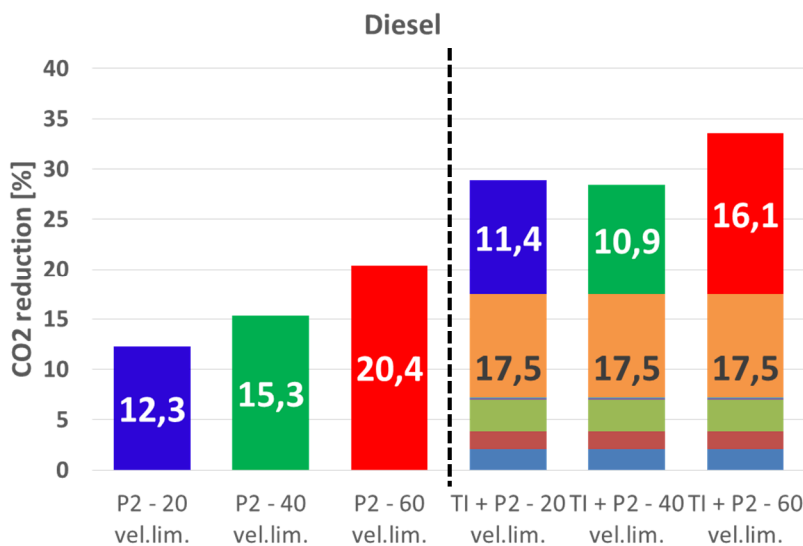
Figure 3.12 - Summary of the CO₂ saving potentials obtained along the NEDC by the implementation of the P2 EMG in the vehicle.

The P2-hybrid topology maximizes its potential thanks to the ICE decoupling from the powertrain. On the other hand, to remove the friction losses of the electric motor generator during the conventional operation modes, a clutch is added between the EMG and the gear train. In such a way, an important loss is removed and a greater saving is obtained.

Although the use with the limitation at 40 km/h does not guarantee the best

results, this has been considered for the comparison with the other hybrid configurations at the same speed limits.

3.2.3. Performing Efficient Transmission (PerfET) – P3

This configuration of hybrid vehicle is obtained by a combination of an electric machine linked to the gear-box output shaft of a conventional powertrain (see Figure 3.13). A clutch is mounted between the gearbox and the electric machine. If the EMG is connected to a Non Manual Transmission, such a configuration is useful to solve the torque gap during the gear shift manoeuvres; therefore, making Non Manual Transmission competitive with respect to the more expensive conventional AMT. The target of PerfET is to make the powertrain more efficient with the functionalities of a hybrid vehicle, thus enhancing also the drivability, thanks to its configuration and structure. PerfET is an affordable hybrid solution for passenger cars. Such an architecture has been developed by Magneti Marelli [59].
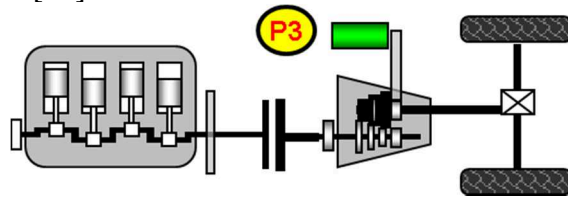
Figure 3.13 - Parallel P3 hybrid electric vehicle configurations.

The characteristics of the electric motor generator used as P3 are described in the Table 3.5, together with the control strategies adopted.

A typical manoeuvre to evaluate the increasing of the performance is a shift first to second gear, at low power (low gas pedal), where the target is to fulfil completely the torque gap occurring when the clutch is opened. The result is the application of a torque almost constant to the wheels and consequently a constant longitudinal acceleration on the vehicle.

The Figure 3.14 shows for a 1.2 l SI engine: a) the thermal engine and primary shaft (i.e. clutch) speeds, b) the torques generated by the thermal engine and the electric motor and the torque transmitted by the clutch, c) the values of these torques delivered to the wheels.
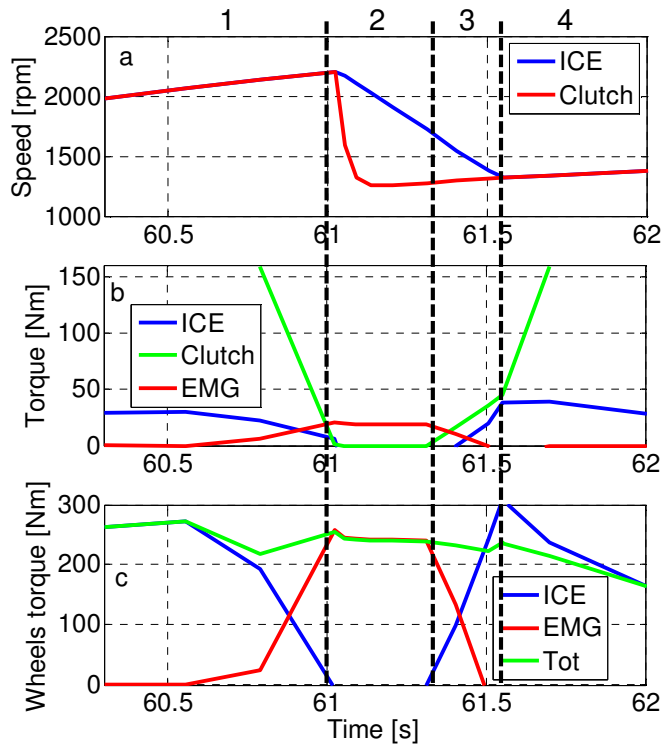
Figure 3.14 – Gear shift first-second: a) ICE and Clutch speeds, b) torques, c) torques to the wheels.

The gear shift manoeuvre can be divided in the following four phases [59]:

- Phase 1 (60.3 – 61 s): the torque generated by the ICE, which is around 35 Nm before the gear shift (more than 250 Nm to the wheels), is reduced up to null torque and the clutch is opened, to allow the gear change from first to second. During this phase, the EMG starts generating torque to compensate the discontinuity of the engine torque delivered. Therefore, the total torque delivered at the wheel remain quite constant at 250 Nm (see the green line on plot c of Figure 3.14).
- Phase 2 (61 – 61.3 s): when the clutch is opened, the EMG completely provides the torque at the wheels. The EMG generates 30 Nm in order to guarantee about 250 Nm to the wheels.
- Phase 3 (61.3 – 61.55 s): the second gear has been engaged and the clutch begins closing. The ICE increases the torque to the target. During this phase, while the clutch is slipping, the torque delivered

is the one transmitted by the clutch plus the one generated by the EMG. Both are controlled in order to keep near constant the torque at wheels.

- Phase 4 (61.55 – 62 s): the engine speed is now synchronized with the clutch speed. Then the torque transmitted is the one generated by the thermal engine, whereas the electrical motor is switched off. [59].

The PerfET architecture has also the advantage of increasing the fuel economy outside the gear shift options. Indeed, depending on the current driving status, the fuel consumption can be reduced through an intelligent use of the electric motor generator with respect to the following parameters.

Table 3.5 – P3 EMG technical data and strategies.

Hybrid Configuration	Voltage [V]	Peak Power [kW]	Max Torque [Nm]	Strategies	
				A	B
PerfET (P3)	48	22	60	**ICE**: works during entire cycle; **EMG**: activated if SOC>0.40 & Vehicle speed<40km/h **SOC**: almost constant	**ICE**: activated in high load conditions; **EMG**: always activated (motor: urban, generator: extra-urban); **SOC**: decreases in the urban phases, increases in extra-urban phases.

Two different strategies, namely A and B, are implemented to maximize the potential of the P3 hybridization: SOC, vehicle speed and engine efficiency. The strategies follow a heuristic logics that define in a flexible way the priorities on the delivery of the torque between the ICE and EMG. The strategy A manages the ICE and the EMG, according to the following control:

- ICE priority: EMG is used to fill the Torque Gap during the gear shift and it is a support to the ICE for high torque requested by the driver;

- EMG priority: ICE is a support to the EMG in 'over-demand' of torque. EMG is enabled if the State of Charge of the battery is above a SOC threshold of 0.40, the vehicle speed is lower than 40 km/h and the ICE operating conditions are very inefficient.

The control A ensures the ICE works during the entire drive cycle, as shown by the blue line of the graph *c* of the Figure 3.15. The SOC approximatively maintains the initial value during the whole NEDC (see Figure 3.15b). It is worth noticing that along the most of extra-urban phases the SOC remains constant. Indeed, during such operations the EMG is not connected to the driveline thanks to its clutch. Therefore, neither limit torque nor electrical current are generated. Moreover, when the clutch is opened the electric motor is not dragged, reducing mechanical and ventilation losses.

The strategy B enables the ICE at high load (i.e. in extra-urban phase of the NEDC), while the EMG is always activated (see red line in the graph c of the Figure 3.15). However, during the ECE, the EMG works as a motor, while at the EUDC the ICE powers the vehicle and ensures the charge of the battery, thanks to the generator mode of the EMG (an extra-load is demanded to the engine that provides a part of the power to the EMG, in order to charge the battery). The red line in Figure 3.15b shows the state of charge of the battery for the B strategy. As a result of the management strategy actuated, the battery SOC significantly decreases in the urban phase, to recover the initial value at the end of the transient. Some engine working conditions of a few seconds of time occurs during the ECE to recharge the battery due to the crossing of the SOC threshold of 40 %. The drawback of this strategy could be the late activation of the ICE during the EUDC, which imply a delay in the light-off of the catalyst; maybe resulting in violation of the pollutant emissions limits.
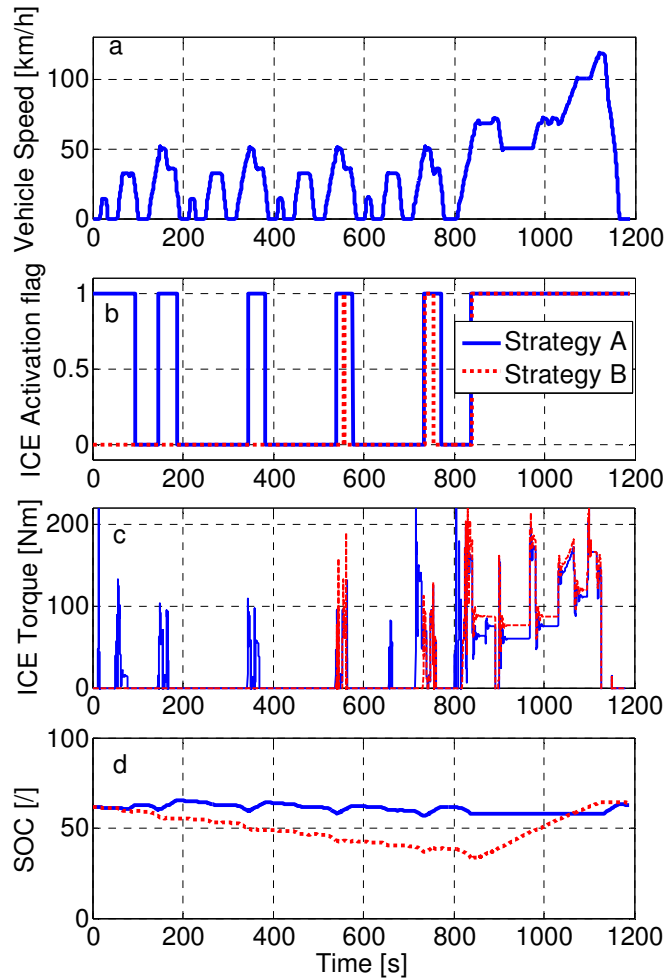
Figure 3.15 - Results P3 hybrid simulations along the NEDC: a) vehicle speed; b) ICE activation flag; c) ICE Torque; d) Battery SOC.

Figure 3.16 summarizes the results of the simulations of the P3 hybrid vehicle for the two management strategies, both in standard and more efficient conditions of the engine (TIs). It is seen a comparable reduction of CO_2 for both strategies. The strategy A contributes for about the 13.7 % to the saving of the CO_2, against the 14.5 % of the B one. By integrating this technology into the vehicle with TIs, the simulated maximum gain could reach about 24 %, with an improvement of 6.6 % related to the P3 hybridization.
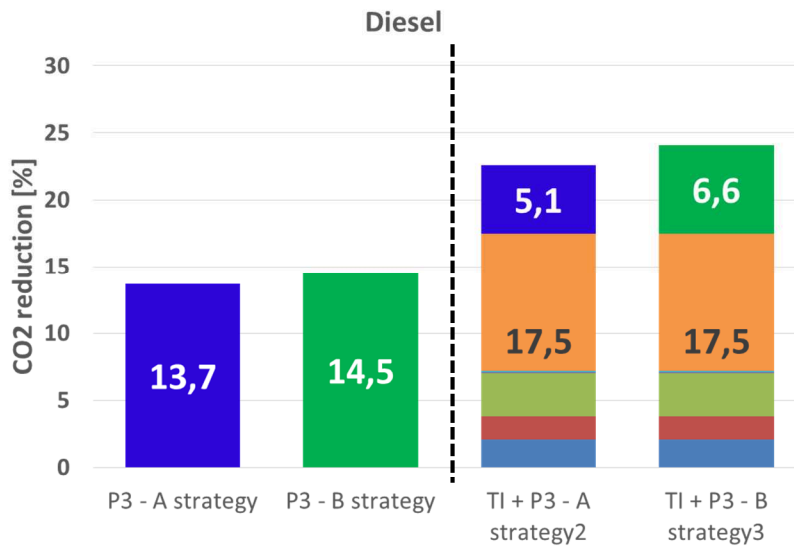
Figure 3.16 - Summary of the CO₂ saving potentials obtained along the NEDC by the implementation of the P3 EMG in the vehicle.

3.2.4. Fuel Cell hybrid vehicle

The fuel cell technology offers a combination of benefits, among these the most important are the high performance, wide applicability range, modularity and practically zero pollutant emissions. However, this technology has to reach specific technical requirement to become commercially competitive. Several fuel cell typologies exist, differing for their working principles, their electrolyte and possible applications. Within ground transportation, comparing available options in terms of power density, efficiency and working conditions, Polymer Electrolyte Membrane or Proton Exchange Membrane Fuel Cells (PEMFCs) seem to be the most suitable device [60].

The US Departement of Energy (DOE) has set clear specifications of the technical targets to be achieved by PEMFC systems for automotive uses (i.e. it have to reach at least a lifetime of 6000 h). According to the DOE [61], the cost of an 80 kW_{net} automotive PEMFC system based on 2012 technology and operating on direct hydrogen is projected to be \$47/kW when manufactured at a volume of 500000 units/year. However, the use of PEMFC systems for automotive applications still presents many critical

issues and drawbacks related to system technology, design, on-board fuel storage, fuel production and control.

Fuel cell stack

Fuel cells are electrochemical devices converting chemical energy into electrical energy via direct reaction between hydrogen and oxygen, without involving any heat conversion. Therefore, fuel cells are typically more efficient than thermal engines [62], which are limited by the Carnot principle and have not moving mechanical parts [8]. Moreover, since fuel cells are assembled in stacks, made of many unit cells, they can be used, without a remarkable variation of efficiency, for either high or low power applications. Polymer electrolyte membrane fuel cells have a polymeric membrane as electrolyte. They are particularly suitable for automotive applications thanks to high overall efficiency, their fast startup (0.1 s), low working temperature (60–90°C) and acceptable power density (250 W/kg) (ICEs have power density of about 500 – 800 W/kg) [10]. Figure 3.17 describes the basic working principle of a PEM-FC. A single cell consists of three components: anode, cathode, and polymeric electrolyte membrane separating the two electrodes. Oxygen and hydrogen (i.e., the reactants) are supplied to cathode and anode, respectively. The presence of a catalyst on the electrolyte surface promotes hydrogen ionization (see equation (3.2)), which releases protons H^+ and electrons. The hydrogen ions are able to pass through the polymeric membrane towards the cathode but the electrolyte does not allow the flux of electrons. Thus, the electrons are forced to flow through an external circuit, providing useful electric power, to the cathode, where they react with oxygen and hydrogen ions H^+ (see equation (3.3)).

This electrochemical reaction releases water either in liquid or vapour phase, depending on temperature and pressure. Summarising, at the anode, the hydrogen is oxidized, according to the reaction

$$2H_2 \rightarrow 4H^+ + 4e^- \tag{3.2}$$

while at the cathode, oxygen is reduced

$$O_2 + 4H^+ + 4e^- \rightarrow 2H_2O \tag{3.3}$$

The global reaction is therefore

$$2H_2 + O_2 \rightarrow 2H_2O + electricity \ + \ heat \tag{3.4}$$
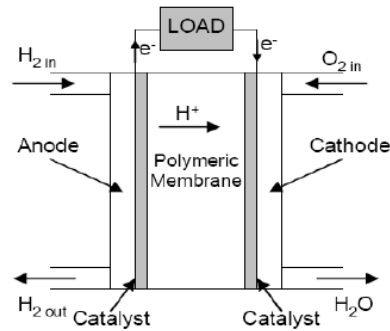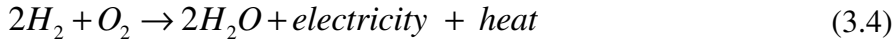
Figure 3.17 - PEM fuel cell working principle scheme [63].

A single fuel cell produces the power, which results from the area times the current density of the cell times the cell voltage. It is therefore common practice to put a number of cells in series, resulting in a so-called fuel cell stacks. The stacks power and voltage are obtained as the sum of the individual cells power and voltage.

Fuel cell performance characteristics are reported as voltage-current (*V-I*) profiles. Then, the overall stack voltage is evaluated by multiplying the single cell voltage by the number of cells, whereas the overall stack current is the same of the single cell. Consequently, the overall stack power is

$$P_{stack} = n_{FC}V_{FC}I = n_{FC}P_{FC} \tag{3.5}$$

The voltage, evaluated accounting for the main causes of losses occurring in a fuel cell, is expressed as

$$V_{cell} = E - V_{act} - V_{Ohm} - V_{conc} - V_{off} \tag{3.6}$$

where E is the electromotive force, also known as Nernst potential, while V_{act}, V_{Ohm}, and V_{conc} are the activation, Ohmic, and concentration losses, respectively. V_{off} is a constant voltage drop that accounts for minor losses such as contact resistance, internal current, and leaks [63]. Figure 3.19 (left side) reports the voltage versus the current, for the cell of the stack used for the purpose of the analysis reported afterwards.

A normalized efficiency map was inferred by fitting the experimental data

acquired on a PEM FC [64].

Balance of Plant (BoP)

To make the FC working properly the gases must be fed to both anode and cathode. Thus, at the cathode side, a compression device is required to provide air at the desired pressure. At the anode, the hydrogen stored in a high-pressure tank is delivered at low pressure to the inlet manifold by means of regulating valves [63].

Other components are required to guarantee the optimal performance of the stack. The Figure 3.18 gives a schematic, simplified diagram of a typical fuel cell system. The components other than the fuel cell stack and the fuel processor are often called Balance of Plant (BoP) components. Different auxiliary systems such as water pumps, humidification chambers and a compression device, in some cases, coupled with a turbine are also included into the BoP.
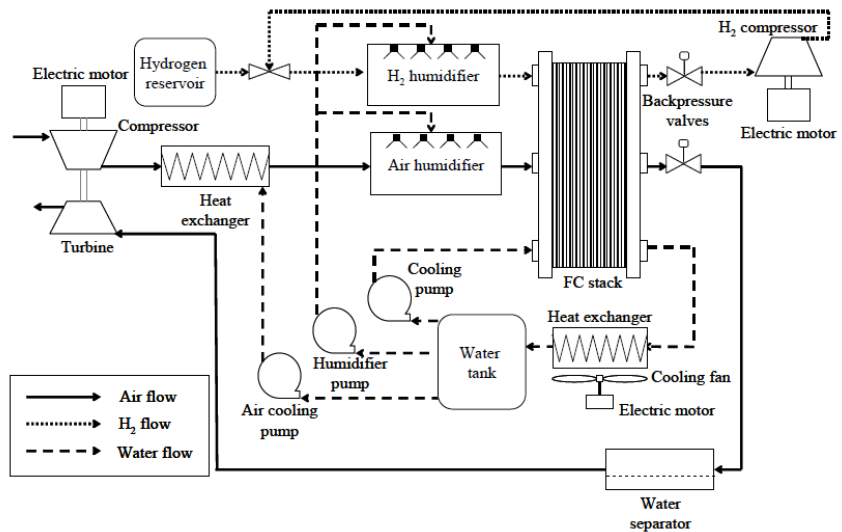
Figure 3.18 - Fuel cell system scheme [65].

The presence of a BoP leads to a reduction of overall efficiency due to the energy used to feed those devices. Particularly, the efficiency accounts for the net power generated as follows [64]

$$\eta_{FCS} = \frac{P_{stackt} - P_{aux}}{\dot{m}_{H_2} HHV_{H_2}}$$

(3.7)

Figure 3.19 (right side) exhibits the comparison between experimental and modeled efficiency values. The values of efficiency map of Figure 3.19 are hereinafter used to evaluate the amount of H_2 consumed by FCHVs by means of equation (3.7).
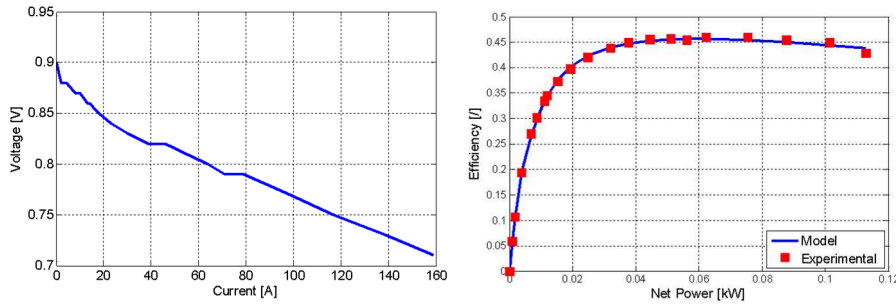
Figure 3.19 - Polarization curve (left side) and efficiency map (right side) of the PEMFC [64].

Fuel Cell Hybrid Vehicle

Before detailing the analysis performed to identify the fuel cell (FC) configurations, it is worth to mention that this part of the study is not intended to deepen the potential use of FC within dedicated vehicles. Indeed these vehicles, such as those being of their market enter stage, could not be compared with conventional ones, except for the final purpose in terms of CO_2 emissions and toxic gases released. The implement of that technology entails the use of completely different devices which could not be compared with ICE based or electrical based vehicles. The purpose of the following analysis is rather oriented towards the study of a technology that could be considered for a transition phase. Therefore, some solutions (i.e. battery sizing and performance) might appear not consistent with standard case.

The fuel cell sub-model has been integrated into the conventional vehicle model, as presented in Figure 3.20. The reference vehicle used for this analysis is the Alfa Romeo Giulietta equipped with the 1.4 l MultiAir Turbocharged SI engine.
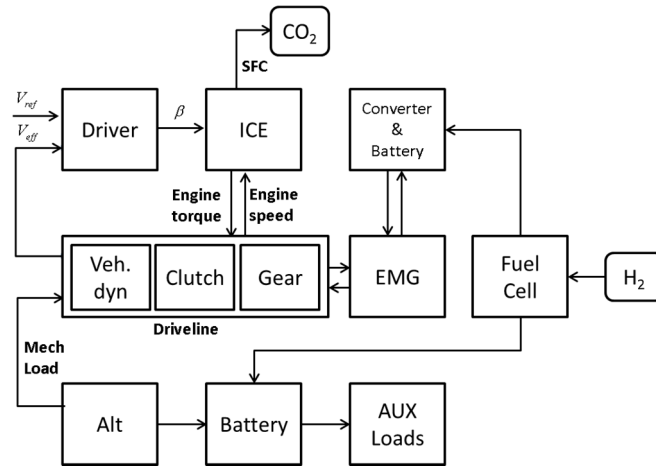
Figure 3.20 - Scheme of the engine model equipped with the FC system, including additional converter and battery devices.

Two configurations of hybrid fuel cell vehicle have been implemented to understand the potentialities of this technology. One case considers a parallel hybrid, the P3 hybrid layout with a fuel cell system to feed the electric motor generator (see Figure 3.21). The second case is a series hybrid architecture (see Figure 3.22), that has a major utilization for fuel cell applications.
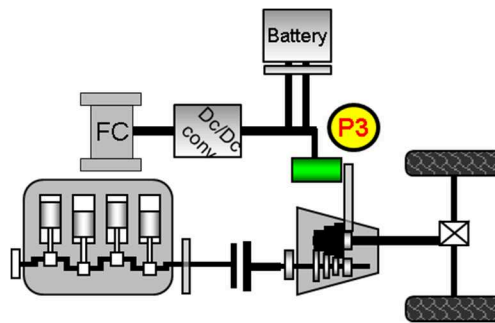
Figure 3.21 - Parallel Fuel Cell Hybrid vehicle configurations.
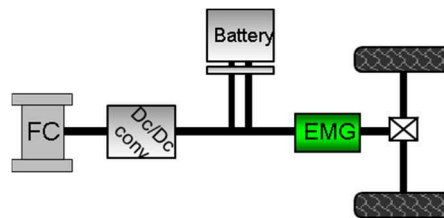
Figure 3.22 - Series Fuel Cell Hybrid vehicle configurations (Range Extender).

Parallel hybrid fuel cell vehicle takes into account both A and B strategies used for P3 management, above described, with different required power, whereas the series hybrid represents the fuel cell range extender.

Referring to the parallel FCHV architecture, the vehicle mass can be obtained by adding the mass of hybridizing devices (battery, stack, electric motor generator, hydrogen tank, converter) to the conventional vehicle body mass. The mass of the range extender vehicle, instead, is derived by subtracting the contributions due to the original gearbox and ICE from the original conventional mass and by replacing them with the hybridization devices [64]. For both parallel and series configuration, the energy provided by the fuel cell is stored in battery. The battery provides the needed power to drive the EMG or stores energy from the EMG during the regenerative phases, based on the control demands.

The benefits achievable by the FCHV are strongly dependent on the control of the FC, the EMG and the ICE. The requested power at wheels is managed from the control unit, which defines the power split between the thermal engine and the EMG, for the parallel case. On the other hand, the series FCHV control guarantees that the EMG fulfils the requested power to the wheels.

The sizing of the fuel cell stack is based on the needed power to the EMG to drive the vehicle along the cycle and to maintain the same SOC level of the battery between the start and the end of the cycle. The fuel cell produces a constant power along the entire driving cycle, in maximum efficient working conditions. For the analysis of the system efficiency it is needed to take also into account the presence of a DC/DC converter. The converter aims at regulating the direct current from voltage level of the output FC to the voltage of the battery. It is worth remarking that an analysis has been carried out to evaluate the benefits coming from two different solutions: the use of the fuel cell in a lower efficiency working condition, by eliminating the converter, and the coupling of the FC at maximum level of efficiency (0.457) and the converter with efficiency of 0.9. The better solution for this application resulted in the combined use of the two devices: the FC works in optimal efficiency condition with variable output voltage, based on the requested power, and the DC/DC converter regulates the voltage to the battery value. The two alternatives have been analysed with respect to the main design and operational variables. The factors that have mainly affected the choice have been the number of cells and the working condition of the fuel cell, as well as the global efficiency of the

system. A large number of cells involves a useless stack oversizing, with low power density. Moreover, it needs to work in the linear zone of the polarization curve, by avoiding high diffusion losses, but at high current to increase the power. Moreover, the control keeps the stack in the region between maximum efficiency and maximum power. Thus, according to the maximum efficiency criterion, known the power demanded by the driver, it is easy to evaluate the number of cells, the current and the voltage of the entire stack, through the equations (3.7).

Table 3.6 – Characteristics of the fuel cell stack for the parallel hybrid vehicles and the range extender case.

	Power stack [W]	**Number of cells [/]**	**Stack voltage [V]**	**Current stack [A]**
P3 FCHV A-strategy	900	15	11.85	75.96
P3 FCHV B-strategy	1350	22	17.39	77.68
Range-Extender	3400	55	43.45	78.25

Table 3.6 indicates the values of power, numbers of cells, voltage and current for the parallel hybrid vehicles and the range extender case.

In this section, the results of the simulations performed for the FCHV along the NEDC are presented. A comprehensive analysis has been carried out to evaluate the real benefits given by the adoption of the fuel cell technology in light duty vehicle. The performed simulations provide the amount of both gasoline and hydrogen consumptions. The results have been also extended to a well to wheel CO_2 emissions analysis. First a Tank-to-Wheel analysis has been carried out to evaluate the consumption of both fuel and H_2, then a Well-To-Tank study has been performed. The conversion process of the H_2 mass into CO_2 equivalent emissions is described in the following equations

$$m_{H_2 2gasoline,eq} = m_{H_2} \frac{HHV_{H_2}}{LHV_{gasoline}} \tag{3.8}$$

$$m_{gasoline,eq} = m_{gasoline} + m_{H_2 2gasoline,eq} \tag{3.9}$$

where *HHV* and *LHV* are the higher heating value and lower heating value, respectively.

Table 3.7 - Techniques to produce the H_2 and the Global Warming Potential (GWP) for each system [66].

H_2 Production System	GWP [$g_{CO2,eq}/g_{H2}$]
Steam reforming	12.52
Steam reforming + Carbon Capture & Storage	5.23
Wood Gasification	2.11
Grid Electrolysis	27.14
Wind Electrolysis + Grid	1.56

It is worth pointing out that the fuel cells are considered zero emissions devices, nevertheless the production and distribution of the hydrogen require energy and lead to the generation of CO_2 if fossil fuels are reformed to generate H_2 or other sources due to compression, transport, storage, etc. The environmental impact of each technology is expressed as $g_{CO2,eq}/MJ_{fuel}$, then converted in g_{CO2}/g_{H2} by accounting also for the influence of other gases in the air [117]. In order to evaluate the best advantages achievable, a 700 bar compressed hydrogen produced by means of the wind electrolysis has been taken into account among all systems. According to JRC [117], the consumption of carbon dioxide per kg of Hydrogen is the 1.56 kg. On the other hand, the production and the distribution of the gasoline produce 0,60 $g_{CO2}/g_{gasoline}$. Table 3.6 lists the most important techniques to produce the H_2 and the Global Warming Potential (GWP) for each system [66].
The histogram on the left side of Figure 3.23 shows the results of the Tank to wheels (TTW) analysis of the simulations for the different FCHV configurations along the NEDC. The CO_2 reductions have been computed with respect to the conventional case (Baseline). The CO_2 emission from the thermal engine is represented with light colours, whereas the dark-coloured bars refer to the Hydrogen consumption and correspond to the CO_2 equivalent emissions computed by the equation (3.8). Obviously, the conventional case does not consider the Hydrogen consumption and, on the other hand, for the range extender mode the gasoline consumption is null.

By increasing the use of the fuel cell towards the range extender mode, the use of the thermal engine decreases, with improvement in gasoline saving. For the TTW analysis, a reduction of the thermal engine exploiting, leads to a decreasing trend of the gasoline CO_2 emissions and an increase of the H_2 consumption.

The WTT analyses (see the histogram on the right side of the Figure 3.23) provides the amount of emitted CO_2 during the processes of production of fuels. The Global Warming Potential (GWP) allows the computation of the CO_2 emissions, this based on the consumptions of both gasoline and hydrogen of the vehicle along the NEDC of the TTW analysis. The WTT analysis follows the TTW trend of the CO_2 emissions, but, clearly, with lower values. From the baseline configuration to range extender, the CO_2 emissions for the production of gasoline decrease. The opposite trend occurs for the CO_2 emissions during production of hydrogen.

The WTW analyses is reported in Figure 3.24. To obtain the WTW results, the CO_2 emissions of the TTW analysis are added to the WTT one. The WTW analysis reproduce the TTW trend, but the CO_2 reductions are lower for each FCHV configuration. The entire process Well-to-wheels involves a lower saving of CO_2 emitted, reducing the values from 28.3, 42.2 and 100 % to 27.9, 40.4 and 95.4 % against the conventional case, for the Hybrid with the strategy A, strategy B and range extender configurations, respectively.

The results shown remark that the implementation of the fuel cell systems into light duty vehicle may provide the higher benefits. Although the fuel cell market in automotive industry is expected to grow with important investments in the next decades, the PEMFC systems for automotive applications still presents some problems for a wide industrial production and commercialization.
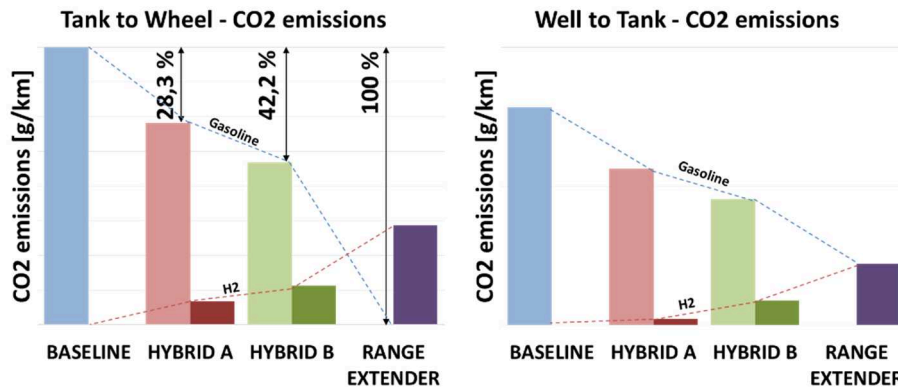
Figure 3.23 – Tank to wheel CO₂ emissions results along the NEDC (left side) and Well to Tank CO₂ emissions results along the NEDC (right side).
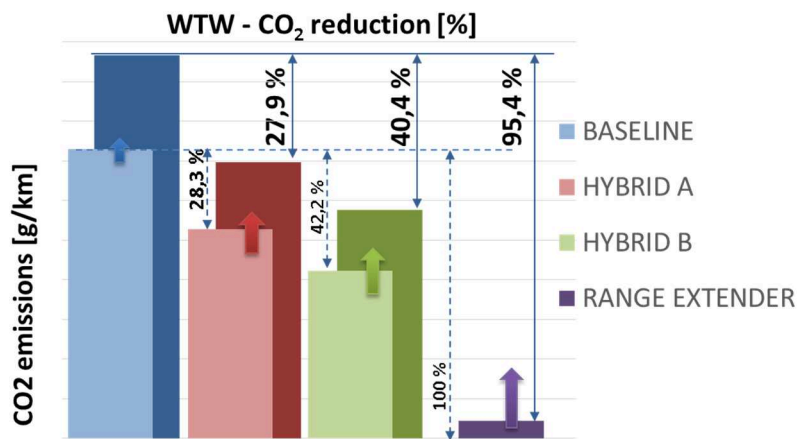
Figure 3.24 - Well to wheel CO₂ emissions results along the NEDC.

3.3 Conclusions

Several technologies for the improvement of the engine efficiency have been described and analysed, in order to investigate their CO_2 impact along the NEDC. Important results in terms of enhancement of the engine efficiency can be obtained. Among others, the engine downsizing and the cylinder deactivation are the most remarkable; they may provide fuel savings up to 10-15 % for light duty vehicles. The sum of the several

technological improvements allows achieving excellent results leading to 26 % and 17.5 % for vehicles equipped with SI and CI engines, respectively. Thus, such advanced technologies can guarantee the key role of the internal combustion engines in automotive market for the next decades.

Table 3.8 – Hybrid powertrain characteristics configurations and strategies used.

Hybrid Configuration	Voltage [V]	Peak Power [kW]	Max Torque [Nm]	Strategies		
BSG (P1)	48	13	60	A Alt.	B Alt.+ Reg.brak.	C Alt.+Reg.brak.+ Traction (40km/h)
ISG (P2)	48	22	60	Reg.brak.+ Traction		
				Speed Limitation: **20** km/h	Speed Limitation: **40** km/h	Speed Limitation: **60** km/h
PerfET (P3)	48	22	60	A		B
				ICE: works during entire cycle; **EMG**: activated if: SOC>0.40 & Vehicle speed<40km/h; **SOC**: almost constant during the cycle.		**ICE**: activated in high load conditions; **EMG**: always activated (motor: urban, generator: extra-urban); **SOC**: decreases in the urban phases, increases in extra-urban phases.

An analysis of the energy consumption and CO_2 reduction for several hybrid powertrain configurations are also reported below. Figure 3.25 summarizes the advantages of the hybridization of vehicles comparing three configurations namely P1, P2 and P3. In order to compare the CO_2 reduction, the benefits related to the P2 are considered with the limitation on the boost contribution of 40 km/h, as used for the P1, while the P3 configuration adopts the strategy B that allows achieving the highest results. In Table 3.8 are reported the hybrid powertrain characteristics configurations and the strategies used. The installation of the electric

machine into the conventional layout of the vehicle can bring an important contribution to reduce the CO_2 emissions up to 15.3 % for the P2 configuration. If the engine is already optimized with the technological improvements, the emissions tends to decrease again. In the histogram of Figure 3.25, it is shown that the maximum achievable reduction of carbon dioxide emissions is equal to 28 % for the TIs + P2 hybrid system.
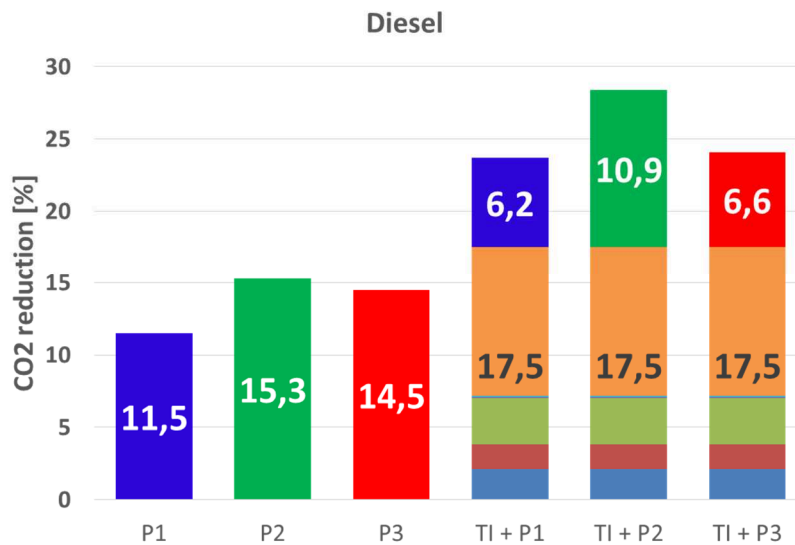
Figure 3.25 - Summary of the CO_2 saving potentials obtained along the NEDC for different kind of hybridization of the vehicle.

The P2 configuration allows minimizing both drag and pumping losses through the disconnection of the thermal engine from the powertrain during pure electric travel and regeneration operations. However, the other configurations give an important fuel saving and some other advantages, such as the easy implementation of Stop & Start function for P1 and to improve the comfort and drivability with the Torque gap filling thanks to P3. Due to their significant potential in reducing fuel consumption and emissions, hybrid electric vehicles are currently considered the most viable alternative propulsion system and are now actively under development by many car companies.

A further analysis has been carried out, showing the important benefits of a fuel cell vehicle. An Well-to-wheel analysis has been performed and the simulations along the NEDC provide excellent results for FC Range Extender vehicle, that could reach up to 95 % of CO_2 reduction. However,

the use of the FC for automotive applications still presents some critical issues. Some drawbacks are subject of current research and will be surely overcame in the next decade. Several disadvantages are related to system technology, design, on-board fuel storage, fuel production and control.

CHAPTER 4

Waste Heat Recovery systems (WHRs)

In the last years, several authors [68][8] have shown the great potential of the Waste Heat Recovery (WHR) to improve ICE thermal efficiency by recovering and converting the wasted heat from the exhaust and coolant fluids into a more useful form of energy. It is worth noticing that the recovery from the exhaust is more efficient, due to the higher temperature, than the liquid coolant, in spite of the latter greater heat capacity and thermal conductivity [5]. Over the years, several types of WHR systems for transportation applications have been investigated and developed. Among the most promising energy recovery technologies explored, the electric turbo-compound (ETC or E-Turbo), Thermoelectric Generators (TEGs) and Organic Rankine Cycle (ORC) are the most effective. Legros et al. [68] conclude that these waste heat recovery technologies could be effectively helpful in reducing CO_2 emissions as confirmed by different authors [6][7].

In this Chapter, an overview of these 'eco-innovation' technologies is carried out, by starting from the state of art and ending with the modeling and the simulations of the ETC, TEG and ORC applied to the conventional vehicle. The WHRs overview ends with a summary of the results for all technologies explored. As mentioned in Chapter 2, the study of the WHR technologies refers to a segment C vehicle (Alfa Romeo Giulietta) equipped with a 1.4l turbocharged spark ignition engine with variable valve actuation (VVA) system; for the main technical data the reader is addressed to Table 2.1. It is worth remarking that the fuel economy and CO_2 emissions evaluated on the NEDC of this vehicle are equal to 16.20 km/l and 144 g/km, respectively.

In order to carry out the analysis, an additional battery and an inverter were added to the standard layout. A lithium battery pack with overall capacity of 200 Wh and nominal voltage of 48 V was considered for the current analysis [24]. The Figure 4.1 shows the scheme of the vehicle-powertrain model, integrated with a Waste Heat Recovery system.
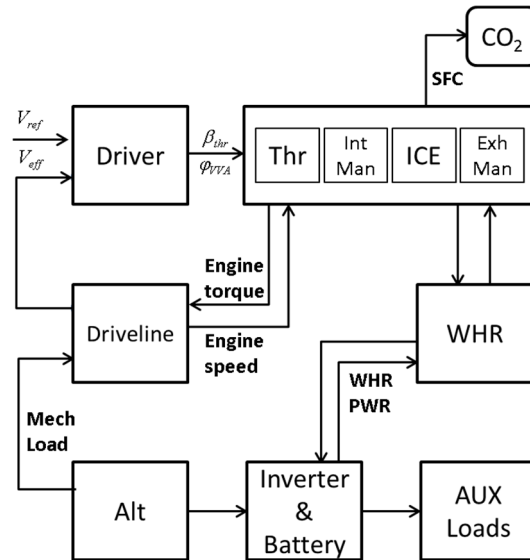
Figure 4.1 - Scheme of the vehicle powertrain model.

4.1 Electric Turbo Compound (ETC)

The ETC consists of an electric machine, hereafter addressed as Motor-Generator Unit (MGU), integrated into the turbo shaft that can operate either as generator or as motor (see Figure 4.2) [24]. In generator mode, the recovered power can satisfy the vehicle electrical demand to drive the auxiliaries or can be stored in the batteries. In motor mode, the MGU allows improving the engine transient response at low speed or during engine warm-up, when the exhaust enthalpy is low and the turbine-compressor power cannot sufficient to boost the engine. This feature promotes the engine downsizing that is one of the most effective ways to obtain an improvement of fuel economy while maintaining the original vehicle performance. Such an aspect was investigated, among the others, by Mamat et al. [69] who evidenced that a 1.0 L turbocharged gasoline engine may offer the same performance as a 2.0 L, with a possible CO_2 reduction of about 40%.
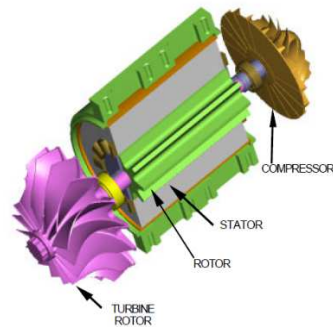
Figure 4.2 - Caterpillar Electric Turbo-Compound System scheme [1].

Other potential benefits of ETC are in a better turbine-compressor matching and the possible removal of waste-gate valve and variable geometry device. Electric turbocharger assistance is therefore a key technology for the reduction of fuel consumption and CO_2 emissions [71]. The technical problems in selecting the appropriate electric machine to be used for an electrically assisted turbocharger are dealt by Bumby et al. [72]. Furthermore, they propose a different configuration of turbo-compound by installing an additional turbine placed downstream of the turbocharger. In such a configuration only the turbine is coupled with an electric machine acting as generator only.

4.1.1. ETC - State of art

Many OEMs, especially in the heavy-duty engine field [1][73], had already applied turbo compound, but greatly oriented to the possibility of having extra-mechanical power [74]. In [1], a Caterpillar application on heavy-duty vehicles shows that a reduction of fuel consumption between 5 and 10% can be reached along highway travelling at a constant speed of 1500 rpm and variable load between 25 and 50%. The simulations carried out by Ibaraki et al. [75], who called the ETC 'hybrid turbo', evidence encouraging results: 10% improvement of fuel efficiency and 50% improvement of engine torque in the low-engine speed zone, in addition to 70% reduction of turbo lag during acceleration. These results are achieved by a suitable control of the 'hybrid turbo': when operating at low engine speed, the hybrid turbo enhances better combustion, lower emissions and improved torque response thanks to motor assistance. At high engine speed, higher engine efficiency is achieved by regenerating the extra power of the

exhaust gas into electric power to drive the auxiliaries. Lefebvre et al. [76] propose an electrical booster (i.e. supercharger) placed upstream of the main compressor, with the aim of speeding up the time response during transient and improving the main compressor efficiency. The same results were achieved by Pallotti et al. [77] for a small, four-cylinder S.I. engine equipped with an e-boosting system, which enhances engine downsizing maintaining similar performance and low fuel consumption (-12%). Fuel economy benefits in both Diesel and SI engines for SUV and light truck applications are achieved also in the work proposed by Balis et al. [73].

Only recently, the possibility to recover the energy by the electric turbo assistance, has gained increased interest in literature. Such an interest is even due to increasing demand for electrical equipments and the growth of hybrid powertrain. Early studies of the ETC were developed for both Diesel [78][38] and gasoline engines [25][76], with an average reduction of CO_2 by about 5 %. The exhaust energy recovery can be achieved by taking into account several configurations of electric turbo-compound, as reported in a comparative study on different types of ETC systems carried out by Mamat et al. [69] and by Zhuge et al. [79]. For the objective of this thesis, the simplest architecture has been studied as shown into Figure 4.3

4.1.2. ETC Modeling

The scheme of the turbo-compound system is shown in Figure 4.3. This configuration involves a turbocharger assisted by the MGU to generate electrical power or to drive the compressor, depending on the adopted strategy. The energy recovered from the exhaust gases can be stored in a battery and/or used to power the auxiliary devices. The proper management of the MGU and recovered energy may lead to a significant improvement of fuel economy [24].
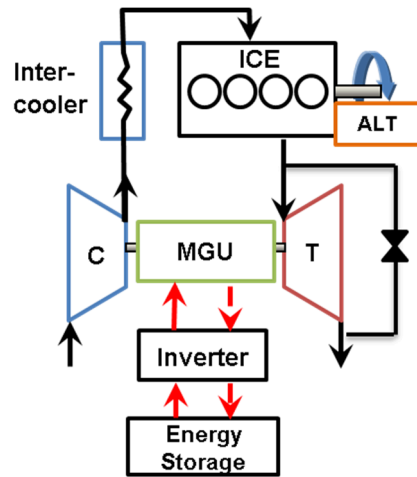
Figure 4.3 - Scheme of the engine equipped with the ETC system (Compressor, MGU, Turbine), including alternator, inverter and energy storage devices [24].

In order to take into account for the motor/generator power and for the mechanical connection between the turbocharger and the electrical machine, the equation (2.48) is modified and the term P_{MGU} is added, as follows

$$\frac{d\omega_{tc}}{dt} = \frac{P_t - P_c \pm P_{MGU}}{I_{tc}\omega_{tc}} \qquad (4.1)$$

where the + sign applies in case of the MGU works as a motor, whereas the – sign applies in the other mode.

The interaction between turbocharger and MGU is simulated through the power balance equation applied to the turbocharger shaft, as sketched in Figure 4.4.
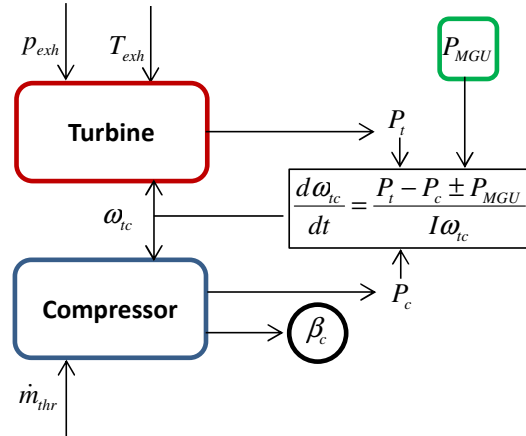
Figure 4.4 - Scheme of the ETC model [38].

4.1.3. ETC and Alternator Control

The benefits achievable by the ETC are strongly dependent on the management strategies applied to the MGU [24]. In previous studies [38][6] is evidenced that depending on the MGU operation mode (i.e. generator/motor) and the amount of power recovered or supplied, different targets may be achieved, leading to CO_2 reduction or improvement of vehicle performance. Particularly, an optimal MGU management may be applied to maximize the fuel economy depending on the power requested by engine/vehicle auxiliaries. In this paragraph, the management strategies considered for the ETC and alternator are described. As previously mentioned, for the current analysis only the MGU operation as generator is considered. The power recovered by the MGU is imposed to be proportional to the turbocharger speed as far as this latter is greater than a lower threshold, to avoid an excessive reduction of the speed, as reported in Figure 4.5.
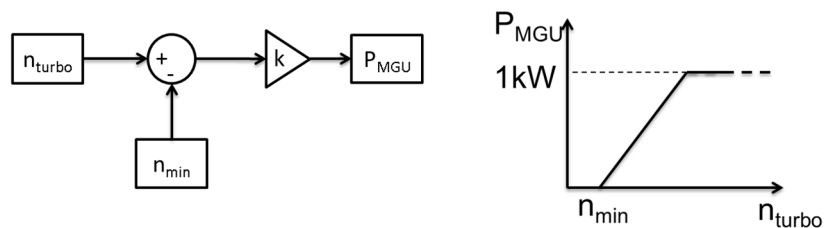
Figure 4.5 - MGU control scheme (left side) and MGU power limitation against the turbo speed (right side).

The recovered energy is stored into the battery pack and then used on demand to drive the electric auxiliaries, depending on the management strategy of the alternator. In fact, two different strategies, namely A and B, are introduced for the electric management of the alternator. The strategy A enables the alternator at low load engine operation (i.e. in the urban phase of the NEDC) while the alternator is electrically disconnected at high load, to avoid the auxiliary load on the engine shaft. On the other hand, the strategy B enables the alternator only at high load operation, as in the extra-urban phase of NEDC and WLTC. In both cases (i.e. strategies A and B) the constraint to recover the initial battery SOC at the end of the driving cycle was imposed. It is worth remarking that the maximum recovered power by the MGU is limited to 1 kW (see Figure 4.5), to avoid penalizing the engine performance. Indeed, an increase of the power recovered by the MGU would result in larger backpressure and lower engine efficiency [24].

In order to achieve the greatest benefits in terms of fuel economy, two control strategies are implemented depending on MGU and engine operating conditions. At low load operation and when the MGU is switched off, the baseline VVA map is employed, to preserve engine fuel consumption, and the throttle opening is driven by a PID controller based on the vehicle speed error. On the other hand, at high engine load, when the MGU operates in generation mode, the full throttle opening is imposed to minimize the pumping work and the closed loop control is applied to the VVA. Figure 4.6 shows the control strategies applied for the VVA depending on engine / MGU operating conditions. The VVA map shown on the left side was derived from experimental data measured at the engine test bench in steady state conditions.
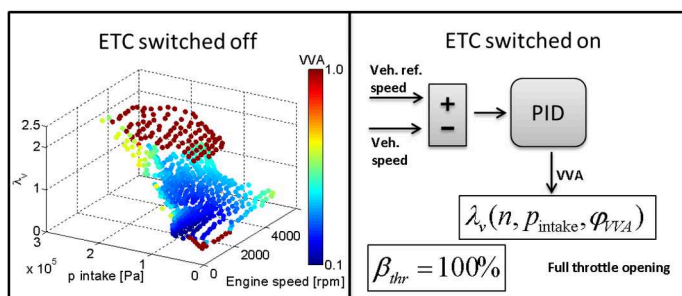
Figure 4.6 - VVA control strategies at low load (left side) and high load (right side).

4.1.4. ETC Results

The fuel economy and CO_2 reduction improvement of the ETC implementation is due to two factors: i) the amount of energy recovered by the ETC that allows recharging the battery thus relaxing the alternator load on the engine, coupled with ii) a more effective management of the alternator. The introduction of the ETC in the standard vehicle architecture, without implementing a suitable management of the alternator results in a CO_2 reduction of 2.9 % and 3.8 % for the NEDC and WLTC, respectively. In the Figure 4.7 are reported the trajectories of the exhaust gas temperature and mass flow rate along the NEDC as computed from the powertrain model. These data are the input for the submodel of the ETC.
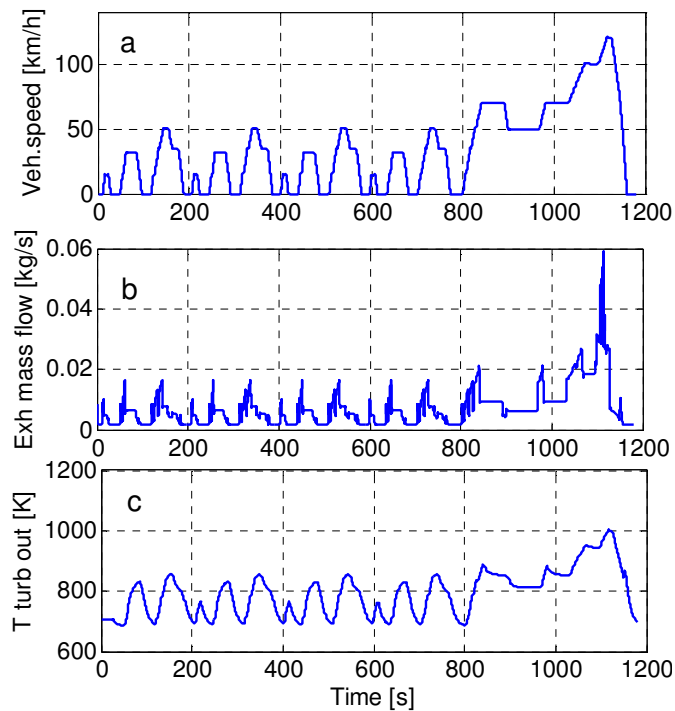
Figure 4.7 - Time histories of the simulated exhaust gas mass flow rate (above), exhaust gas temperature (below).

The upper plot of Figure 4.8 shows the time histories of compressor and turbine power and the power recovered by the MGU along the NEDC. The lower graph of Figure 4.8 reports the operation of the MGU and the alternator. Since the MGU is activated when the turbo speed is greater than

the lower threshold of 30000 rpm, the energy recovery takes place only when the engine operates at high load, as in the extra-urban transient (see red-dotted line in Figure 4.8b). In fact, as shown in Figure 4.8a, these operating conditions are the only ones where the turbine power is significantly higher than compressor and a significant amount of energy can be recovered by the MGU.

The results of the simulations performed by implementing the alternator management strategies A and B, are shown in the Figure 4.9 - Figure 4.12. The Figure 4.9b indicates the alternator and MGU operation along the NEDC when the strategy A is applied, evidencing that the alternator is activated only during the urban transient (see solid-blue line). The MGU operation (see the dotted-red line) is very similar to that related to the standard alternator management (see Figure 4.8b), thus leading to a similar time history of the recovered power. Furthermore, the simulated battery state of charge (SOC) shown in Figure 4.11, exhibits in case of the strategy A, similar trajectory than that achieved for the standard management, with a negligible variation with respect to initial and final values. The Figure 4.10 shows the simulation results achieved while implementing the strategy B. In this case, the alternator is enabled when the engine works at high load (i.e. extra-urban transient) and the MGU operates more frequently, especially in the urban cycle. This is actuated by the relaxing of the lower threshold of the turbo speed from 30000 rpm down to 20000 rpm. It is worth noting that such threshold was not feasible for the previous cases (i.e. standard and A strategies), due to the extra power requested by the alternator in the urban cycle that may inhibit the engine from providing the driving torque requested to accomplish the reference vehicle speed trajectory. As a result of the management strategy actuated, the battery SOC significantly decreases in the urban phase, to finally recover the initial value at the end of the transient (see Figure 4.11).

The strategies determine different torque profiles, due to different activation modes of the ETC and the alternator and to the VVA control strategy at both low and high loads. During the urban phase, the strategy A leads the engine to work at higher load due to the alternator utilization (red line in left graph of Figure 4.12). On the other hand, the alternator shutdown in the strategy B (green line in left graph of Figure 4.12) causes a reduction of the engine torque compared to the ETC mode without alternator management (blue line in left graph of Figure 4.12). Of course, the opposite considerations are worth for the extra-urban cycle, as shown in the right

graph of Figure 4.12.

The simulations performed along the WLTC with the strategy B, lead to similar results: an increase of fuel economy is achieved when the ETC powers the engine auxiliaries, as reported in Figure 4.13.

The overall results are summarized in Figure 4.14 that shows the reduction of CO_2 emissions achieved with the ETC implementation, for the different alternator management strategies investigated. It is worth noting that the WLTC exhibits the major reduction of CO_2, due to the higher load conditions, with an improvement of fuel economy over 5 % with the B strategy applied.
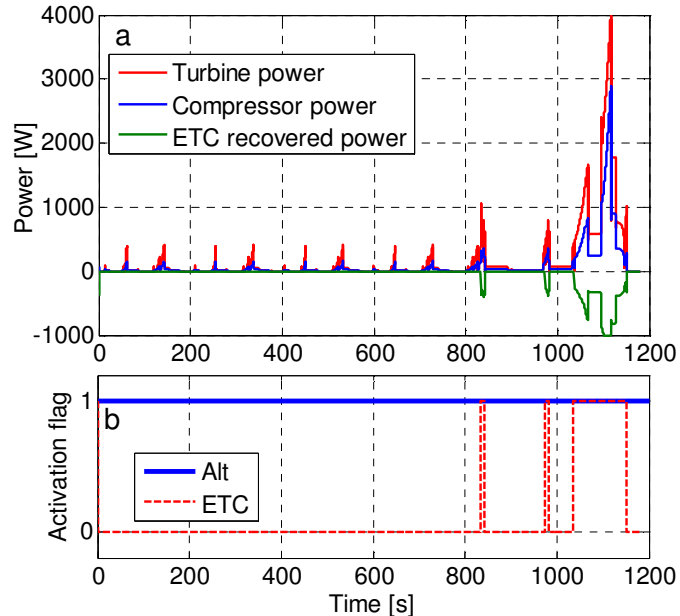
Figure 4.8 - Simulation results on the NEDC with standard alternator management: a) Turbine, compressor and MGU power; b) Alternator and MGU operation (1- on, 0 - off).
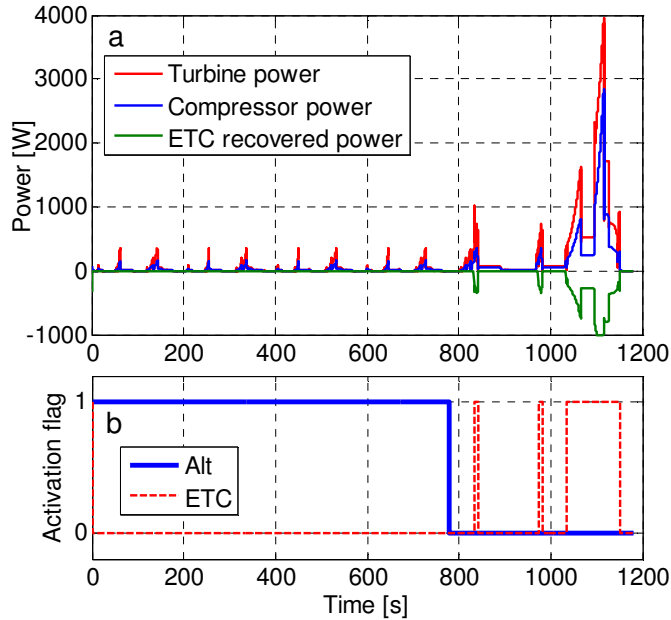
Figure 4.9 - Simulation results on the NEDC with strategy A: a) Turbine, compressor and MGU power; b) Alternator and MGU operation (1- on, 0 - off).
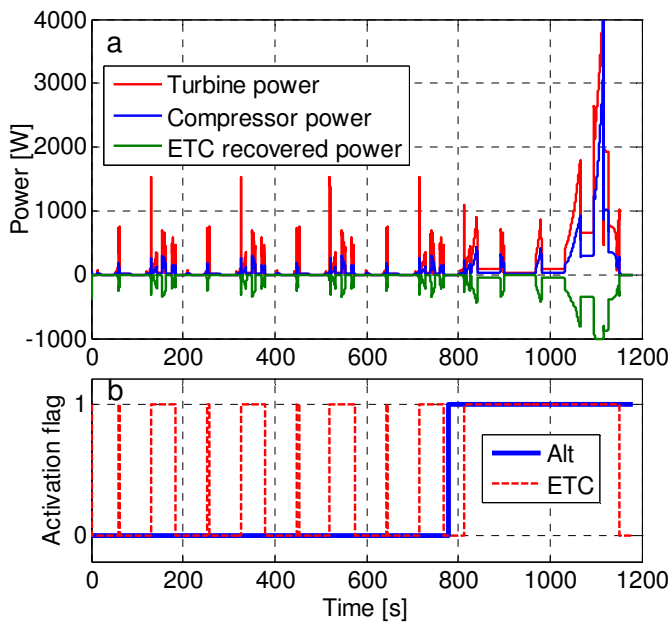
Figure 4.10 - Simulation results on the NEDC with strategy B: a) Turbine, compressor and MGU power; b) Alternator and MGU operation (1- on, 0 - off).
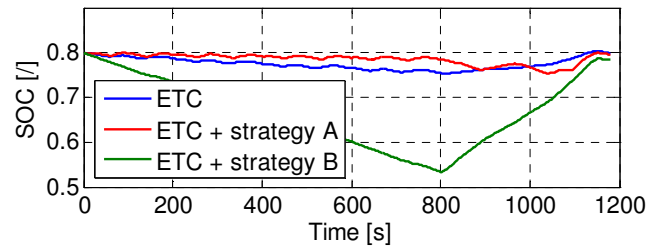
Figure 4.11 - Simulated trajectories of the battery SOC on the NEDC in case of standard alternator management, strategy A and strategy B.
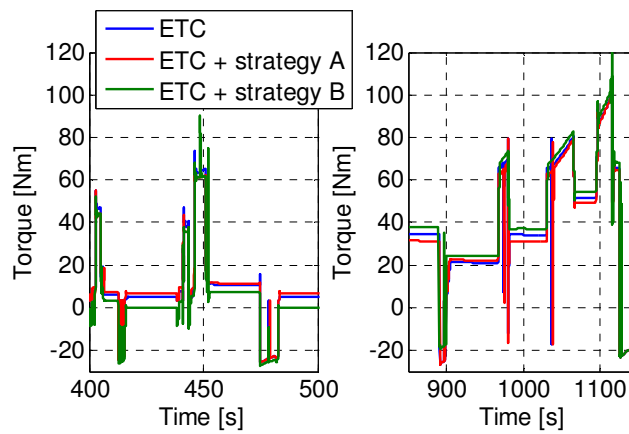
Figure 4.12 - Simulated trajectories of the engine torque on the NEDC. Left side: urban transient (time window 400 – 500 s); Right side: extra-urban transient (time window 850 – 1150 s).
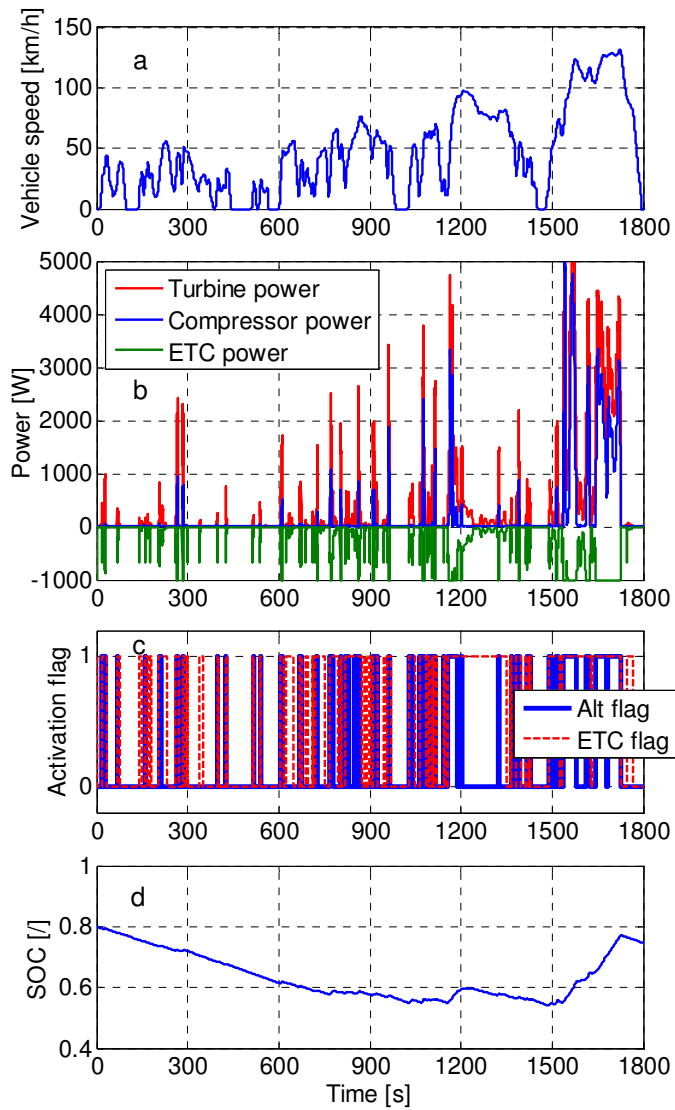
Figure 4.13 - Simulation results on the WLTC with strategy B: a) measured vehicle speed profile; b) Turbine, compressor and MGU power; c) Alternator and MGU operation (1- on, 0 - off); d) Battery SOC.
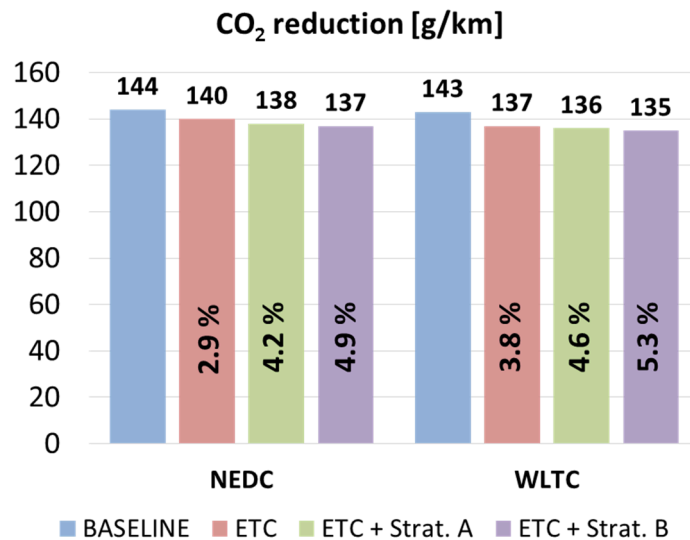
Figure 4.14 - Estimated overall CO₂ emissions along NEDC and WLTC, for the three management strategies investigated.

4.2 Thermo Electric Generators (TEGs)

Most thermoelectric materials have double potential applications. One is based on the Peltier effect and is focused on various applications of heating or cooling. Second exploits the Seebeck effect for power generation, primarily, from waste heat [80]. In the latter case, TEGs convert heat (temperature differences) directly into electrical energy and it can be used for automotive applications in waste heat recovery from the exhaust gas.

The Seebeck effect is a phenomenon that occurs between two different electrical conductors or semiconductors in presence of a temperature difference, resulting in a voltage difference (see Figure 4.15). When one of the two conductors or semiconductors is heated, a flux of electrons moves towards the cooler source; then, direct current (DC) is generated, if the pair is connected through an electrical circuit.
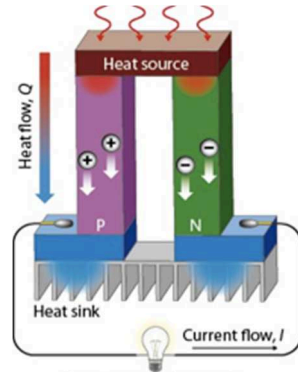
Figure 4.15 - Seebeck effect [80].

The Seebeck effect generates small voltage differences at the junction, about a few microvolts per kelvin of temperature difference; it may reach a few millivolts if the temperature difference is large enough. The connection in series of several devices allows to increase the output voltage, whereas the parallel layout increases the current. The configurations of large arrays of these devices can provide useful electrical power if a large temperature difference is maintained across the junctions. On the most widespread application is found in the thrermocouples, which exploit indeed the Seebeck effect [81][82]. However, due to the small power density of these systems, the power generated may not reach high values. The efficiency of the thermoelectric energy conversion is proportional to figure of merit of the materials, ZT

$$ZT = \frac{\sigma S^2 T}{k} \tag{4.2}$$

where σ is the electrical conductivity [1/Ωm], S the Seebeck coefficient, T the absolute mean temperature and k the thermal conductivity. For a long time, the best known thermoelectric materials were bismuth telluride-based alloys with a ZT around 1 [83]. Thermoelectric generators (TEGs) are characterized by very low efficiency (3-5%) with currently available materials. In principle, for a vehicle with 60 kW of exhaust wasted heat such low efficiency can guarantee the generation of the required electrical energy for on-board uses. However, materials with higher ZT and low costs may help in reducing the dimensions of the devices and enhance their installation on board of large automotive fleets [84][80][85].

4.2.1. TEG - State of art

In recent years, technological developments have increased the efficiency of thermoelectric, with further improvements expected. The dimensionless figure of merit, ZT, exhibits a value around 1 for common thermoelectric bulk materials; however recent developments in quantum-well and quantum-dot nanostructures have produced materials with ZT up 3.5 (see Figure 4.16). Albeit these materials will not be commercially available for a short while, their promise for increased efficiency has strengthened the interest for TEGs in automotive applications [6]. The need for on-board thermal and electrical energy, together with their effective management, opens a wide scenario for the use of thermoelectric devices in cars. Among others, one application is for climate control. While currently available materials do not still provide efficiencies that can compete with refrigerant systems, thermoelectrics are used in some premium cars for the heating and cooling of seats. In such an application the Peltier effect is exploited by feeding with the current the thermoelectric device [86].
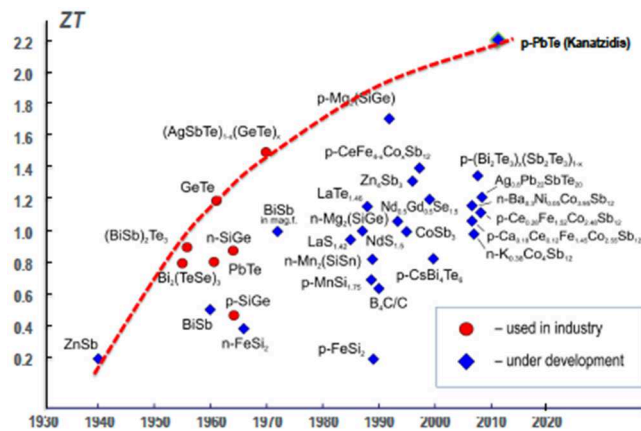
Figure 4.16 - Figure of Merit ZT improvements in the past years [87].

Although TEGs have been suggested for applications such as accelerating catalytic converter light-off and clearing particulate filters, most important application is for the recovery of waste heat. Some systems have been proposed for applications with thermal gradient between either ambient air and exhaust gases or engine cooling water and exhausted gases [80][85][88]. On a temperature gradient bases, the exhaust gases represent

the best source, but issues about heat exchanger and maximum TEG operating temperature need to be considered. In literature, for example, Crane et al. [89] developed extensive computer models of thermoelectric modules to recover waste heat in the radiator, including both transient and steady state cases. In [84][89][90] the authors attempt to optimize the actual heat recovery and thermoelectric design in accordance with automotive constraints. Key challenges include the lack of interface materials connecting the thermoelectrics and the heat sinks. These interfaces must accommodate the massive fluctuations in thermomechanical strain between heat exchangers and thermoelectric converters while providing excellent thermal and electrical contact [6]. For long time, thermoelectric waste heat recovery has been considered impractical for standard passenger vehicles because of the extremely low thermal efficiencies of thermoelectric devices [91]. Power generation thermal efficiencies for conventional bismuth-telluride (Bi_2Te_3) TEGs have been in the range of 1 to 3% depending on hot and cold side temperatures. These low efficiencies combined with the relatively high costs of the thermoelectric semiconductor materials have typically kept thermoelectrics (TEs) for being considered as a viable technology for automotive applications. A system approach can help making TE technology more feasible; radiator and wasted exhaust gases can both be used for TE generation. One of the critical challenges for implementing thermoelectric devices into automotive applications (where cost and volume limitations are critical) involves achieving adequate waste heat recovery to justify the extra costs for TEG devices. The challenge then becomes the design of the thermoelectric device such that it does not provide significant system weight penalties or impair the performance of other systems such as the engine coolant loop. This involves optimizing TEG performance within the constraints of the automotive powertrain requirements. Currently, major automotive OEMs, including BMW, FIAT, Ford, General Motors, Volkswagen, and Volvo are investing in R&D activities on thermoelectric waste heat recovery systems, with promising results [87][92]. In particular, the TEG prototype system developed by Amerigon for BMW, Ford, and General Motors has shown power output peaks of up to 608 W in testing activities with hot side and cold side of 890K and 290K, respectively [87], expecting fuel economy improvement of 2-3%. Most of the issues, due to the high temperature tolerances necessary for waste heat recovery systems, are *i)* the development and choice of the correct type of material systems, which interconnects, *ii)* the

critical safety characteristics, and *iii)* the need for low cost solutions. Indeed, the crucial challenge is making good electrical and thermal contacts. The large temperature gradient across the device puts mechanical stress on the contact-thermoelectric interface. Moreover, joining the different materials introduces resistance that heats up the contact, degrading the device. Furthermore, the integration of TEGs, heat exchangers and related power electronics implies an additional weight, which eventually reduces the benefits in terms of fuel economy. Considering that the prototypes developed so far by the automotive OEMs represent only a rough estimate of what one could expect in terms of final product, Rowe et al. [93] provided an evaluation of the weight penalty when incorporating a TEG. They calculate an additional weight of about 80 grams per generated Watt (12.5 W/kg). Finally, the cost needs to be properly assessed for a complete technical/commercial feasibility analysis. Being the technology at the prototype stage, with the focus on integration issues rather than the TEG equipment itself, it is difficult to estimate the expected production cost for commercial application. Today's commercial TEGs with ZT around 1 guarantee a gain of 5 % in fuel economy, their cost is about 30 $/W [94]. However, a cost/benefits analysis is not that trivial and should also include monetary and non-monetary benefits for the automotive industry itself (and not a simple payback estimate for customers), energy harvesting potential, future emissions regulations and related penalty costs, and should explore opportunities of innovative materials both for TEG modules and automotive components. The study carried out by LeBlanc [95] applies a new thermoelectric cost analysis, which includes material properties, device physics, material costs, manufacturing costs, and system costs. The analysis and resulting cost values provide a tool for research and development of thermoelectric device. Recent advances in thermoelectric materials are being achieved and some TEG devices, with higher operating temperatures and greater efficiencies, could be used for power generation from waste heat recovery [6]. Indeed, new TEG materials such as Zn_4Sb_3-based semiconductors offer improved performance with a broader temperature range than the conventional Bi_2Te_3-based TEG devices.

4.2.2. TEG Modeling

A simplified scheme of the TEG implemented in the engine layout is shown in Figure 4.17.
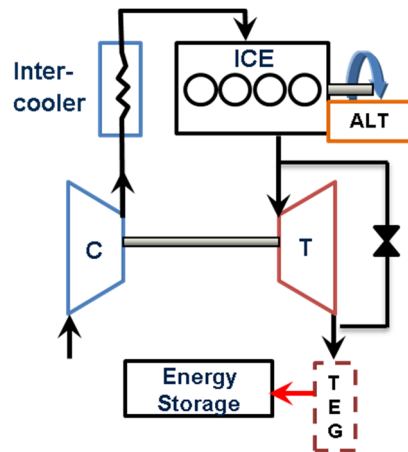
Figure 4.17 - Scheme of the engine equipped with the TEG systems, including alternator and energy storage devices.

Each TEG module is composed by a number of thermocouples electronically and thermally connected, in both series and parallel, configuration. Each thermocouple consists of two elements, namely p and n leg enclosed by two ceramic plates, as shown Figure 4.18.
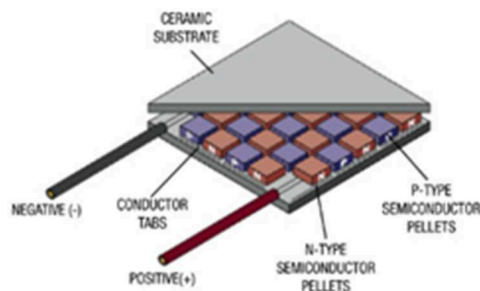
Figure 4.18 - Thermoelectric module [6].

Due to its availability, cost, and performance, Bi_2Te_3 was selected as the material for the thermoelectric modules; its properties and operating temperature range are well-suited for the presented configuration with the exhaust gases as hot side and the coolant loop as cold side. The results

presented in this work are based on the device HZ-14, produced by Hi-Z
Tecnhology, Inc. [82], with the following main characteristics:
- 49 thermocouples electronically connected in series;
- dimensions- 6.27×6.27 cm^2;
- weight- 83g;
- maximum continuous operating temperature (hot side)- 523K;
- maximum peak operating temperature (hot side)-673K;
- maximum power of 13W, with 4.5% efficiency (at optimal
  conditions of 503K at the hot side and 303K at the cold side).

It is worth noting that such specifications are provided by the
manufacturers and have not been validated/tested.

For each module, electrical and thermal characteristics (voltage V,
current I and resistance R) are estimated according to the following
equations, where the material properties are defined as the average of the p
and n legs, and n_{couple} is the number of couples in each module [96][6].

$$R_{mod} = \frac{2n_{couple}\rho}{G} \tag{4.3}$$

$$K = 2n_{couple}kG \tag{4.4}$$

$$V_{OC} = 2n_{couple}\alpha(T_h - T_c) \tag{4.5}$$

$$I = \frac{V_{OC}}{R_{mod} + R_{load}} = \frac{2n_{couple}\alpha(T_h - T_c)}{R_{mod} + R_{load}} \tag{4.6}$$

where ρ is the electrical resistivity, G the TE geometry factor, K the thermal
conductance, k the thermal conductivity and α the Seebeck coefficient. The
actual temperature of the TEG module hot and cold side plates (T_h and T_c
respectively) are useful to describe TEG performance, as depicted in Figure
4.19. The heat fluxes related to hot and cold side (Q_h and Q_c respectively)
for each module are given by equations (4.7) and (4.8), respectively.

$$Q_h = K(T_h - T_c) + 2n_{couple}\alpha T_h I - \frac{1}{2}I^2 R_{load} \tag{4.7}$$

$$Q_c = K(T_h - T_c) + 2n_{couple}\alpha T_c I + \frac{1}{2}I^2 R_{load} \tag{4.8}$$

In order to maximize the output power, the load resistance R_{load} is set to match the TEG module internal resistance [96][6]. To correlate the temperatures T_h and T_c to the temperature of the hot (h) and cold (c) fluid (T_1 and T_4 respectively), the heat exchange between the fluids and the TEG module has been modelled.

$$Q_h = U_h A\left(T_1 - T_h\right) \tag{4.9}$$

$$Q_c = U_c A\left(T_c - T_4\right) \tag{4.10}$$

where U is the overall heat transfer coefficient and A the exchange area.
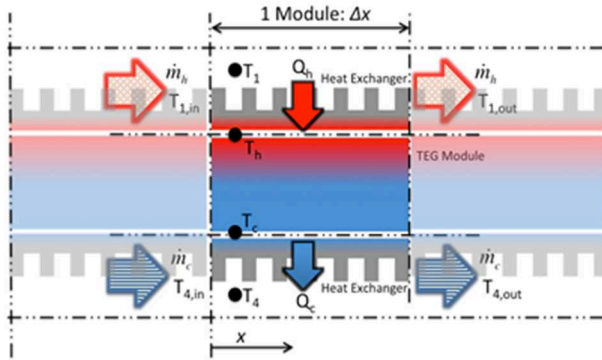
Figure 4.19 - TEG module heat flows [6].

Thus, (4.6), (4.7), (4.8), (4.9) and (4.10) represent an equations system with five unknown, i.e. Q_h, Q_c, T_h, T_c and I. For the analysed configuration, the exhaust flow rate and temperature along with incoming coolant mass flow and temperature are the inputs.

The recovered power P_{mod} and efficiency η_{TE} can be determined as

$$P_{mod} = I^2 R_{load} \tag{4.11}$$

$$\eta_{TE} = \frac{P_{mod}}{Q_h} \tag{4.12}$$

The system is solved for each module connected in series along the x-dimension assuming that: i) T_1 equals $T_{1,in}$, ii) $T_{4,out}$ of the nth module represents $T_{4,out}$ of the (n^{th}+1) module, and iii) each module is operating at the same voltage. It is worth noting that the model and is based on

manufacturers data and has not been validated by testing activities.

4.2.3. TEG-Vehicle Configuration

As discussed above, there are several options to recover waste heat in a vehicle in terms of hot and cold fluids, namely one might consider exhaust gas-coolant, exhaust gas-ambient air, coolant-ambient air, and any combination of those. The selection of the configuration is performed as function of the working temperature range of each component and the available thermoelectric material. Indeed since *i)* each material has a different optimal operating temperature range, and *ii)* for a given material, performance is a function of temperature, as shown in Figure 4.20 [97].
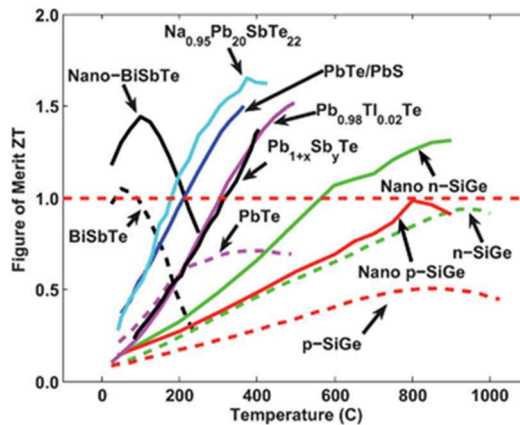
Figure 4.20 - Figure of Merit (ZT) vs. average temperature for different materials [97].

This study is focused on one specific system configuration, where hot and cold fluids are exhaust gases and the engine coolant loop, respectively. A scheme of the configuration is shown in Figure 4.21. Besides being the configuration most commonly researched and explored, it seems a good opportunity for energy recovery and the most suitable material, among ones on the market, is the Bi_2Te_3. Several analyses have been carried out for different ns × np (# modules in series × # modules parallel) TEG configurations.

Figure 4.21 - TEG waste heat recovery configuration [6].

4.2.1. TEG results

Basic TEG configuration

This section presents the main results of the analysed system in terms of fuel economy improvement and CO_2 reduction.

As discussed previously, SI engines offer more opportunities than CI engines in terms of thermoelectric waste heat recovery. Thus, the temperature of the exhaust gases in extra-urban case reaches values in the NEDC that would maximize the output of the TEG (see Figure 4.22c), thus improving its performance and potential benefits. As shown in Figure 4.22c, the exhaust gas temperature is mainly in the range 600-1000K, well above the Diesel case, favouring the TEG optimal operating conditions. In Figure 4.22b is represented the other input of the model, i.e. the exhaust gas mass flow along the NEDC. Figure 4.22d shows the recovered power by TEG, which is limited with respect to others WHRs, with a maximum value of about 200 W. This latter results requests the enabling of TEG and alternator along the entire cycle (see Figure 4.22e).

Figure 4.22 - Simulation results along the NEDC: a) measured vehicle speed profile; b) exhaust gas mass flow rate, c) exhaust gas temperature, d) Recovered TEG power, e) Activation flag for TEG and alternator.

The analysed configuration results in fuel consumption improvement and CO_2 reduction of about 1.9 and 1.5 g/km along NEDC and WLTC respectively, aligned with literature results [91][98][99][87]. It is worth

noting that even though Bi_2Te_3 represents the optimal trade-off between cost and performance, it is not the best material for thermoelectric generation. However, the reduction of about 1.5 g/km for a small passenger car can be significant in the framework of increasingly stringent environmental regulations [1].

Combination of ETC-TEG

This paragraph deals with the analysis of opportunities and challenges of combining TEG and ETC technologies for a compact car [3]. The exhaust gases after ETC still have enough energy to further thermoelectric conversion within a TEG device. Moreover, it is still guaranteed a minimum temperature for the light-off of after-treatment devices of the exhaust gas. The Figure 4.23 shows a complete scheme of the engine layout integrated with the ETC and TEG devices.
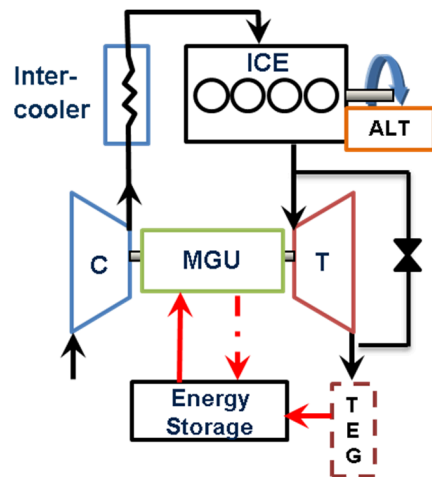
Figure 4.23 - Scheme of the engine equipped with the ETC and TEG systems, including alternator and energy storage devices [3].

The combined application of two different WHR technologies was assessed by Zhang et al. [55], who investigated the idea of coupling a TEG with an ORC system for the thermal energy recovery.
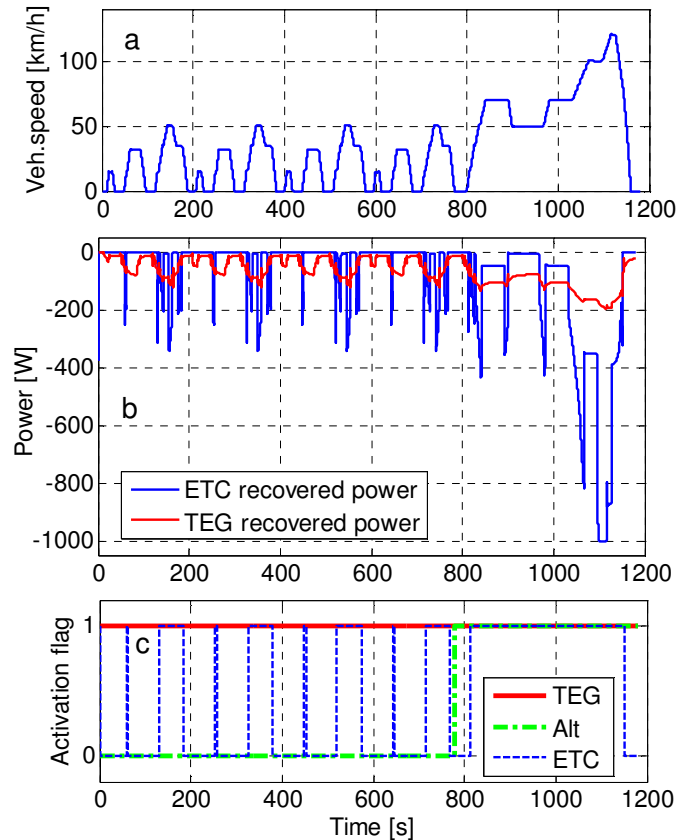
Figure 4.24 - ETC-TEG analysis on NEDC: a) measured vehicle speed profile; b) ETC and TEG recovered power; c) actuators activation (1 – on, 0 - off).

The results achieved show that the recourse to ETC and TEG devices in passenger cars could lead to an average fuel economy (and CO_2 reduction, consequently) ranging from about 3% to 5% [38][24][76] and 1% to 4% [6], respectively. To ETC control, the strategy B presented in paragraph 4.1.3 with the same hypothesis and limitations is considered, i.e., generation mode, 1 kW maximum power. The Figure 4.24 and Figure 4.25 show the time histories of vehicle speed (graphs a) and simulated recovered power (graphs b) for the NEDC and WLTC, respectively. The control strategy enables the alternator operation only in the extra-urban phase and has been proved to be the most suited for the energy recovery from the exhaust gases [24].
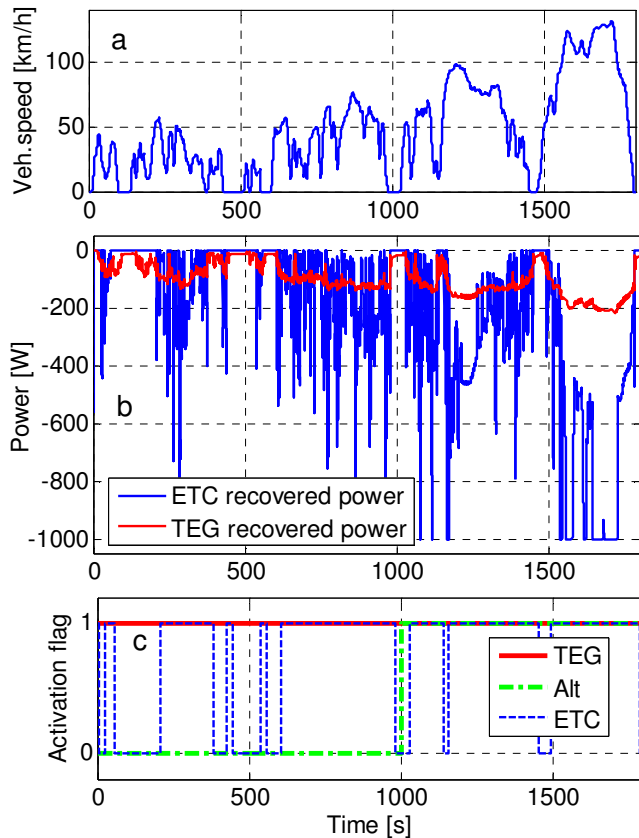
Figure 4.25 - ETC-TEG analysis on WLTC: a) measured vehicle speed profile; b) ETC and TEG recovered power; c) actuators activation (1 – on, 0 - off).

The figures evidence that the TEG system exhibits a lower recovered power than the ETC device. The activation flags for TEG, ETC and alternator shown in the lower graphs (graphs c), remark that the TEG is always operating whereas the ETC is activated only when the turbo speed exceeds the threshold value of 30000 rpm; consequently, a significant energy recovery from ETC is achieved only at high load operations.

The overall results are summarized in Figure 4.26 that shows the reduction of CO_2 emissions achieved with the TEG and the ETC for the two driving cycles considered (i.e. NEDC and WLTC). The blue bars denote the baseline case. Referring to the NEDC, a decrease of CO_2 of about 5% occurs for the vehicle equipped only with the ETC (e.g. red bar), as estimated at the previous ETC paragraph [24]. The TEG implementation

in the vehicle model allows obtaining lower savings, (1.9 % for NEDC, green bar) in terms of fuel economy and CO_2 reduction, in agreement with the values presented in the literature [6]. The greatest improvement of fuel economy and CO_2 reduction is achieved by coupling the ETC and TEG. In the NEDC, a reduction of CO_2 emissions of 5.6 % is achieved. The trend of the simulation results can be easily extended to WLTC as well. In this case a benefit in terms of fuel saving above 6% can be reached, due to the higher engine load conditions [3].
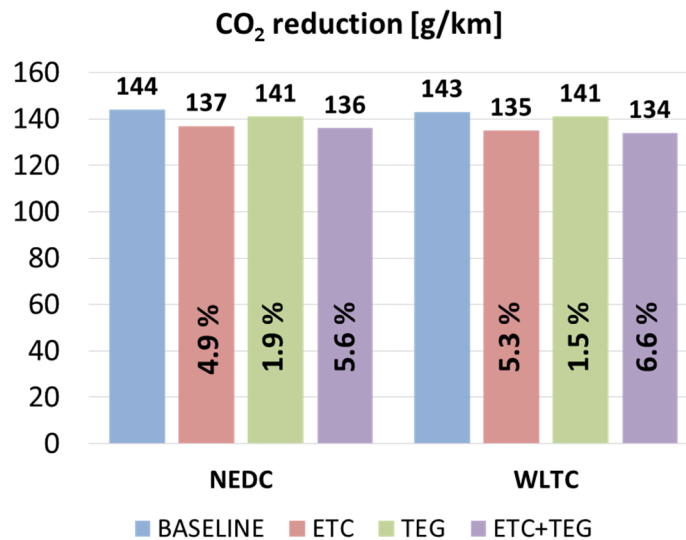
Figure 4.26 - Estimated CO_2 emissions along NEDC and WLTC. The percentages indicate the CO_2 savings vs. the baseline configuration [3].

The data on fuel saving shown are in agreement with Legros et al. [68]. The results confirm that thermoelectric generators look like not mature yet and some efficient materials have still to be developed. However, research on new materials is very active. The conventional bismuth-telluride materials are not too efficient for the typical range of temperature of gasoline engines and new materials, as 'skutterudite', seem to be the current trend and need to be manufactured [68].

4.3 Organic Rankine Cycle (ORC)

The Rankine cycle is a system particularly suitable to recover energy from low-grade heat sources. The technology has many possible applications. Among them, the most widespread and promising fields are: waste heat recovery, biomass power plant, geothermal plants and solar thermal power. The working fluid can be either water or an organic component, such as a refrigerant or a hydrocarbon- based liquid, which allows exploiting lower-temperature heat sources [100]. For waste heat recovery applications, water is not included among the working fluids because of several reasons, explained below [101]. Therefore, for energy conversion or heat recovery from lower temperature heat sources, the steam Rankine cycle (SRC) can be replaced by an Organic Rankine Cycle (ORC) using a fluid with high molecular mass and a lower boiling point than water. The working fluids should include other desirable characteristics such as low latent heat, high critical temperature and pressure, suitable specific volume, low density and surface tension, high thermal conductivity, high thermal stability, non-corrosive, non-toxic, and compatibility with engine materials [102]. Thus, from the literature analysis [103][8], the working fluid R123 was selected for the current study. The four main components of the Rankine cycle are evaporator, expander, condenser and pump and the four corresponding thermodynamic processes are vaporization, expansion, condensation and compression (see Figure 4.27, where a prototype of an ORC plant developed by University of Purdue [104] is represented). A volumetric expander is used instead of a turbine, due to the small size of the plant for the required purpose. Other variants of the basic cycle can be obtained with the use of different components. These solutions can increase the cycle thermal efficiency through additional transformations such as reheating and regeneration [105].

The ORC section is divided into four parts: the first one deals with state of art; the second part refers to modeling and validation of the ORC system; the third takes into account for the system components sizing and an optimal control strategy; the latter deals with the simulation results. The identification and validation of the ORC model were carried out versus experimental data available from the literature, collected on a test rig whose configuration is reported in [106].
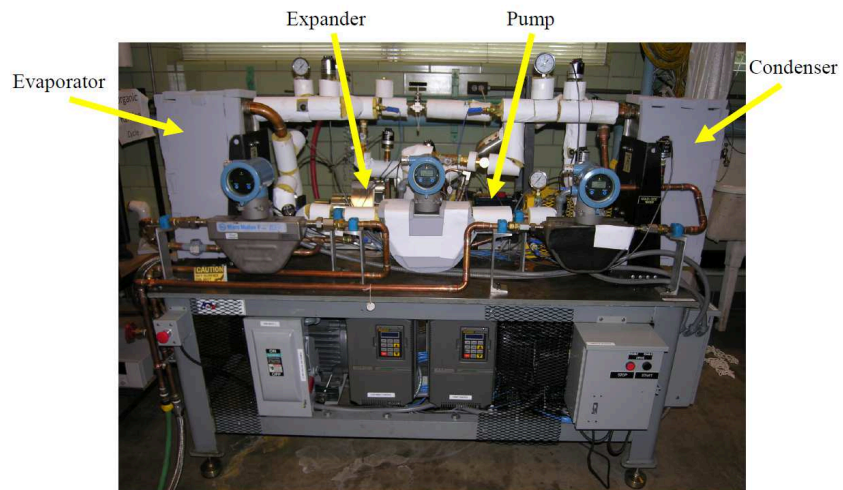
Figure 4.27 - Prototype of ORC plant [104].

4.3.1. ORC – State of art

The first studies and applications of the engine-ORC compound were specific for heavy-duty vehicles and arose during the energy crisis in 1970s. In 1976, indeed, Patel and Doyle [107] developed the first application for exploiting an ORC for automotive engine, using the exhaust waste heat of a Mack 676 Diesel engine installed in a long haul truck duty cycle. The constructed prototype showed an improvement of fuel economy of 12.5%. Heywood [35] in 1981 proposed a review of the possible alternative systems to be coupled to conventional engines. The several solutions showed that the ORC plant could guarantee a reduction of fuel consumption of about 10-15 % on Diesel engines. Several studies were carried out on ORC systems in the following years; among these assume importance the comparison of the performance for different cycles applied to a Diesel engine [108], the design of the ORC control system [109] and the comparison among seven working fluids [110]. The effective interest of the automotive industry towards the waste heat recovery via ORC was neglected during the 90s and the beginning of the 2000's. The cause is probably due to considerable room for improvement of engine efficiency achievable with cheaper solutions, as reported from Tona et al. [105] and Colonna et al. [101] in their analyses of the state of art.

Recently, several contributions have been presented in the literature regarding the ORC applications mainly for heavy-duty engines

[111][112][113]. These engines operate with significantly higher exhaust temperatures than light duty engines, with higher potential benefits. In order to implement the ORC systems on passenger car, many studies have been made in the last years [114][102]. An important challenge for light-duty diesel engines is to be able to fulfil the thermal requirements of exhaust after-treatment systems. Crialesi Esposito et al. [115] focused on the optimization and control of an ORC system for automotive engine waste heat recovery. The results showed a fuel saving of about 6 % during the acceleration-deceleration transient. Edwards et al. [116] have investigated the effect of efficiency-improvement strategies (cylinder deactivation and turbo-compounding), on the steady-state performance of the ORC. Moreover, an analysis on the impact of the residual thermal energy on the aftertreatment efficiency has also been carried out. Finally, from the literature studies, it can be expected that the ORC systems for automotive applications have a potential to achieve a reduction of CO_2 emissions ranging from 3 to 8 % [111].

4.3.2. ORC Modeling

The reference plant, whose scheme is depicted in Figure 4.28, involves an ORC system thermally coupled to the engine exhaust pipe and an auxiliary battery pack. The ORC system is placed downstream the turbine exhaust pipe. The exhaust gases downstream the turbine and the ambient air are considered as hot fluid for the evaporator and cold fluid for the condenser, respectively.

Figure 4.28 - Scheme of the engine equipped with the ORC system, including alternator and energy storage devices [111].

The evaporator of the ORC system is described through a grey-box model that takes in account the equations describing both thermodynamic and heat exchange phenomena. Due to the lack of useful data on ORC for automotive use, it has decided to exploit data from solar application [106]. These data are accurated and detailed, and the characteristics of the plant from which the measurements were taken are available and complete. In such a plant the hot source is a solar pipe. However, the use of these data required several analyses to account for the basic parameters of the solar plant that were then used for the purpose of the automotive WHR. Among these the design of the heat exchanger was the most critical point. The components (pump, expander and condenser) are modeled through a black-box approach. Moreover, an optimal sizing for all components was carried out in order to obtain the best results with reference to vehicle application. As aforementioned, an Organic Rankine Cycle is aimed at partially recovering the waste heat from the engine by the heat exchange between organic fluid and engine exhaust flow. The organic fluid follows an evaporation process within the heat exchanger, afterwards it evolves as superheated vapour in a volumetric expander (e.g. Scroll) directly coupled to an alternator to produce electrical energy. The electrical energy is then stored into a battery pack and used to feed auxiliaries. Figure 4.29 shows the relationships among the system components.

Figure 4.29 - Scheme of the ORC plant model [111].

The input variables of the ORC system are the pump rotational speed, which sets the organic fluid flow rate, and the expander rotational speed, which influences the evaporation temperature. These control variables are managed in order to optimize the cycle efficiency, for each engine working conditions. Furthermore, the following hypothesis are assumed: *i*) the condensation pressure is set constant; *ii*) the cooling of the organic fluid in liquid phase into the condenser is set constant; *iii*) the outlet temperatures of pump and expander are evaluated through a polytrophic process [111]. In the following paragraphs, the sub-models of the ORC system components are described.

Pump model
The volumetric pump considered for the ORC system was modeled through a black-box approach that implies the characterization of isentropic efficiency as a function of working fluid mass flow rate and enthalpies in the suction and exhaust sections [111]. The mass flow through the pump $\dot{m}_r$ was evaluated by the following equation

$$\dot{m}_r = \frac{X_{pp}\dot{V}_{pp,max}}{v_{in,p}} \tag{4.13}$$

where X_{pp} is the pump volumetric fraction, linked to the operating frequency, $\dot{V}_{spmax}$ is the maximum pump flow rate and $v_{in,p}$ is the specific volume of the organic fluid in the suction section. The pump power $\dot{W}_{pp}$ was then evaluated by the equation

$$\dot{W}_{pp} = \frac{\dot{m}_r(h_{ex,p,is} - h_{in,p})}{\eta_{pp}}$$

(4.14)

where η_{pp} is the pump efficiency, $h_{ex,p,is}$ and $h_{in,p}$ are the exhaust isentropic and inlet pump enthalpy, respectively.

Evaporator model

The countercurrent evaporator is divided into three zones, each one is representative of the organic fluid physic state. The purpose of this model is to evaluate the outlet heat exchanger temperature of both fluids by considering the transferred heat and neglecting the pressure drop along the pipes. The exhaust engine flow rate represents the hot fluid while the organic fluid is the cold one. The evaporator was firstly modelled by means of a grey-box approach, afterwards a black-box model was developed to achieve lower computational burden. The scheme of the countercurrent evaporator is reported in Figure 4.30.
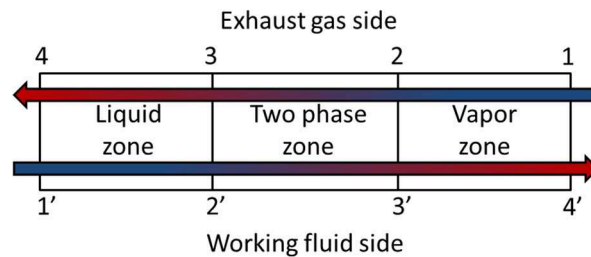
Figure 4.30 - Scheme of the countercurrent evaporator [111].

Grey-box model
The grey-box model assumes as input variables the flow rates and the inlet temperatures of both the organic and the hot fluid, the evaporating pressure, the thermal transmittance for each zone and the total exchanging area. The total area was evaluated with the following equation

$$A_l + A_{tp} + A_v = (N_p - 2)LW$$

(4.15)

where A represents the exchanging area of the several zones of the evaporator, N_p the numbers of plates of the heat exchanger, L and W the length and the width of the heat exchanger plates, respectively.

The thermal transmittance U for each zone is evaluated by means of the following equation

$$\frac{1}{U} = \frac{1}{h_r} + \frac{1}{h_{sf}} \tag{4.16}$$

where h_r and h_{sf} are the convective resistances of organic and secondary fluid respectively. In case of a single phase zone, these parameters are dependent on fluid speed and viscosity by means of Reynolds, Prandtl and Nusselt numbers. On the other hand, in case of two phases, as during boiling and condensation processes, the parameters are calculated by the Hsieh and Kuo correlations, respectively [106]. By applying the thermal energy equation for each zone, the following set of nonlinear equations is obtained

$$\dot{Q}_l = m_{hf} c_{p,hf} (T_3 - T_4)$$

$$\dot{Q}_{lat} = m_{hf} c_{p,hf} (T_2 - T_3)$$

$$\dot{Q}_{surr} = m_r c_{p,r} (T_{4'} - T_{3'}) = m_{hf} c_{p,hf} (T_1 - T_2)$$

$$\dot{Q}_l = A_l U_l \left(-\left(\frac{T_{1'} + T_{2'}}{2} \right) + \left(\frac{T_4 + T_3}{2} \right) \right) \tag{4.17}$$

$$\dot{Q}_{lat} = A_{tp} U_{tp} \left(\left(\frac{T_2 + T_3}{2} \right) - T_{2'} \right)$$

$$\dot{Q}_{surr} = m_r c_{p,r} (T_{4'} - T_{3'}) = A_v U_v \left(\left(\frac{T_2 + T_1}{2} \right) - \left(\frac{T_{3'} + T_{4'}}{2} \right) \right)$$

$$A_l + A_v + A_{tp} = (N_p - 1) LW$$

The model outputs are the areas of each zone and the outlet temperatures of organic and secondary fluids. The grey-box model is applied to evaluate the heat exchanger efficiency vs. the engine operating conditions, in order to calibrate the black-box model parameters [111].

Black-box model
The black-box model is based on synthetic functional relationships with the

aim to speed-up the computational time for potential real-time application [111]. The model parameters are calibrated by a set of data, generated by exploiting the grey-box model in a wide engine operating range.

The modeling approach used for the countercurrent evaporator is known in literature as ε - NTU method [34]. The total transferred heat within the evaporator was calculated through the following equation

$$\dot{Q}_{ev} = \varepsilon C_{min} \Delta T_{max} \tag{4.18}$$

where, ε is the efficiency of the exchanger, C_{min} is the minimum thermal flow among the fluids and ΔT_{max} is the maximum temperature difference over the exchanger and is evaluated by subtracting the inlet organic fluid temperature $T_{1'}$ from the inlet hot fluid temperature T_1. The exchanger efficiency was previously characterized as a function of the fluids flow rates and ΔT_{max}. The outlet hot fluid temperature T_4 is the result of the equation (4.18) by considering the power balance over the hot fluid.

$$\dot{Q}_{ev} = \varepsilon C_{min} \Delta T_{max} = m_{hf} c_{p,hf} (T_4 - T_1) \Rightarrow T_4 \tag{4.19}$$

By imposing the equality between the equation (4.18) and the sum of liquid phase heating $\dot{Q}_l$, latent heat $\dot{Q}_{lat}$ and vapor phase superheating $\dot{Q}_{surr}$, the outlet cold fluid temperature $T_{4'}$ was evaluated

$$\dot{Q}_{ev} = \varepsilon C_{min} \Delta T_{max} = \dot{Q}_l + \dot{Q}_{lat} + \dot{Q}_{surr} \Rightarrow T_{4'} \tag{4.20}$$

Scroll expander model

The Scroll expander model evaluates the adiabatic efficiency and the filling factor, both expressed as function of the organic fluid density in the expander inlet, expander rotational speed and expansion ratio. The inlet fluid specific volume $v_{in,exp}$ can be determined by using the filling factor φ, previously identified on experimental data [106]

$$v_{in,exp} = \frac{\varphi \dot{V}_{s,exp}}{\dot{m}_r} \tag{4.21}$$

Thus, the inlet expander pressure can be evaluated once the inlet density and temperature are known. The expansion was modeled as a two-step process: an adiabatic reversible expansion and a constant volume expansion, as reported in the following equation

$$\dot{W}_{exp} = \dot{m}_r [(h_{in,exp} - h_{m,is,exp}) +$$
$$+ v_{in,exp}(p_{m,exp} - p_{ex,exp})] \qquad (4.22)$$

Condenser model

The condenser model is based on the same black-box approach of the evaporator. The exchanger efficiency is expressed as a function of the organic fluid flow rate and the inlet temperature of both organic fluid and cold fluid (i.e. ambient air). This model was used to evaluate the cold fluid outlet temperature while the organic fluid outlet temperature is considered constant by imposing either the condensation pressure and the liquid cooling.

ORC model validation

The models of the ORC components were validated against literature experimental data [106]. A good correlation is obtained for each model, ranging from 0.85 to 0.98. The graphs in Figure 4.31 show the comparison between predicted and measured adiabatic efficiency of the pump, thermal power of evaporator and condenser and expander power, evidencing very good fittings.
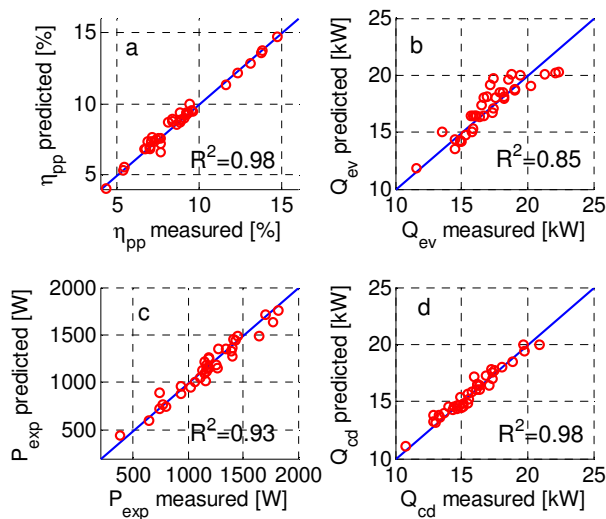
Figure 4.31 - Validation results of the ORC components models, with respect to literature experimental data: a) pump isentropic efficiency, b) evaporator power, c) expander power, d) condenser power.

4.3.3. ORC Component sizing and Control

The pump displacement was defined according to the engine working conditions (i.e. exhaust temperature and flow rate), to obtain a balanced heat flow from the exhausted gases towards the organic fluid.

The countercurrent evaporator is composed of N plates with a specific size. The exchanging area sizing was assessed through a sensitivity analysis on the grey-box model in order to obtain, in the worst conditions, a title equal to 1 at the exchanger outlet. A similar approach was used for the condenser; particularly, the exchanging area was chosen to have an optimal condensation pressure. A further analysis was carried out, taking into account the possibility to use the water of the engine cooling plant as coolant fluid in the condenser, against the ambient air. This choice results in higher coolant temperature (323 K with respect to 296 K assumed for the ambient air), but a more compact condenser size, due to the higher heat exchange coefficient of coolant fluid than the ambient air.

The Scroll expander volume was determined by means of a sensitivity analysis in order to maximize the ORC output power according to engine operating conditions. Therefore, the expander displacement was set to be suitable for the pump characteristics.

The ORC system presents two control variables, namely pump and expander rotational speed, and two external inputs corresponding to the exhaust gas flow rate and temperature. The evaporation temperature (and pressure) is controlled through the expander rotational speed, while the overheating is imposed by regulating the coolant mass flow rate, operating on the pump working frequency. In order to maximize the ORC thermodynamic efficiency along the vehicle driving transient, an optimization analysis was carried out to evaluate the reference values of evaporation temperature ($T_{ev}*$) and overheating ($\Delta T_{3'4'}*$). The optimization process was implemented with constraints on *i*) the maximum organic fluid temperature, that must be lower than the critical temperature, and *ii*) the exhaust gas temperature downstream the evaporator, that must be maintained within a suitable range to guarantee efficient catalyst operation. For the ORC control, both reference evaporation temperature and overheating were expressed as function of the engine exhaust flow rate and temperature. It is worth noting that the most efficient working condition can be identified through the following path: *i*) reduction of the minimum temperature and pressure of the organic fluid; *ii*) decrease of the evaporator

overheating and *iii*) identification of the optimal evaporation temperature and pressure (see Figure 4.32). This latter task has to be pursued by considering the following opposite effects: on the one hand, an increase of the evaporation temperature results in better cycle efficiency and greater expander specific work, due to the higher pressure ratio; on the other hand, it leads to lower adiabatic efficiency of the expander, due to the major losses.
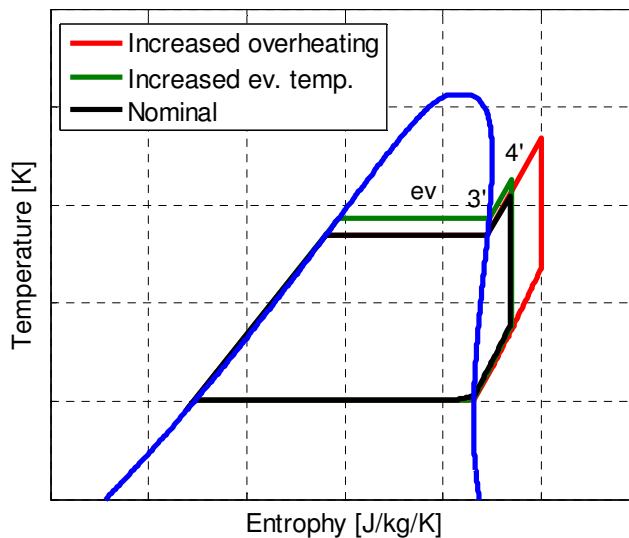
Figure 4.32 - Qualitative representation of the ORC on T-s diagram in nominal condition (black curve) against the cycles obtained with variation of overheating (red curve) and evaporation temperature (green curve) [111].

The ORC control (see Figure 4.33) is performed by applying two PI controllers to the pump frequency and the expander rotational speed: the first one operates adapting the organic fluid overheating to the reference value, the latter works on the error between the effective and the reference evaporation temperature. An increase of the organic fluid flow rate, due to a high pump speed, results in a lower heat exchange and in increased intake expander pressure and density with enhanced expander efficiency and output power. A reduction of the expander speed, at constant flow rate, leads to increased evaporation pressure and, consequently, thermodynamic cycle efficiency [111].
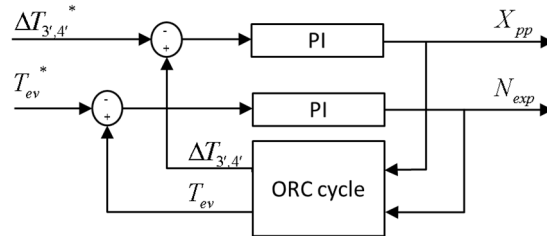
Figure 4.33 - Scheme of the ORC control [111].

4.3.4. ORC Results

In the present section the simulation results achieved by the powertrain-ORC model along the driving cycles NEDC and WLTC are presented [111]. The simulations were carried out considering the additional weight (30 kg) of the ORC plant. The plots of Figure 4.34 show the simulated time histories of the engine variables assumed as ORC model inputs, namely the exhaust gas mass flow rate and temperature. It is worth noting that the former 500 s of the NEDC refer to engine cold operation, before reaching the steady thermal state. The thermal dynamics of the exhaust gas temperature during engine warm-up was simulated by means of a first order system, whose time constant was identified against experimental data collected at the vehicle test rig. The simulations presented refer to cold start conditions; in case of hot start, as prescribed by regulations, slightly increased benefits are expected.
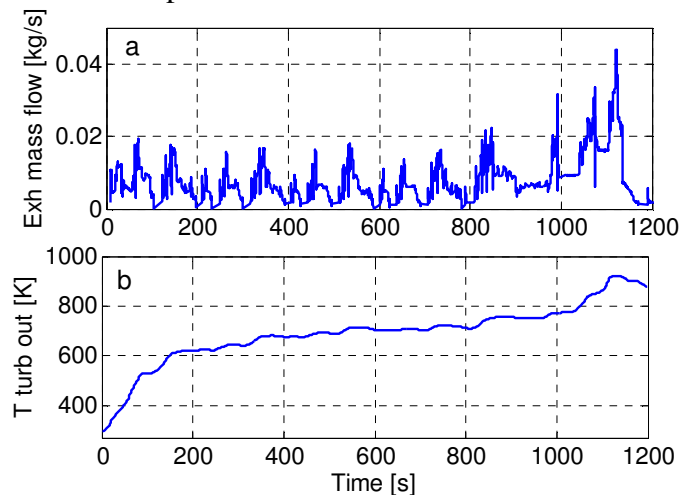
Figure 4.34 Time histories of the simulated mass flow rate (a) and temperature (b) of the exhaust gas along the NEDC.
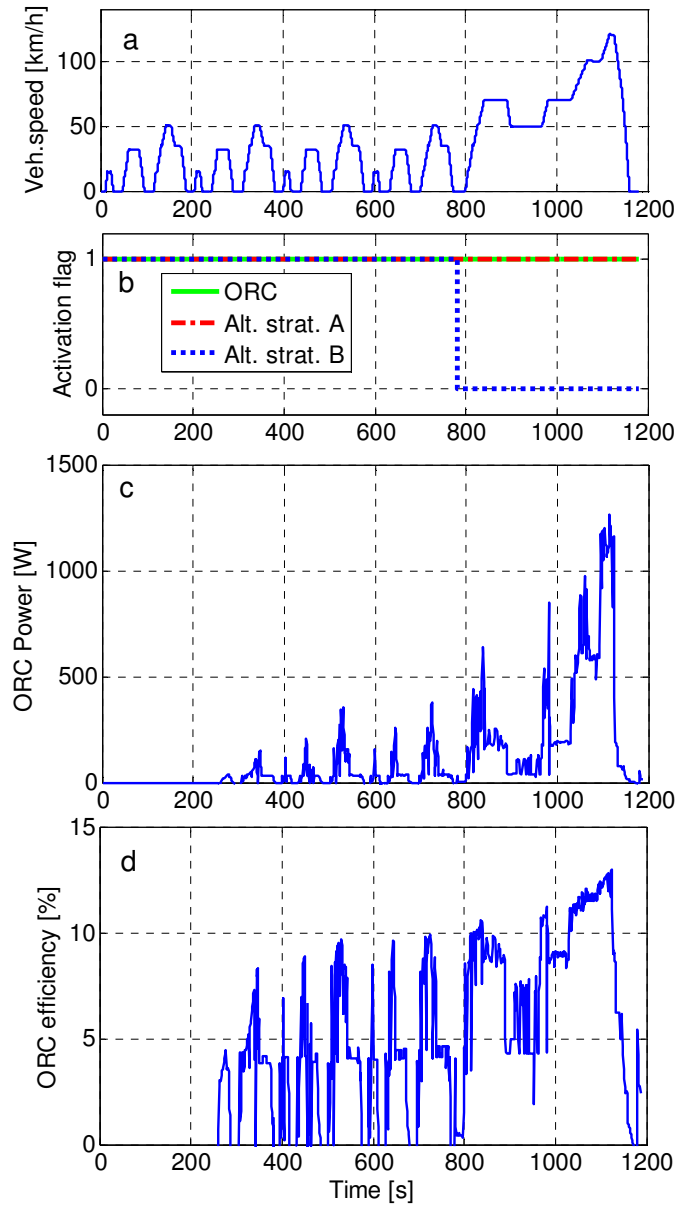
Figure 4.35 - Simulation results along the NEDC: a) NEDC profile, b) Activation flag for ORC and alternator (A and B strategy), c) Recovered ORC power, d) ORC efficiency.

The benefits achievable by the ORC are also dependent on the management strategies applied to the alternator. In the ETC and TEG analysis, different targets may be achieved in terms of CO_2 reduction depending on the alternator operation and the amount of recovered power supplied to the auxiliary loads. In the simulation analyses, the ORC recovered power was evaluated as the difference between the expander and pump power. The recovered energy is stored into a battery pack and then used on demand to drive the electric auxiliaries depending on the management strategy of the alternator. Two different strategies, namely A and B, were introduced for the alternator management. In the former case (i.e. strategy A) the alternator operates along the whole driving transient; on the other hand the strategy B enables alternator operation only at low load, as in the urban phase of NEDC and WLTC while the alternator is electrically disconnected at high load. In both cases, the constraint to recover the initial battery SOC at the end of the driving cycle is imposed. It is worth remarking that the amount of recovered power in the extra-urban phase is sufficient to power the auxiliaries, thus allowing the alternator disablement. Figure 4.35 a and b show the alternator and ORC operation along the NEDC, evidencing the effects of the two alternator strategies (A- dashed-dotted-red line, B – dotted-blue line). Figure 4.35c shows the time history of the power recovered from the ORC system along the NEDC with the B strategy, that guarantees better results in terms of CO_2 reduction. For the strategy B, the activation of the alternator during the urban phase allows overloading of the ICE, which works in low efficiency, with an increasing of the engine efficiency and of both mass flow rate and temperature of the exhaust gases. Thus, the activation of the ORC is fast, the recovered power is high and the absorbed energy compensates and exceeds the energy used to feed the auxiliaries by the alternator. The electric recovered power is obtained by considering a generator efficiency equal to 0.85 [100]. The introduction of the ORC system in the conventional vehicle architecture, without implementing a suitable management of the alternator (A strategy), results in a CO_2 reduction of 3.4 % for both NEDC and WLTC. Better results are achieved by implementing the B strategy for the alternator, with a reduction of CO_2 emissions of 3.7 % and 4 % along the NEDC and WLTC, respectively. The outlet ORC temperature actuation was set in order to promote a fast warm-up of the after-treatment devices. Consequently, during the first urban module of the NEDC, the ORC is disabled because of the low temperature of the exhaust gas during the engine cold operation.

After the engine warm-up, the trend of power recovered from the ORC system increases with the exhaust gas temperature, reaching peak values close to 1200 W during the extra-urban phase, considerably larger than the alternator load. Figure 4.35d shows the time history of the estimated ORC efficiency along the NEDC. The peak values do not exceed 13 %, in accordance with the results presented in the literature. The simulations performed along the WLTC driving cycle present similar results: the application of the ORC allows recharging the battery to power the electric auxiliaries through the recovered energy and always results in an increase of fuel economy. Further improvements are observed when the strategy B is applied. The overall results are summarized in Figure 4.36 which shows the reduction of CO_2 emissions achieved with the ORC implementation compared to the baseline case (blue bars), for the different alternator management strategies (red and green bars) investigated. It is worth noting that the WLTC exhibits the major reduction of CO_2, due to the higher engine load conditions, with an improvement of fuel economy up to 4 % when the strategy B is applied. Further simulations were performed by considering the engine coolant as cold fluid for the condenser (violet bars). The results evidenced lower recovered power and benefits in CO_2 reduction; nevertheless, it is worth remarking that this solution allows reducing the size of the condenser, thus resulting in a more feasible solution for compact cars. Furthermore, the engine coolant temperature is roughly constant compared to the ambient air, thus ensuring more stable performance of the ORC system, almost regardless to ambient conditions.
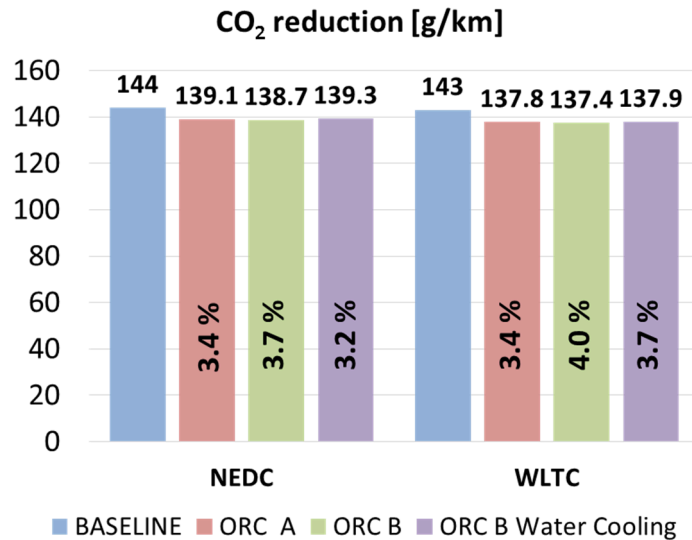
Figure 4.36 - Estimated overall CO₂ emissions along the NEDC and WLTC, for the two management alternator strategies (A and B) and with the engine cooling water as cold fluid of the condenser [111].

4.4 WHRs Conclusions

The performed simulations of several vehicle-powertrains allows to evaluate available exhaust energy for different drive cycles and to understand the opportunity and potentialities of the WHRs. For the sake of brevity, these simulations are reported for only one application. However, the main objective of this activity is to focus on the benefits achievable from several WHRs or combination of these ones. The results follow the trend already analysed in literature [68] and indicate that important CO_2 reduction from the WHRs are difficult to achieve in light-duty conventional vehicles, respect the heavy-duty vehicles. It is worth pointing out that from the simulations carried out for Alfa Romeo Giulietta equipped with 1.4 l gasoline engine, the WHR systems for automotive applications have potential to achieve a reduction of CO_2 emissions ranging from 1.5 to 6.6 %, as reported in the histogram of Figure 4.37.
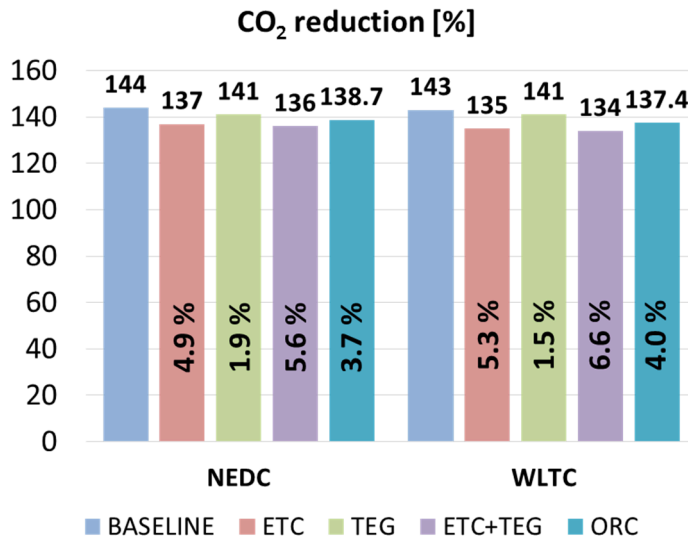
Figure 4.37 - Estimated overall CO₂ emissions along the NEDC and WLTC, for the different waste heat recovery systems.

As shown by Legros [68], the turbocompounding and Organic Rankine cycles systems are the most probable technologies to be soon integrated into passenger cars. Thermoelectric generators lack of produced power and are not mature yet. They could become interesting to use when new materials will guarantee an optimum trade-off between the efficiency and the cost. Another important feature that penalizes the thermoelectric generators, but favours the ETC, is the weight to power ratio. The ETC has proved the most advantageous technology, reaching a fuel saving up to 4.9 % for the NEDC and 5.3 % for the WLTC. The combining of the ETC with the TEG leads to further gain of almost one point of percentage.
The enhancements obtained through the WHRs can further increase if other advanced technologies are accounted to improve further the engines efficiency [5].

CHAPTER 5

Conclusions and perspectives

In order to face with the increasing EU restrictions imposed on CO2 emissions from light-duty vehicles, new concepts such as hybrid powertrains as well as Waste Heat Recovery (WHR) technologies have been proposed in the last years by OEMs. The hybridization and electrification of the vehicles are now under active development by many car companies, thanks to their significant potential in reducing CO2 emissions. More innovative WHR technologies include Electric Turbo-Compound (ETC), Thermo-Electric Generator (TEG) and Organic Rankine Cycle (ORC); though they have been successfully tested on few heavy-duty applications, have not been proved yet as effective and affordable for passenger cars. In this work, the investigation of several hybrid configurations, advanced technologies to improve the engine efficiency and WHR systems has been analysed to better understand the opportunities and limitations for their use on passenger cars in the next years.

For the purpose of this study, a comprehensive framework has been developed; it is made of several submodels implemented in a computational platform for easy management and use. The vehicle-powertrain model is a structure that has been developed in order to simulate easily, quickly and with high accuracy a wide variety of different vehicles, components, devices and technologies. This has been obtained thanks to the modular and scalability properties of the models. The main components simulated are internal combustion engine, gearbox, turbo, electrical system, etc. Attention is given to the implementation of complex numerical interaction among the submodels, which implement basic control commands as well. Connections are established to account for both mechanical (between ICE and wheels, by passing through the entire drivetrain) and electric energy flows (between alternator, battery and electric loads). The modeling approach is based on a set of grey-box dynamic models of intake/exhaust manifolds, turbocharger and vehicle longitudinal dynamics coupled with black-box parametric models for in-cylinder processes and friction losses.

The model has been identified and validated against steady-state and transient experimental data.

An extended list of technologies for the improvement of the overall energy conversion efficiency has been compiled, in order to investigate their impact on the emission of CO_2 on test cycles NEDC and WLTC. The Willans line methodology used to model the ICE has been exploited in order to analyse the influence of the several technological improvements on the engine efficiency. Performance and fuel consumption enhancements have occurred and a full path of CO_2 reduction for these technologies has been presented exhibiting variations from 2% up to about 20%. The most important contribution is given by the downsizing of the engine and the cylinder de-activation technologies, that singularly ensure about 10 % of CO_2 reduction. Furthermore, an accurate description of several hybrid configurations and their control strategies has been presented; a thorough analysis of the simulations results for the standard driving cycles is reported and discussed to evaluate their impact on fuel economy and thus on CO_2 emissions. Three parallel hybrid configurations have been studied to evaluate the advantages and the drawbacks and to quantify the CO_2 reduction with respect to the baseline configuration. The performed simulations have proved that hybridization of the vehicles allows obtaining an average saving of about 12 %, making feasible the achievement of 2020 CO_2 reduction targets for Large/SUV segment. It has demonstrated that the matching of the vehicle equipped with the more efficient engine, obtained with the technological improvements, and the explored hybrid configurations can allow reaching about 27 % of maximum reduction of CO_2. Moreover, several configurations of a fuel cell hybrid vehicle have been simulated and a comprehensive well-to-wheel analysis has been performed, accounting also for the CO_2 due to the production and distribution of both hydrogen and gasoline. The range extender solution has shown the major saving of fuel consumption, among the explored configurations. These improvements though not yet implementable in a short while can fulfill the CO_2 target of 2020 and beyond, making the technology appealing for future powertrains.

Summarizing, hybrid vehicles are the most viable alternative solution to reduce the greenhouse gas emissions. If important evolutions on the electric energy storage and fuel cell technology will be achieved, both range extender (based on either ICE or FC) and plug-in hybrid configurations can demonstrate to be the best answer to address

environmental issues.

The WHR technologies have been compared accounting for their technical benefits and drawbacks; moreover the results of the simulations completed the study with a quantitative analysis of their advantages. It has been observed that TEGs present the lower benefit in terms of CO2 reduction, but can be coupled with the ETC to obtain the most useful system (up to 6.6 % of fuel saving), guaranteeing the needed light-off temperature of the exhaust gases for effective catalyst operations. Although technologically feasible, ETC, TEG and ORC are not yet mature for a large-scale production and implementation. As evidenced by the results of the simulations, they offer significant improvements on fuel economy and CO2 reduction. However, a suitable management of their operation has to be properly designed to account for engine speed, load and auxiliaries demand.

Such WHR technologies present a great potential for energy savings and can play a role in responding to increasingly strict emission standards and in maintaining the ICEs very competitive. However, further work is required to make WHRs feasible for their application on board of light duty vehicles; the main research areas deal with i) materials for more efficient TEGs; ii) electric machines running at high speed for ETCs and iii) packaging solutions for on-board installation of ORCs.

This dissertation provides a comprehensive framework to analyze those technologies that can promote the development of more efficient propulsion systems. At simulation level further enhancements are envisaged to better support the design of new powertrains either conventional or hybrid with WHR. Among others, the vehicle-powertrain model can be extended, by adding submodels of pollutant emissions [117] and after-treatment devices. Further developments towards deeper study of some technologies could be undertaken, starting from the design and development of ETC, TEG and ORC plants linked with the engine. Other work can approach the study of new hybrid architecture far from the current conventional series/parallel ones, integrating also the WHRs and electric after-treatment devices. Lastly, a cost analysis for all solutions studied should be performed to appraise their feasibility with respect to the constraints imposed by the automotive market.

APPENDIX

Engine maps scaling up/down

In this section, a procedure for the scaling up/down of the internal combustion engines is reported [12].
The following expressions are used to scale the model

$$v_{pist,scaled} = v_{pist,model} \frac{S_{scaled}}{S_{model}} \tag{6.1}$$

$$amep_{scaled} = amep_{model} \frac{V_{d,model}}{V_{d,scaled}} \tag{6.2}$$

$$bmep_{scaled} = \left[e_0 \left(v_{pist,scaled} \right) - e_1 \left(v_{pist,scaled} \right) \cdot amep_{scaled} \right] \cdot$$
$$\cdot amep_{scaled} - fmep \left(v_{pist,scaled} \right) \tag{6.3}$$

$$T_{e,scaled} = bmep_{scaled} \frac{V_{d,scaled}}{4\pi} \tag{6.4}$$

$$\omega_{scaled} = v_{pist,scaled} \frac{\pi}{S_{scaled}} \tag{6.5}$$

Therefore, it is possible to compute the fuel flow rate scaled map by the following expression

$$\dot{m}_{scaled} = amep_{scaled} \cdot \omega_{scaled} \frac{V_{d,scaled}}{4\pi \cdot H_{LHV}} \tag{6.6}$$

The joint analysis of Willans line affine relationship and specific parameters correlations highlights how, overall, a quadratic dependence of *bmep* on *amep* is recommended to be considered [26]. Thus, the identification of the Willans line coefficients for each class of membership allows creating a suitable database to identify the best configuration for a vehicle, as well as for providing a useful tool for powertrain components

design. Moreover, this method allows generating excellent scalable control algorithms for hybrid vehicles (but in general for any type of vehicle) based on the efficiency maps.

This study was carried out by analysing four different engines, namely two spark ignition (SI) naturally aspirated and two compression ignition (CI) turbocharged. The model structure was suitably adapted to the differences between the two engine configurations, without being excessively altered, thus preserving its generalization for the subsequent extension to other engines. The experimental data were collected at the engine test bench in steady-state conditions. Results presented later show the influence of the components on the engine efficiency maps.

Table 6.1 shows the data related to the engines considered. Class 1 denotes spark ignition engines, whereas Class 2 refers to compression ignition engines.

A separate complete procedure description, i.e. ranging from parameters identification to subsequent model validation, is presented and discussed for each engine class. Particularly, model validation is performed by exploiting identified Willans line coefficients to scale engine performance from large/small to small/large displacement. In order to verify both scaling up and down accuracy by Willans line, two identifications and two scaling procedures relative to SI and CI engines were carried out, analysing first the downsizing and then the oversizing of the engine, respectively. It is worth mentioning here that accuracy obtained when inverting the above described process (exchanging SI downsizing by oversizing and thus the opposite for CI engine) was also successfully verified. Nevertheless, the latter process was not included for sake of brevity.

Table 6.1 - Technical sheet of studied engines. A and B refer to Large and small engine, respectively.

	Class : 1, SI		Class : 2, CI	
Size	A	B	A	B
Cycle	Otto	Otto	Diesel	Diesel
Strokes	4	4	4	4
Max Power (kW)	38.6	25	102.6	67.2
Max Torque (Nm)	115.62	102	305.2	115.62
Cylinders	4	4	4	4
Disposition	In - Line	In – Line	In - Line	In - Line
Bore (mm)	72	70.8	82	69.6
Stroke (mm)	84	78.89	90.4	82
Displacement (cm3)	1368	1242	1909	1248
Compression ratio	11:1	10:1	18:1	16.8:1
H_{LHV} (MJ/kg)	44	44	44.4	44.4
Valves	8	8	16	16
Intake valves per cylinder	1	1	2	2
Intake valve head diameter (mm)	34.85	34.27	28.13	23.9
Equivalent piston skirt length (mm)	37.22	36.6	51	43.3
Emission standard	Euro3	Euro2	Euro3	Euro5

Results Yielded by the Identification Procedure for Engine Class 1, A

The first step of parameters identification defines the set of parameters of the equations (2.7) for the reference SI engine. The following Table 6.2 lists the values yielded on output by this first identification task. It is worth remarking here that parameters e_{10} and e_{11} were removed from identification due to their negligible contribution to modeling accuracy,

which was verified by applying the backward stepwise technique.

Table 6.2 - Outcomes of Willans line curve-fitting applied to Engine Class1, A.

Parameter	Value
e_{00}	0.226
e_{01}	0.022
e_{02}	-0.001
$ploss_0$	0.886
$ploss_2$	0.003

The graph at the left side of the Figure 6.1 shows a comparison between the experimental *bmep* and corresponding values resulting from the identification of Willans line model parameters, evidencing a very good fitting (R^2=0.9964).
Figure 6.1 highlights in the graph on the right the satisfactory accuracy of the Willans line model in approximating the experimental data, consisting of 71 engine points evenly distributed throughout the engine operation range. Despite its apparent simplicity, this representation of the internal combustion engine efficiency or fuel consumption map fairly reproduces actual engine data [118].
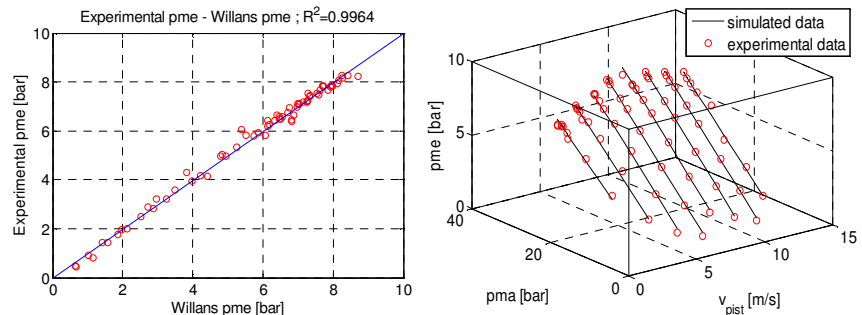
Figure 6.1 - Comparison between measured and simulated BMEP, Engine Class 1, A (left side) and comparison between Willans line model and experimental data, grouped by engine speed, Engine Class 1, A (right side).

Figure 6.2 shows the efficiency maps obtained from experimental data and Willans line model, respectively. The comparison shows how well the model approximates the engine behaviour; it is clear that the main discrepancies occur nearby the extreme points, at high torque, high engine

speed or both.

The parameters identified for the reference engine can be exploited to reproduce the behaviour of all engines belonging to the same class, taking into account only the information related to displacement and stroke.

Model Validation for Engine Class 1, B

The Willans line model identified for the engine 'Class 1, A' was applied to evaluate the performance of an engine 'Class 1, B'. Figure 6.3 shows the good agreement of the estimated *bmep*, vs. the corresponding measured data, with correlation index equal to 0.9923 and the comparison between experimental *bmep* and corresponding brake mean effective pressure values estimated by Willans line scaled model for Engine Class 1, B.
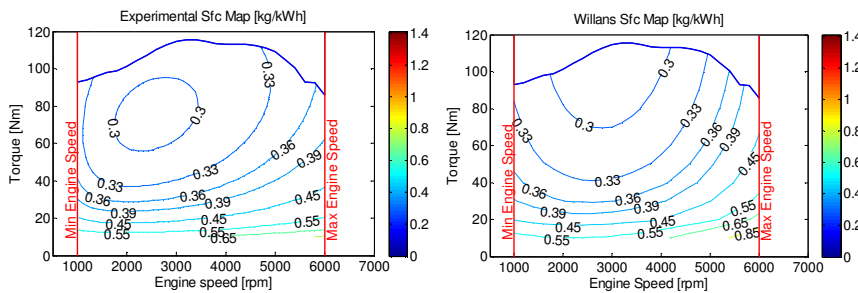
**Figure 6.2 - Specific fuel consumption map obtained by experimental data, Engine Class 1, A (left side) and Specific fuel consumption map obtained by Willans line model, Engine Class 1, A (right side).**
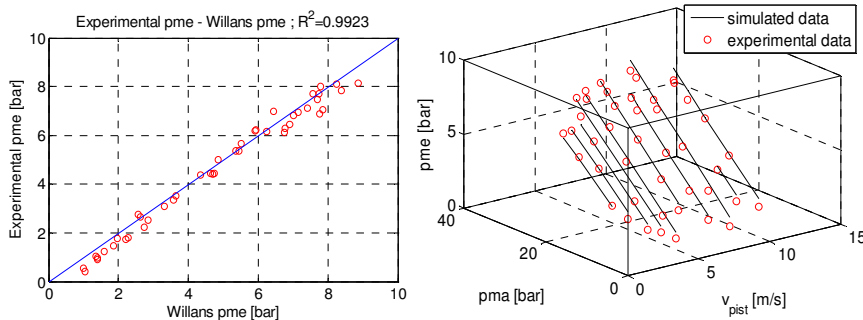

Figure 6.3 - Engine Class1, B scaled with data from engine Class1 A (left side) and Engine Class1, B scaled with data from engine Class1 A (right side).

The efficiency maps, related to experimental data and Willans model

outputs obtained via engine scaling, are represented in Figure 6.4.

In this case, the efficiency maps, apparently similar, show different trends in terms of amplitudes and concavities. This result is probably due to the presence of the alternator in the engine Class 1 A layout, whereas the experimental measurements on engine Class 1 B were conducted by disconnecting this component.
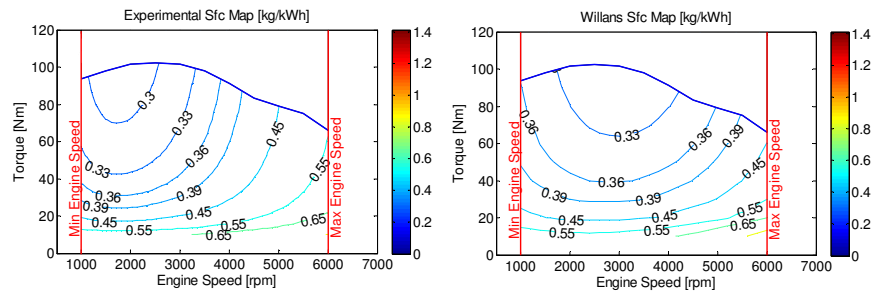
Figure 6.4 - Specific fuel consumption map of engine Class 1 B obtained with experimental data (left side) and Specific fuel consumption map of scaled engine Class 1 B (right side).

Verification of Willans Line-Based Evaluation of Engine Class 1, A Losses

In this section, a comparison between overall losses estimated via Willans line approach and those calculated by the Bishop-based mathematical model is made. Particularly, the following losses contributions are considered by summing up the relative mathematical relationships expressed by equations (2.10), (2.11), (2.12), (2.13) and (2.14):

1. Piston mechanical losses, corresponding to *fmep$_5$*.
2. Blow-by, corresponding to *fmep$_4$*.
3. Crankcase losses, summing up *fmep$_1$* and *fmep$_2$*.
4. Auxiliary losses, corresponding to *fmep$_3$*.

The graph on the left side of Figure 6.5 shows the distribution of the mechanical losses obtained by using the mathematical model, with labels expressing the losses grouping described above. On the same plot, the variation of Willans line derived losses as a function of speed is superimposed, highlighting the very good agreement between overall losses estimated with mathematical model and Willans line-based estimation, thus confirming the goodness of the procedure.

Afterwards, the comprehensive losses estimation performed via Willans

line approach is coupled to literature derived information on losses sharing [35][119], this time also including the auxiliary losses sub-sharing, as shown on the right graph of the Figure 6.5. The losses grouping as addressed by Bishop-based estimation is confirmed. Moreover, the combination of Willans line findings, with average shares derived from literature information, is suitable to enable subsequent deployment, e.g. for analysing the effect due to engine losses when varying engine size in hybrid vehicle design optimization tasks.
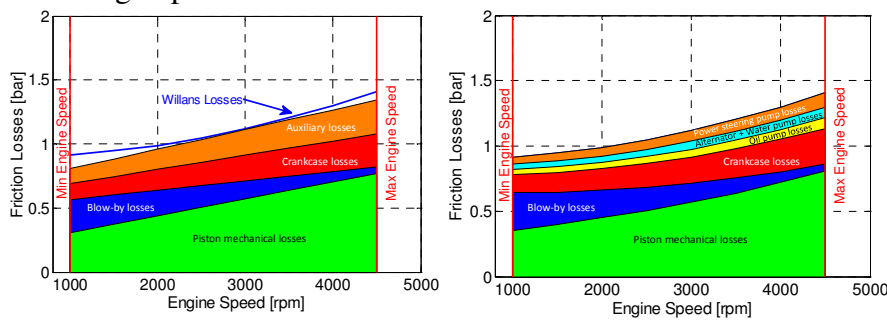
Figure 6.5 - Distribution of friction losses obtained through the mathematical model [29] applied to engine Class 1 A (left side) and Distribution of friction losses obtained via the coupling of Willans line based estimation with literature derived losses sharing, as indicated in [30] and [35] (right side).

Results yielded by the identification procedure for Engine Class 2, B

The experimental data-set is composed of 132 engine points evenly distributed throughout the operation range. Figure 6.6 shows the comparison between measured and simulated *bmep* values for the CI engine (Class 2, B). The correlation index value is close to unity with R^2 equal to 0.9988.

The analysis of the efficiency maps shown in Figure 6.7 apparently denotes a different behavior. The reason of this discrepancy is based on the engine technology: experimental data for engine Class 2 (both A and B) were obtained considering the EGR device. Therefore, the little error occurring in the estimation of the efficiency map might be especially due to the different VGT control strategies that are most likely adopted on the two engines, whereas EGR effect mostly impacts at low loads. However, the fact that the model does not account for such high-detail level aspects is acceptable when considering the end applications of the proposed software

tool.
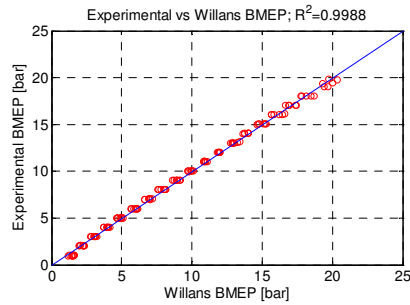
Figure 6.6 - Comparison between measured and simulated BMEP values, Engine Class 2, B.

Figure 6.7 - Specific fuel consumption map obtained by experimental data. Engine Class 2, B (left side) and Specific fuel consumption map obtained with Willans line model. Engine Class 2, B (right side).

Model Validation for Engine Class 2, A

To validate the model, the same procedure adopted in the previous section about engine Class 1 was used. Using the coefficients identified on engine Class 2 B, it was possible to develop the Willans line model to evaluate a different engine, this time larger than that considered for parameters identification. Figure 6.8 shows the scaling phase from engine Class 2 B to engine Class 2 A: the results evidence a good agreement (with R^2 equal to 0.9880) between original and scaled model. Afterwards, the efficiency maps were analysed, by comparing the experimental one (Figure 6.9 left side) with that achieved by scaling the engine Class 2 A (Figure 6.9 right side). The efficiency maps are very similar, showing similar pattern, gradients and concavity. Differences can only be noted at high engine speed; however, considering that a compression ignition engine rarely

works at speeds above 4000 rpm and, moreover, until this point simulated maps well approximate the experimental maps trend, it is possible to conclude that the results are satisfactory. The small discrepancy can be again justified considering the different EGR and VGT control strategies adopted on the two engines.
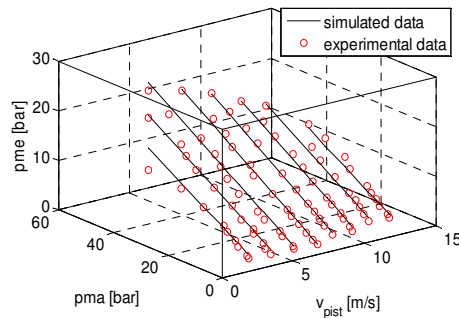
Figure 6.8 - Engine Class 2 A scaled with data from engine Class 2 B.
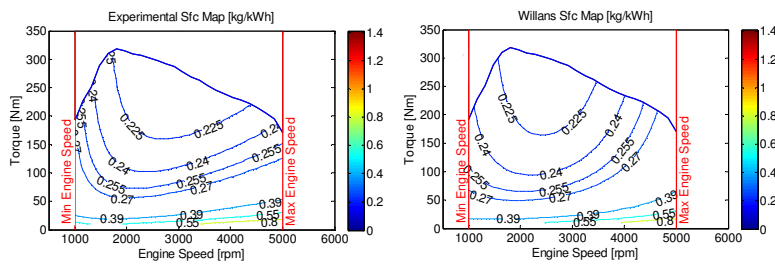
Figure 6.9 - Specific fuel consumption map of engine Class 2 A obtained with experimental data (left side) and Specific fuel consumption map of scaled engine Class 2 A, obtained by applying Willans line (right side).

Verification of Willans line-based evaluation of Engine Class 2, B losses

The graph in left side of Figure 6.10 illustrates the comparison between the mechanical losses estimated with the mathematical model proposed by Bishop, while the right graph shows the literature derived losses shares applied to the Willans line model.

The comparisons illustrated in Figure 6.10 highlight the closeness between reference mathematical model [30][29] and the software tool here developed (which actually proposes to combine information inferred from

Willans line identification with literature derived mechanical and auxiliary losses). It is worth remarking here, however, that the Bishop model [30][29] was developed in the 60s for spark ignition engines. Thus, extension to a different technology, such as CI Diesel engine, obviously requires suitable precautions when deriving information on losses computation. Particularly, in case of CI engine, differently from SI, no auxiliary sub-sharing was applied (see Figure 6.10 right side), since the non-negligible effect of injection pump has also to be accounted for.
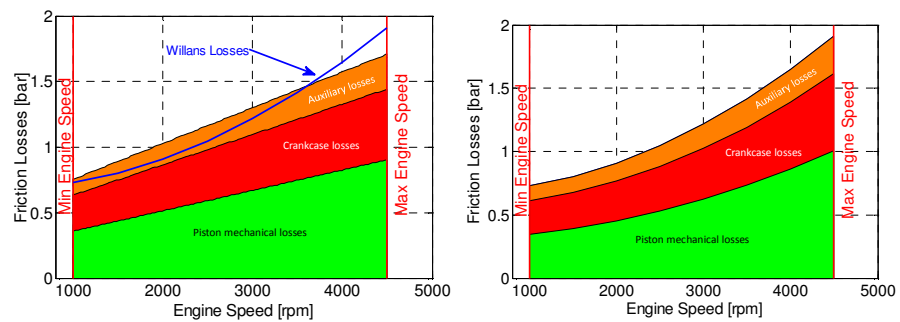
Figure 6.10 - Distribution of friction losses obtained through the mathematical model applied to engine Class 2 B (left side) and Distribution of friction losses obtained via the coupling of Willans line based estimation and literature derived information, as indicated in [30] and [35] (right side).

Engine Losses Model Validation

A specific analysis was carried out to validate the Willans line based estimation of mechanical losses for the engine 'Class 1, A (i.e. large gasoline engine, see Table 6.1)', via comparison between simulated and experimental data. The experimental mechanical losses were evaluated by processing the measured in-cylinder pressure cycles and the analysis was carried out under different engine operating conditions. Figure 6.11 (left side) shows some exemplary indicated cycles obtained for different load conditions. The following equations enable proper estimation of engine mechanical losses as a function of indicated mean effective pressure *imep*.

$$bmep = \eta_{org} \cdot imep \quad \leftrightarrow \quad fmep = bmep - imep \tag{6.7}$$

Figure 6.11 (right side) shows the comparison between the mechanical losses evaluated from the experimental data (i.e. indicated pressure cycles), where the percentage values displayed in red, blue and yellow bars

represent different load conditions, and those calculated by the Willans line and Bishop-based mathematical models. At different values of engine speed, the mechanical losses estimated through the Willans line model increase with a quadratic function, and slightly differ from the value calculated from the experimental data considering a medium load. Assuming that the model developed is not configured as a tool for calculating the mechanical losses, but rather as a modeling and simulation support for preliminary assessment and approximation of corresponding losses shares, as well as for fuel consumption and efficiency, the trend of the calculated engine losses appears quite satisfactory when compared to experimental results. Therefore, above discussed experimental verification of Willans line based prediction of overall engine losses well supports one of the main contributions of this paper, namely the extension of Willans line method deployability to accounting for the influence of engine size modification on each single engine loss, as previously discussed (see Figure 6.5, along with related comments given within the text). Particularly, the modeling tool here proposed is expected to provide relevant preliminary insight on the potential reduction of engine losses attainable via suitable design improvement, as well as by the adoption of innovative hardware and related control strategies.

|	1500	2000	2500	3000	3500	4000
Low Load	0,6916	0,7084	1,3307	1,1743	1,0539	1,159
Medium Load	0,8357	1,0175	1,4831	0,9724	1,1542	1,5582
High Load	1,2794	1,3723	1,5364	1,154	1,2896	1,3156
Ploss Willans Model	0,9439	0,9891	1,047	1,118	1,202	1,299
Ploss Bishop Model	0,8056	0,8823	0,9591	1,036	1,113	1,189
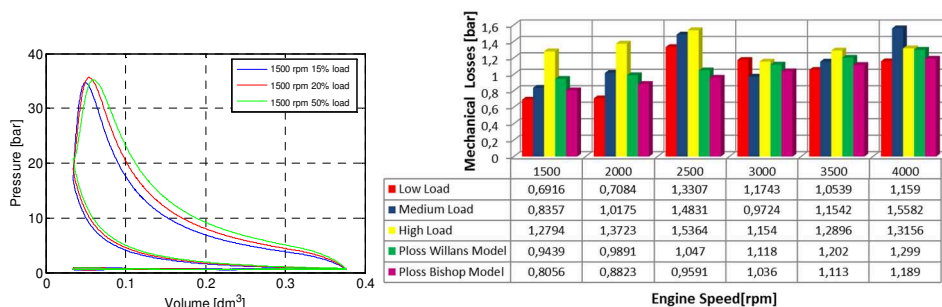
Figure 6.11 - Indicated cycles for different load conditions (left side) and Comparison between experimentally derived mechanical losses and corresponding values resulting from Willans line model identification (right side).

Acknowledgements

References

[1]   European Commission, "Technical Guidelines for the preparation of applications for the approval of innovative technologies pursuant to Regulation (EC) No 443/2009 of The European Parliament and of the Council ," version: February 2013.

[2]   European Environment Agency, "Monitoring CO_2 emissions from passenger cars and vans in 2013," EEA Technical report, No 19/2014, 2014.

[3]   Arsie, I., Cricchio, A., Pianese, C. Ricciardi, V., and De Cesare, M., "Modeling Analysis of Waste Heat Recovery via Thermo-Electric Generator and Electric Turbo-Compound for CO_2 Reduction in Automotive SI Engines," ATI 2015 – 70th Conference of the ATI Engineering Association, Energy Procedia 82 (2015) 81-88, 2015.

[4]   Kabza, H., "Hybrid Electric Vehicles: Overview," Elsevier B.V., 2009.

[5]   Shabashevic, A., Richards, N., Hwang, J., Erickson, P.A., "Analysis of powertrain in design on effective waste heat recovery from conventional and hybrid electric vehicles," Applied Energy 157 (2015) 754-761, 2015.

[6]   Arsie, I., Cricchio, A., Marano, V., Pianese, C., De Cesare, M., Nesci, W., "Modeling Analysis of Waste Heat Recovery via Thermo Electric Generators for Fuel Economy Improvement and CO_2 Reduction in Small Diesel Engines," SAE Int. J. Passeng. Cars - Electron. Electr. Syst., 7 (1), 2014.

[7]   Gabriel-Buenaventura, A., Azzopardi, B., "Energy recovery systems for retrofitting in internal combustion engine vehicles: A review of techniques," Renewable and Sustainable Energy Reviews 41 (2015) 955–964, 2015.

[8]   Tahani, M., Javan, S., and Biglari, M., "A comprehensive study on waste heat recovery from internal combustion engines using organic rankine cycle," Thermal Science, Vol.17, pp.611-624, doi:10.2298/TSCI111219051T, 2013.

[9]   Karvonen, M., Kapoor, R., Uusitalo, A., Ojanen, V., "Technology competition in the internal combustion engine waste heat recovery:

a patent landscape analysis," Journal of Cleaner Production 112 (2016) 3735-3743, 2015.

[10]   Liu, J., Peng, H., and Filipi, Z., "Modeling and Analysis of the Toyota Hybrid System," Proceedings pf the 2006 IEEE/ASME, International Conference on Advanced Intelligent Mechatronics, Monterey, California, USA, 24-28 July, 2006.

[11]   Criscuolo, I., "Optimization of SI and CI engine control strategies via integrated simulation of combustion and turbocharging," Ph.D. Thesis, University of Salerno, Italy, 2012.

[12]   Sorrentino, M., Mauramati, F., Arsie, I., Cricchio, A. et al., "Application of Willans Line Method for Internal Combustion Engines Scalability towards the Design and Optimization of Eco-Innovation Solutions," SAE Technical Paper 2015-24-2397, doi:10.4271/2015-24-2397, 2015.

[13]   Rizzoni, G., Guezennec, Y., Brahma, A., Wei, X. et al., "VP-SIM: A Unified Approach to Energy and Power Flow Modeling Simulation and Analysis of Hybrid Vehicles," SAE Technical Paper 2000-01-1565, doi:10.4271/2000-01-1565, 2000.

[14]   Paganelli, G., Ercole, G., Brahma, A., Guezennec, Y., and Rizzoni, G., "General Supervisory Control Policy for the Energy Optimization of Charge-Sustaining Hybrid Electric Vehicles," JSAE Review, Vol. 22, no. 4, Pages 511-518, October 2001.

[15]   Baglione, M.L., "Development of system analysis methodologies and tools for modeling and optimizing vehicle system efficiency," Ph.D. Thesis, University of Michigan, Michigan, US, 2007.

[16]   Wipke, K.B., Cuddy, M.R., and Burch, S.D., "ADVISOR 2.1: A User- Friendly Advanced Powertrain Simulation Using a Combined Backward/ Forward Approach," IEEE Transactions on Vehicular Technology, vol. 48, 1751-1761, 1999.

[17]   Rousseau, A., Pagerit, S., Monnet, G., Feng, A., "The New PNGV System Analysis Toolkit PSAT v4.1 – Evolution and Improvement," SAE Paper 2001-01-2536, 2001.

[18]   Berry, A., Blissett, M., Steiber, J., Tobin, A., McBroom, S., "A New Approach to Improving Fuel Economy and Performance Prediction through Coupled Thermal Systems Simulation," SAE Paper 2002-01-1208, 2002.

[19]   Assanis, D., Filipi, Z., Gravante, S., Grohnke, S., Gui, X., Louca, L., Rideout, G., Stein, J., Wang, Y., "Validation and Use of

SIMULINK Integrated, High Fidelity, Engine-In-Vehicle Simulation of the International Class VI Truck," SAE Paper 2000-01-0288, 2000.

[20] Arsie, I., Pianese, C., Rizzo, G., Flora, R. et al., "A Computer Code for S.I. Engine Control and Powertrain Simulation," SAE Technical Paper 2000-01-0938, doi:10.4271/2000-01-0938, 2000.

[21] Arsie, I., De Franceschi, F., Pianese, C., Rizzo, G., "ODECS – A Computer Code for the Optimal Design of S.I. Engine Control Strategies," SAE Technical Paper 960359, 1996.

[22] Canova, M., "Fluid Systems Dynamics Modeling for Control: Internal Combustion Engines Case Studies," Ph.D. Thesis, University of Parma, Italy, 2006.

[23] Guzzella, L., Sciarretta, A., "Vehicle Propulsion Systems, Introduction to Modeling and Optimization," Springer, 2005.

[24] Arsie, I., Cricchio, A., Pianese, C. Ricciardi, V., and De Cesare, M., "Evaluation of CO_2 reduction in SI engines with Electric Turbo-Compound by dynamic powertrain modelling," IFAC-PapersOnLine, Volume 48, Issue 15, 2015, Pages 93–100, 4th IFAC Workshop on Engine and Powertrain Control, Simulation and Modeling E-COSM 2015 — Columbus, Ohio, USA, 23-26 August 2015.

[25] Wei, W., Zhuge, W., Zhang, Y., and He, Y., "Comparative study on electric turbo-compounding systems for gasoline engine exhaust energy recovery," Proc. of ASME Turbo Expo, June 14-18, 2010, Glasgow, UK, 2010.

[26] Rizzoni, G., Guzzella, L. and Baumann, B.M., "Unified Modeling of Hybrid Electric Vehicle Drivetrains," IEEE/ASME Transactions on Mechatronics, Vol. 4, no. 3, September 1999.

[27] Musardo, C., and Staccia, B., Master Dissertation: "Energy Management Strategies for Hybrid Electric Vehicles," Politecnico di Milano, Facoltà Di Ingegneria, M.Sc. in Computer Science, 2003.

[28] Zuurendonk, B., "Advanced Fuel Consumption Emission Modeling using Willans Line scaling techniques for engines," DCT 2005.116, Traineeship report, Technische Universiteit Eindhoven, Department Mechanical Engineering, Dynamics and Control Technology Group, 2005.

[29] Lee, S., Shannon, B., Mikulec, A., and Vrsek, G., "Applications of

Friction Algorithms for Rapid Engine Concept Assessments," SAE Technical Paper 1999-01-0558, doi:10.4271/1999-01-0558, 1999.

[30] Bishop, I., "Effect of Design Variables on Friction and Economy," SAE Technical Paper 640807, doi:10.4271/640807, 1964.

[31] Fons, M., Muller, M., Chevalier, A., Vigild, C. et al., "Mean Value Engine Modelling of an SI Engine with EGR," SAE Technical Paper 1999-01-0909, doi: 10.4271/1999-01-0909, 1999.

[32] Arsie, I., Cricchio, A., Pianese, C. and De Cesare, M., "Real-Time Estimation of Intake O2 Concentration in Turbocharged Common-Rail Diesel Engines," SAE Int. J. Engines 6(1):2013, doi:10.4271/2013-01-0343, 2013.

[33] Wahlstrom, J., Eriksson, L., "Modeling diesel engines with a variable-geometry turbocharger and exhaust gas recirculation by optimization of model parameters for capturing non-linear system dynamics," Proc. of the Institution of Mechanical Engineers, Part. D, Journal of Automobile Engineering, 225 (7), 2011.

[34] Muller, M., Hendricks, E., Sorenson, S.C., "Mean Value Modelling of Turbocharged Spark Ignition Engines," SAE Technical Paper 980784, 1998.

[35] Heywood, J.B., "Internal Combustion Engine Fundamentals," McGraw-Hill, 1988.

[36] Canova, M., Garzarella, L., Ghisolfi, M., Guezennec, Y., Midlam-Mohler, S., and Rizzoni, G., "A Mean-Value Model of a Turbocharged HCCI Diesel Engine with External Mixture Formation," SAE Technical Paper 2005-24-034, 2005.

[37] Eriksson, L., Lindell, T., Leufven, O., and Thomasson, A., " Scalable Component-Based Modeling for Optimizing Engines with Supercharging, E-Boost and Turbocompound Concepts," SAE Int. J. Engines 5(2):2012, doi: 10.4271/2012-01-0713, 2012.

[38] Arsie, I., Cricchio, A., Pianese, C., De Cesare, M., Nesci, W., "A Comprehensive Powertrain Model to Evaluate the Benefits of Electric Turbo Compound (ETC) in Reducing CO_2 Emissions from Small Diesel Passenger Cars," SAE Technical Paper 2014-01-1650, 2014.

[39] Jensen, J.P., Kristensen, A.F., Sorensen, S.C., Houbak, N., and Hendricks, E., "Mean value modeling of a small turbocharged diesel engine". SAE Technical Paper 910070, 1991.

[40] El Hadef, J., Colin, G., Talon, V., Chamaillard, Y., "New Physics-

Based Turbocharger Data-Maps Extrapolation Algorithms: Validation on a Spark- Ignited Engine," Proc. Of 2012 IFAC Workshop on Engine and Powertrain Control, Simulation and Modeling (ECOSM12), Rueil-Malmaison, France, 2012.

[41] Cros, J., Radaorozandry, L., Figueroa, J., and Viarouge, P., "Influence of the magnetic model accuracy on the optimal design of a car alternator," COMPEL - The International Journal for Computation and Mathematics in Electrical and Electronic Engineering, 27 (1): 196 – 204, 2008.

[42] Sorrentino, M., Rizzo, G., and Vasca, F., "An Energetic Comparison for Hybrid Vehicles Ranging from Low to High Degree of Hybridization," SAE Technical Paper 2011-24-0086, 2011.

[43] Mecker, C., "Shaping the Future – Innovations for Efficient Mobility," Normandy Motor Meetings, 2014.

[44] U.S.DOE, "FY 2014 Progress Report for Advanced Combustion Engine Research and Development," Energy Efficiency and Renewable Energy Vehicle Technologies Office, December 2014.

[45] Holmberg, K., Andersson, P., Erdemir, A., "Global energy consumption due to friction in passenger cars," Tribology International 47(2012) 221-234, 2012.

[46] Tomanik, E., Dezotti, R., Gomes, L., "Low Friction Components for Reduced Fuel Consuption on Flex Fuel Engine," Mahle Metal Leve SA, 2014.

[47] Xin, Q., Pinzon, C.F., "Improving the environmental performance of heavy-duty vehicles and engines: key issues and system design approaches – Alternative Fuels and Advanced Vehicle Technologies for Improved Environmental Performance," Woodhead publishing series in energy, Navistar Inc., USA, DOI: 10.1533/9780857097422.2.225, 2014.

[48] Roujol, S., Joumard, R., "Influence of passenger car auxiliaries on pollutant emission factors within the Artemis model," Atmospheric Enviroment, Vol 43, Issue 5, February 2009, pp 1008-1014, Air pollutant Related to Transport, doi: 10.1016/j.atmosenv.2008.01.016, 2016.

[49] Dingle, P.J.G., "Fuel injection systems for heavy-duty diesel engines - Advanced Direct Injection Combustion Engine Technologies and Development," in Zhao H (ed.), Volume 2:

Diesel Engines, Woodhead Publishing, Cambridge, UK, pp. 289–316.

[50] Millo, F., Ferrero Giacominetto, P., Gianoglio Bernardi, M., "Analysis of different exhaust gas recirculation architectures for passenger car Diesel engines," Applied Energy 98 (2012) 79–91, 2012.

[51] Park, Y., Bae, C., "Experimental study on the effects of high/low pressure EGR proportion in a passenger car diesel engine," Applied Energy 133 (2014) 308–316, 2014.

[52] Hu, B., Copeland, C., Lu, P., Akehurst, S. et al., "A New De-throttling Concept in a Twin-Charged Gasoline Engine System," SAE Int. J. Engines 8(4):1553-1561, doi:10.4271/2015-01-1258, 2015.

[53] Hung, N., S., "Rotordynamics of Automotive Turbochargers," Springer, 2015.

[54] Chambon, P., Huff, S., Norman, K., Edwards, K. et al., "European Lean Gasoline Direct Injection Vehicle Benchmark," SAE Technical Paper 2011-01-1218, doi:10.4271/2011-01-1218, 2011.

[55] Zhang, C., Shu, G.Q., Tian, H., Wei, H., Yu G., Liang Y., "Theoretical Analysis of a Combined Thermoelectric Generator (TEG) and Dual-loop Organic Rankine Cycle (DORC) System Using for Engines' Exhaust Waste Heat Recovery," SAE Technical Paper 2014-01-0670, 2014.

[56] Chan, C.C., "The state of the art of Electric, Hybrid, and Fuel Cell Vehicles," Proc. IEEE, vol. 95, no. 4, Apr. 2007.

[57] Bitsche, O., and Gutmann, G., "System for Hybrid Cars," Journal of Power Sources 127(2004) 8-15, 2004.

[58] Steffan, R., Hofmann, P., Geringer, B., "Potentials of a 48 Volt Belt-Starter-Generator in the Powertrain of an Ultra-Light Vehicle," SAE Technical Paper 2015-01-1155, 2015.

[59] Amisano, F., Raimondi, M., "AMT + Electric traction: the Most Efficient Car Transmission," 10th International CTI Symposium, Berlin, 6-7 December 2011.

[60] Ellinger, R., Meitz, K., Prenninger, P.; Salchenegger, S., and Brandstatter, W., "Comparison of CO_2 Emission Levels for Internal Combustion Engine and Fuel Cell Automotive Propulsion Systems," SAE Technical Paper 2001-01-3751, 2001.

[61] Spendelow, J., and Marcinkoski, J., "DOE Fuel Cell technologies

Program Record," U.S. Department of Energy (Hydrogen Program), 2012.

[62] Larminie, J. , and Dicks, A., "Fuel Cell Systems Explained, 2nd Edition," Wiley, 2003.

[63] Arsie, I., Di Domenico, A., Pianese, C., Sorrentino, M., "Modeling and Analysis of Transient Behavior of Polymer Electrolyte Membrane Fuel Cell Hybrid Vehicles," Journal of Fuel Cell Science and Technology, Vol. 4/261, 2007.

[64] Sorrentino, M., Pianese, C., Maiorino, M., "An integrated mathematical tool aimed at developing highly performing and cost-effective fuel cell hybrid vehicles," Journal of Power Sources 221 (2013) 308e317, 2013.

[65] Di Domenico, A., "A Dynamic model of automotive PEM Fuel Cell System for powertrain Design, Control and hierarchical model identification within Hardware in the Loop Fuel Cell Hybrid Testing," Ph.D. Thesis, University of Salerno, Italy, 2006.

[66] Edwards, R., Larivé, J.F., Rickeard, D., Weindorf, W., "Well-To-Tank Appendix 4 – Version 4a, Description , results and input data per pathway," Well-to-wheels analysis of future automotive fuels and powertrains in the European context, JRC Technical Reports, DOI 10.2790/95629, 2014.

[67] Yang, J., Stabler, F.R., "Automotive Applications of Thermoelectric Materials," Journal of Electronic Materials, Vol. 38, No. 7, 2009 Special Issue Paper, doi: 10.1007/s11664-009-0680-z, 2009.

[68] Legros, A., Guillame, L., Diny, M., Zaidi, H., Lemort, V., "Comparison and Impact of Waste Heat Recovery Technologies on Passenger Car Fuel Consumption in a Normalized Driving Cycle," Energies 2014, 7, 5273-5290; doi:10.3390/en7085273, 2014.

[69] Mamat, A.M.I., Romagnoli, A., Martinez-Botas, R.F., "Characterisation of a low pressure turbine for turbocompounding applications in a heavily downsized mild-hybrid gasoline engine," Energy, 64: 3-16, 2014.

[70] Algrain, M., "Controlling an Electric Turbo Compound System for Exhaust Gas Energy Recovery in a Diesel Engine," Proc. of 2005 IEEE International Conference on Electro Information Technology, Lincoln, NE, 22-25 May 2005.

[71] Terdich, N., and Martinez-Botas, R., "Experimental Efficiency

Characterization of an Electrically Assisted Turbocharger," SAE Technical Paper 2013-24-0122, doi:10.4271/2013-24-0122, 2013.

[72] Bumby, J.R., Spooner, E.S., Carter, J., Tennant, H. et al., "Electrical Machines for Use on Electrically Assisted Turbochargers," 2nd Int. Conference on Power Electronics, Machines and Drives, 2004, Vol.1, pp.344-349, doi: 10.1049/cp:20040310, 2004.

[73] Balis, C., Middlemass, C., and Shahed, S.M., "Design & Development of E-Turbo for SUV and Light Truck Applications," Proc. of DEER (Diesel Engine Emissions Reduction) 2003 Conference, Newport, RI, August 2003.

[74] Callahan, T., Branyon, D.P., Forster, A.C., Ross, M.G., and Simpson, D.J., "Effectiveness of Mechanical Turbo Compounding in a Modern Heavy-Duty Diesel Engine," JSAE International Journal of Automotive Engineering, 3: 69-73, 2012.

[75] Ibaraki, S., Yamashita, Y., Sumida, K., Ogita, H. et al., "Development of the 'hybrid turbo,' an electrically assisted turbocharger," Mitsubishi Heavy Industries, Technical Review Vol. 43 No. 3, Sep.2003.

[76] Lefebvre, A. and Guilain, S., "Transient Response of a Turbochargd SI Engine with an Electrical Boost Pressure Supply," SAE Technical Paper 2003-01-1844, 2003.

[77] Pallotti, P., Torella, E., New, J., Criddle, M. et al., "Application of an Electric Boosting System to a Small, Four-Cylinder S.I. Engine," SAE Technical Paper 2003-32-0039, 2003, doi:10.4271/2003-32-0039, 2003.

[78] Teo Sheng Jye, A.E., Pesiridis, A., and Rajoo, S., "Effects of Mechanical Turbo Compounding on a Turbocharged Diesel Engine". SAE Technical Paper 2013-01-0103, 2013.

[79] Zhuge, W., Huang, L., Wei, W., Zhang, Y., and He, Y., "Optimization of an Electric Turbo Compounding System for Gasoline Engine Exhaust Energy recovery," SAE Technical Paper 2011-01-0377, 2011.

[80] Yang, J., "Potential Applications of Thermoelectric Waste Heat Recovery in Automotive Industry," 24th International Conference on Thermoelectrics, DOI:10.1109/ICT.2005.1519911, 2005.

[81] http://www.techtarget.com.

[82] http://www.Hi-Z.com.

[83] Zebarjadi, M., K. Esfarjani, M. S. Dresselhaus, Z. F. Ren, and G.

Chen, "Perspectives on Thermoelectrics: From Fundamentals to Device Applications," Energy & Environmental Science 5, no. 1 (2012): 5147, 2012.

[84]   Crane, D.T., and Jackson, G.S., "Systems-Level Optimization of Low-Temperature Thermoelectric Waste Heat Recovery," 37th International Energy Conversion Engineering Conference, pp. 583-588, 2002.

[85]   Hendricks, T.J., Lustbader, J.A., "Advanced Thermoelectric Power System Investigations for Light-Duty and Heavy Duty Applications: Part I," International Conference on Thermoelectronics/IEEE, IEEE Catalogue #02TH8657, 2002.

[86]   http://www.gentherm.com/page/thermoelectrics.

[87]   Fairbanks, J. W., "Automotive Thermoelectric Generators and HVAC," 2012 Annual Merit Review, DOE Vehicle Technologies Program and Hydrogen and Fuel Cells Program, 2012.

[88]   Headings, L., Marano, V., Jaworski, C., Guezennec, Y.G., Washington, G., Heremans, J.P., Rizzoni G., "Opportunities for Thermoelectric Energy Conversion in Hybrid Vehicles," In: IMECE 2006 ASME International Mechanical Engineering Congress and Exposition, 2006.

[89]   Crane, D., Jackson, G., and Holloway, D., "Towards Optimization of Automotive Waste Heat Recovery Using Thermoelectrics," SAE Technical Paper 2001-01-1021, 2001, doi:10.4271/2001-01-1021, 2001.

[90]   Crane, D.T., "Optimizing Thermoelectric Waste Heat Recovery From an Automotive Cooling System," Ph.D. Dissertation, University of Maryland, Ann Arbor, MI, 2004.

[91]   Stobart, R. and Milner, D., "The Potential for Thermo-Electric Regeneration of Energy in Vehicles," SAE Technical Paper 2009-01-1333, 2009, doi:10.4271/2009-01-1333, 2009.

[92]   Magnetto D., "Waste Heat Recovery Opportunities & Technologies," 3rd International Conference Thermal Management for EV/HEV, 2013.

[93]   Rowe, D.M., Smith, J., Thomas, G., Min, G., "Weight Penalty Incurred in Thermoelectric Recovery of Automobile Exhaust Heat," Journal of Electronic Materials 40(5): 784-788, DOI:10.1007/s11664-011-1571-7, 2011.

[94]   Kumar S., Heister S.D., Xu X., Salvador J. R., Meisner G. P.,

"Thermoelectric Generators for Automotive Waste Heat Recovery Systems Part I: Numerical Modeling and Baseline Model Analysis," Journal of Electronic Materials, 42(4): 665-674, DOI:10.1007/s11664-013-2471-9, 2013.

[95] LeBlanc, S., Yee, S.K., Scullin, M.L., Dames, C. and Goodson, K.E., "Material and manufacturing cost considerations for thermoelectrics," Renewable and Sustainable Energy Reviews 32 (2014) 313–327, 2014.

[96] Angrist, S.W., "Direct Energy Conversion," 4th ed., Allyn and Bacon, Boston, 1982.

[97] Minnich, A.J., Dresselhaus M. S., Ren Z. F. Chen G., "Bulk nanostructured thermoelectric materials: current research and future prospects," Energy Environ. Sci., 2009, 2, 466-479, DOI:10.1039/B822664B, 2009.

[98] Stobart, R., Wijewardane, A., and Allen, C., "The Potential for Thermo-Electric Devices in Passenger Vehicle Applications," SAE Technical Paper 2010-01-0833, 2010, doi:10.4271/2010-01-0833, 2010.

[99] Smith K., and Thornton M., "Feasibility of Thermoelectrics for Waste Heat Recovery in Conventional Vehicles," Technical Report NREL/TP-540-44247, April 2009.

[100] Lemort, V., Declaye, S., Quoilin, S., "Experimental characterization of a hermetic scroll expander for use in a micro-scale Rankine cycle," Proceedings of the Institution of Mechanical Engineers, Part A: Journal of Power and Energy, 226 (1) (2012), pp. 126–136, 2012.

[101] Colonna, P., Casati, E., Trapp, C., Mathijssen, T., Larjola, J., Turunen-Saaresti, T., Uusitalo, A., "Organic Rankine Cycle Power Systems: From the Concept to Current Technology, Applications, and an Outlook to the Future," ASME Journal of Engineering for Gas Turbines and Power 137, 2015.

[102] Wang, T., Zhang, Y., Peng, Z., Shu, G., "A review of researches on thermal exhaust heat recovery with Rankine cycle," Renewable and Sustainable Energy Reviews 15: 2862–2871, 2011.

[103] Quoilin, S., Declaye, S., Tchanche, B.F., Lemort, V., "Thermo-economic optimization of waste heat recovery Organic Rankine Cycles," Applied Thermal Engineering 31 (2011): 2885-2893, 2011.

[104] Woodland, B.J., Braun, J.E., Groll, E.A., Horton, W.T., "Experimental Testing of an Organic Rankine Cycle with Scroll-type Expander," International Refrigeration and Air Conditioning Conference at Purdue, July 16-19, 2012.

[105] Tona, P. and Peralez, J., "Control of Organic Rankine Cycle Systems on board Heavy-Duty Vehicles: a Survey," Proc. of 4th IFAC Workshop on Engine and Powertrain Control, Simulation and Modeling, Columbus (OH), August 23-26 2015.

[106] Quoilin, S., "Sustainable Energy Conversion Through the Use of Organic Rankine Cycles for Waste Heat Recovery and Solar Applications," University of Liege, 2011.

[107] Patel, P.S., and Doyle, E.F., "Compounding the truck diesel engine with an organic Rankine-cycle system," SAE Technical Paper 760343, 1976.

[108] Bailey, M.M., "Comparative Evaluation of Three Alternative Power Cycles for Waste Heat Recovery from the Exhaust of Adiabatic Diesel Engines," Lewis Research Center, Cleveland (OH), 1985 Jul, Report No. NASA TM-86953. Sponsored by the Department of Energy, 1985.

[109] Di Bella, F.A., Di Nanno, L.R., Koplow, M.D., "Laboratory and on-highway testing of diesel organic rankine compound long-haul vehicle engine," SAE Technical Paper 830122, 1983.

[110] Marciniak, T.J., Krazinski, J.L., Bratis, J.C., Bushby, H.M., Buyco, E.H., "Comparison of Rankine-Cycle Power Systems: Effects of Seven Working Fluids," Argonne National Laboratory, Energy and Environmental Systems Division, Argonne (IL), 1981 Jun, Report No. ANL/CNSV-TMe87 DE82 005599. Sponsored by the Department of Energy, 1981.

[111] Arsie, I., Cricchio, A., Pianese, C. Ricciardi, V., and De Cesare, M., "Modeling and Optimization of Organic Rankine Cycle for Waste Heat Recovery in Automotive Engines," SAE Technical Paper 2016-01-0207, 2016.

[112] Peralez, J., Tona, P., Lepreux, O., Sciarretta, A., Voise, L., Dufour, P., Nadri, M., "Improving the Control Performance of an Organic Rankine Cycle System for Waste Heat Recovery from a Heavy-Duty Diesel Engine using a Model-Based Approach," Proc. of 52nd IEEE Conference on Decision and Control, December 10-13, 2013.

[113] Vaja, I., Gambarotta, A., "Internal Combustion Engine (ICE)

bottoming with Organic Rankine Cycles (ORCs)," Energy 35 (2010): 1084-1093, 2010.

[114] Briggs, T., Wagner, R., Edwards, K., Curran, S. et al., "A Waste Heat Recovery System for Light Duty Diesel Engines," SAE Technical Paper 2010-01-2205, 2010.

[115] Crialesi Esposito, M., Pompini, N., Gambarotta, A., Chandrasekaran, V., Zhou, J. and Canova, M., "Nonlinear Model Predictive Control of an Organic Rankine Cycle for Exhaust Waste Heat Recovery in Automotive Engines," Proc. of 4th IFAC Workshop on Engine and Powertrain Control, Simulation and Modeling, Columbus (OH), August 23-26, 2015.

[116] Edwards, K.D., Wagner, R., Briggs, T., "Investigating Potential Light-duty Efficiency Improvements through Simulation of Turbo-Compounding and Waste-heat recovery Systems," SAE Technical Paper 2010-01-2209, 2010.

[117] Arsie, I., Cricchio, A., De Cesare, M., Pianese, C. et al., "A Methodology to Enhance Design and On-Board Application of Neural Network Models for Virtual Sensing of No_x Emissions in Automotive Diesel Engines," SAE Technical Paper 2013-24-0138, 2013, doi:10.4271/2013-24-0138.

[118] Pisu, P., Rizzoni, G., "A Comparative Study of Supervisory Control Strategies for Hybrid Electric Vehicles," IEEE Transactions on control systems technology, Vol. 15, No. 3, pp. 506-518, May 2007.

[119] Meloni, M., Cacciatore, D., Dohmen, J., Ring, F. et al., "Lamborghini Approach to Engine Downsizing Engine Friction Modeling," SAE Technical Paper 2013-24-0088, doi:10.4271/2013-24-0088, 2013.